CENTRAL LIBRARY

SCHOLARLY ARTICLES

A CURRENT AWARENESS BULLETIN OF ARTICLES BY FACULTY, STUDENTS AND ALUMNI

~ NOVEMBER 2013 ~

DELHI TECHNOLOGICAL UNIVERSITY

(FORMERLY *DELHI COLLEGE OF ENGINEERING)*

GOVT. OF N.C.T. OF DELHI

SHAHBAD DAULATPUR, MAIN BAWANA ROAD

DELHI 110042

PREFACE

This is the Eleventh Issue of Current Awareness Bulletin for the year 2013, started by Delhi Technological University Library. The aim of the bulletin is to compile, preserve and disseminate information published by the Faculty, Students and Alumni for mutual benefits. The bulletin also aims to propagate the intellectual contribution of DTU as a whole to the academia. It contains information resources available in the internet in the form of articles, reports, presentation published in international journals, websites, etc. by the faculty and students of Delhi Technological University in the field of science and technology. The publication of Faculty and Students, which are not covered in this bulletin, may be because of the reason that the full text either was not accessible or could not be searched by the search engine used by the library for this purpose. To make the bulletin more comprehensive, the learned faculty and Students may provide their uncovered publication to the library either through email or in CD, etc.

This issue contains the information published during November 2013. The arrangement of the contents is alphabetical wise starting from A-Z. The Full text of the article, which is either subscribed by the University or available in the web, is provided in this Bulletin.

CONTENTS

1. A Supervised Fuzzy Eye Pair Detection Algorithm ***Seba Susan** and ***Pooja Kadyan,** Department of Information Technology

2. An Empirical Study to Redefine the Relationship between Software Design Metrics and Maintainability in High Data Intensive Applications ***Ruchika Malhotra** and ***Anuradha Chug,** Department of Information Technology

3. Biodiesel Production of Waste Cooking Oil through Ultrasound Cavitation ***Amit Pal** and Surendra Singh Kachhwahab, Department of Mechanical Engineering

4. Design and Simulation of High Speed 8-bit Vedic Multiplier Using Barrel Shifter on FPGA Arnav Gupta Jaypee Institute Of Information Technology Harshit Gupta Delhi Technological University

5. Effect of holmium substitution on structural and electrical properties of barium zirconate titanate ferroelectric ceramics ***Priyanka A. Jha** and A.K.Jha, Department of Applied Physics

6. Indirect Adaptive Control of Robot Manipulator and Magnetic Ball Suspension System ***Bharat Bhushan**, Dept. of Electrical Engineering

7. Efficient AODV using Improved flooding with Sectorized Antenna for Mobile Adhoc Networks ***Rajesh Kumar Yadav, *Dr. Daya Gupta** and ***Viomesh Kumar Singh**, Computer Engineering

8. Finite element analysis of deflection of rolls and its correction by providing camber on rolls ***Vijay Gautam**, Department of Mechanical Engineering

9. Object Recognition from color images by Fuzzy classification of Gabor Wavelet features ***Seba Susan** and ***Seema Chandna**, Department of Information Technology

* **Faculty**

2013 5th International Conference on Computational Intelligence and Communication Networks

A Supervised Fuzzy Eye Pair Detection Algorithm

Seba Susan and Pooja Kadyan
Department of Information Technology, Delhi Technological University

***Abstract*— Most of the face recognition problems in literature rely on automatic eye-pair detection algorithms for locating the eye positions followed by the normalization of the face image based on the distance between the eyes. In this paper we propose a supervised fuzzy eye pair detection algorithm that can be executed in real time and requires minimal training. Nine categories of facial geometrical measurements are defined. The Gaussian function is used to compute the fuzzy memberships with the mean and standard deviation of the Gaussian being evaluated from ten reference images from the database chosen randomly. The eye pair detection algorithm works successfully on the Utrecht face database except for two cases where the eyebrow pairs are detected. The results are shown to outperform the popular eye variance filter method for eye detection.**

Keywords- Fuzzy Membership functions, Automatic Eye pair detection, Gaussian membership function, Supervised eye detection

I. Introduction

The face recognition problem [1,11] is of increasing relevance in Computer Vision problems and video surveillance applications. The face recognition procedure usually consists of two main steps [11]. The first step is the extraction of prominent facial features like the eyes, eyebrows etc. followed by normalization of the face image. The second step is representing the extracted facial information in the form of a feature vector and subsequent classification. The eye detection stage is very important for the face normalization procedure prior to the feature representation and classification stages. Several automatic eye detection algorithms have been proposed in literature [2-9]. A recent work [12] proposes a eye verifier that compares the candidate eye detected using circular filters with eye templates constructed through prior knowledge using the ternary Hamming distance for matching. We in this paper propose a supervised fuzzy eye pair detection algorithm that outperforms the conventional eye variance filter method [9]. Our method is free from the rigorous training required for neural network based classifiers [3].

The paper is organized as follows. The Face segmentation and facial feature extraction steps are outlined in Section II. The facial geometrical measurements and their fuzzification is explained in Section III. The results are discussed in Section IV and conclusions are drawn in Section V.

II. Extraction of face and facial features by morphological operations

The steps for the segmentation of the face and the extraction of prominent facial features are described below with an example for demonstration. This is achieved by segmenting out the skin pixels in the CIEL*a*b* color space as described in the following steps.

Step 1: Read the RGB input image

Fig. 1 Original Image

Step 2: Transform the image into CIEL*a*b* color space and obtain the a* (red-green axis) and b* (blue-yellow axis) color dimensions. Binarize the a* and b* matrices using Otsu's threshold The largest connected component in the intersection of a* and b* represents the face. Since a* values are high for reddish hues and b* is high for yellowish shades, the skin is segmented out with high accuracy as shown in Fig. 2 (a).

(a) (b) (c)

Fig. 2 (a) The largest connected component in the intersection of (b) binarized a* and (c) binarized b* matrices.

Step 3: Find the centroid of the white mass in Fig. 2(a) i.e. the face and denote it by (x_c,y_c).

Step 4: Now invert the above binary image to display the prominent facial features that includes the eyes as seen in Fig. 3. This image is given as the input to the fuzzy eye

978-0-7695-5069-5/13 $26.00 © 2013 IEEE
DOI 10.1109/CICN.2013.70

detector algorithm proposed in this paper described in the next section.

Fig. 3 The segmented facial features

III. The proposed facial geometrical measurements and their fuzzy memberships

After obtaining the facial features as in Fig. 3 we next form a list of white isolated components in it and that includes the two eyes, teeth as well as single isolated pixels. For every possible pair of such components, we compute the following eight features that we define collectively as the singular characteristics of the eye pair.

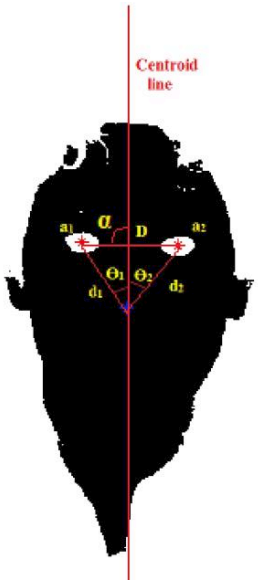

Fig. 4 Facial Geometrical features with the centroid of the face marked with a blue cross

The eight features obtained for every candidate eye pair are described below and also shown in Fig. 4 represented by their symbols.

i. **Distance between eyes (D):** Distance D between the two eyes is measured from the centre of masses of the two eyes.

ii. **Distance between 1st eye and centroid (d_1):** It is the distance calculated from the center of the first eye to the centroid of the segmented face marked by a blue cross in Fig. 4.

iii. **Distance between 2nd eye and centroid (d_2):** It is the distance calculated from the center of the second eye to the centroid of the segmented face marked by a blue cross in Fig. 4.

iv. **Angle made by eyes with the vertical axis (α):** It is the angle formed by the line joining the two eyes and the vertical axis. The vertical axis is the vertical line passing through the centroid.

v. **Angle made by 1st eye and centroid (θ_1):** This is the angle that the line joining the first eye and centroid makes with the vertical line passing through the centroid.

vi. **Angle made by 2nd eye and centroid (θ_2):** This is the angle that the line joining the second eye and centroid makes with the vertical line passing through the centroid.

vii. **Area of 1st eye (a_1):** It is the area occupied by first eye.

viii. **Area of 2nd eye (a_2):** is the area occupied by second eye.

These eight parameters are used to define nine categories or testing parameters for the eye pair. We use a few sample faces from the database with manually annotated eye pair to lay down the accepted range of values that these eight measurements may assume for an eye pair. Fuzzy category memberships are used for deciding the actual eye pair in the test images as described next.

We have chosen the Gaussian membership function to find the membership of each feature, with the mean and standard deviation determined from the mean and standard deviations of these measurements obtained from ten reference images from the database whose eye positions are manually annotated. The nine fuzzy memberships for every candidate eye pair are defined below with the first eight derived directly from the eight measurements and the ninth pertaining to equality of areas of the eyes.

i. Membership of the distance between eyes

$$\mu_1 = e^{-\frac{(D_1 - x_1)^2}{2\pi\sigma_1^2}} \quad (1)$$

ii. Membership of the distance between 1st eye and centroid

$$\mu_2 = e^{-\frac{(d_1 - x_2)^2}{2\pi\sigma_2^2}} \quad (2)$$

iii. Membership of the distance between 2nd eye and centroid

$$\mu_3 = e^{-\frac{(d_2 - x_3)^2}{2\pi\sigma_3^2}} \quad (3)$$

iv. Membership of the angle made by eyes with the vertical axis

$$\mu_4 = e^{-\frac{(\alpha - x_4)^2}{2\pi\sigma_4^2}} \quad (4)$$

v. Membership of the angle made by 1st eye and centroid with vertical axis

$$\mu_5 = e^{-\frac{(\theta_1 - x_5)^2}{2\pi\sigma_5^2}} \quad (5)$$

vi. Membership of the angle made by 2nd eye and centroid with vertical axis

$$\mu_6 = e^{-\frac{(\theta_2 - x_6)^2}{2\pi\sigma_6^2}} \quad (6)$$

vii. Membership of the area of 1st eye

$$\mu_7 = e^{-\frac{(\alpha_1 - x_7)^2}{2\pi\sigma_7^2}} \quad (7)$$

viii. Membership of the area of Area of 2nd eye

$$\mu_8 = e^{-\frac{(\alpha_2 - x_8)^2}{2\pi\sigma_8^2}} \quad (8)$$

ix. Membership of Matching between the two areas of the eyes

$$\mu_9 = e^{-\frac{(\alpha_1 - \alpha_2)^2}{2\pi\sigma_9^2}} \quad (9)$$

where, **x1, x2, x3, x4, x5, x6, x7, x8** are mean values of the respective features and $\boldsymbol{\sigma_1}$, $\boldsymbol{\sigma_2}$, $\boldsymbol{\sigma_3}$, $\boldsymbol{\sigma_4}$, $\boldsymbol{\sigma_5}$, $\boldsymbol{\sigma_6}$, $\boldsymbol{\sigma_7}$, $\boldsymbol{\sigma_8}$ are their standard deviations. These values are obtained from the mean and standard deviations of the measurements made from the manually annotated eye pairs in the ten reference images from the database selected randomly and subjected to the binarization procedure as explained in the above Section. The nine memberships (1-9) are indicative of nine fuzzy sets where the universe of discourse is the set of all possible candidate eye pairs.

The nine fuzzy memberships in (1-9) are summed up for every possible pair of candidate eye pair *p* in the segmented face (Fig. 3) obtained in Section II.

$$S_p = \sum_i \mu_i \quad (10)$$

The pair *p* that corresponds to the maximum sum of memberships i.e. $\max_{\forall p}\{S_p\}$ in the image is the eye pair. The eye pair detected in the face in Fig. 3 is shown below in Fig. 5.

Fig. 5 Eye pair detected (red crosses) for the segmented face in Fig. 3 by the proposed method.

IV. Experimental results and discussion

The results are compiled on the *Utrecht* face database [10] for 65 people out of which ten reference faces provided the parameters for the fuzzy memberships while the algorithm was tested on the other 55 faces. The images are color images whose resolution is 900x1200. The ten reference images randomly chosen are shown in Fig. 6 and the eight parameters derived from them are listed in Table 1.

Fig. 6 Ten reference images used for fuzzy eye pair detection

The MATLAB 7.9 version software was used for the implementation of the codes. The algorithm was tested on the 55 test images and the results show correct eye pair detection for all cases but except for two faces where the eyebrow pairs are detected as shown below in Fig. 7 Our proposed method was compared to the conventional eye variance filter method [9] and the results in Fig. 8 show the nine cases out of 55 for which eye variance filter method fails while the fuzzy eye pair method is successful in all these cases. This gives an overall accuracy of 96.36% for the proposed method which is much higher than the 81.81% classification accuracy for eye variance filter method.

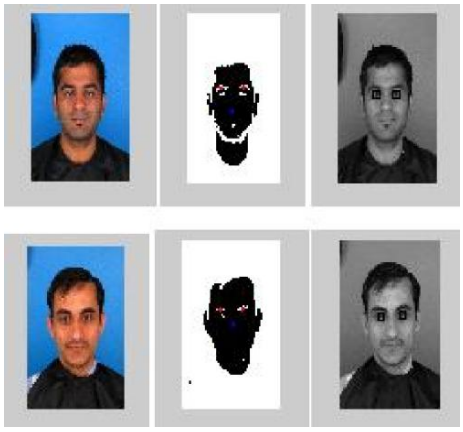

(a) **(b)** **(c)**

Fig. 7 The two cases where eyebrow pairs are detected (a) Original image (b) Result of proposed method (c) Result of eye variance filter method.

V. Conclusion

A supervised fuzzy eye pair detection algorithm is discussed in this paper based on nine geometrical features that operates successfully on the color face database. It requires minimal training and can be executed in real time unlike the neural net based classifiers. The proposed method outperforms the eye variance filter method as proved by experimental results with an accuracy of 96.36% with only two failure cases where the eyebrow pair was detected instead of the eye pair.

REFERENCES

[1] P.J. Philips, Hyeonjoon Moon, S.A. Rizvi, and O.J. Rauss, "The Feret evaluation methodology for face-recognition algorithms," *IEEE Transactions on Patt. Anal. and Machine Intelligence*, pp. 246-252, 1999.

[2] R. Stiefelhagen and J. Yang, "Gaze Tracking for Multimodal Human-Computer Interaction," *IEEE International Conference on Acoustics, Speech, and Signal Processing*, pp 2617, 1997.

[3] T. D'Orazio, M. Leo, P. Spagnolo, and C. Guaragnella, "A neural system for eye detection in a driver vigilance application," *IEEE Intelligent Transportation Systems Conference*, pp. 320-325, 2004.

[4] L. Jin, X. Yuan, S. Satoh, J. Li and L. Xia, "A hybrid classifier for precise and robust eye detection," *IEEE International Conference on Pattern Recognition*, 2006.

[5] Valenti, R., Gevers, T.: 'Accurate eye center location and tracking using isophote curvature'. *Proc. IEEE Conf. on Computer Vision and Pattern Recognition,* 2008

[6] Daugman, J.: 'The importance of being random: statistical principles of iris recognition', *Pattern Recognit.,* 2003, 36, pp. 279–291

[7] Ren, J., Jiang, X.: 'Fast eye localization based on pixel differences'. *Proc. IEEE Int. Conf. on Image Processing, 2009*, pp. 2733–2736

[8] D'Orazio, T., Leo, M., Cicirelli, G., Distante, A.: 'An algorithm for real time eye detection in face images'. *Proc. Int. Conf. on Pattern Recognition,* 2004, pp. 278 –281

[9] G.C. Feng, P.C. Yuen, "Variance projection function and its application to eye detection for human face recognition", *Pattern Recognition Lett*ers, 19 (1998) pp. 899-906.

[10] PICS, 2003. Psychological Image Collection at Stirling (PICS image data base). *Available from http://pics.psych.stir.ac.uk/, Universit of Stirling Psychology Department*.

[11] G.Zhao, Matti Pietik¨ainen, "Dynamic Texture recognition using local binary patterns with application to facial expressions", *IEEE Transactions on Pattern Analysis and Machine Intelligence*, 2007.

[12] Nguyen, Van Huan, Thi Hai Binh Nguyen, and Hakil Kim. "Reliable detection of eye features and eyes in color facial images using ternary eye-verifier." *Pattern Recognition* (2012).

TABLE 1: MEAN AND STANDARD DEVIATIONS (S.D.) OF THE NINE GEOMETRICAL MEASUREMENTS DERIVED FROM TEN REFERENCE IMAGES IN FIG. 6

Images	D	d_1	d_2	α	θ_1	θ_2	a_1	a_2
1st	179.42	81.46	96.46	92.16	33.44	39.50	1802	1756
2nd	214.16	89.59	123	91.68	30.10	39.54	2101	2085
3rd	222.15	121.80	99	94.08	42.03	39.73	2216	2308
4th	184.11	94.74	87.6	90.91	31.56	30.11	1644	1681
5th	216.79	105.79	110.12	88.80	50.24	49.96	1850	1745
6th	194.64	85.11	108.49	90.95	41.33	49.16	1384	1309
7th	201.84	100.39	100.59	88.35	53.32	51.32	1479	1591
8th	180.96	80.02	99.45	92.08	32.95	40.28	1827	1853
9th	200.49	120.39	78.16	88.31	35.14	24.02	913	1177
10th	210.19	86.13	122.82	92.10	37.33	49.28	1667	1774
Mean	**200.51**	**96.54**	**102.58**	**90.94**	**38.74**	**41.29**	**1688**	**1727**
S.D	**15.50**	**15.26**	**14.14**	**1.90**	**7.92**	**9.03**	**372.23**	**330.45**

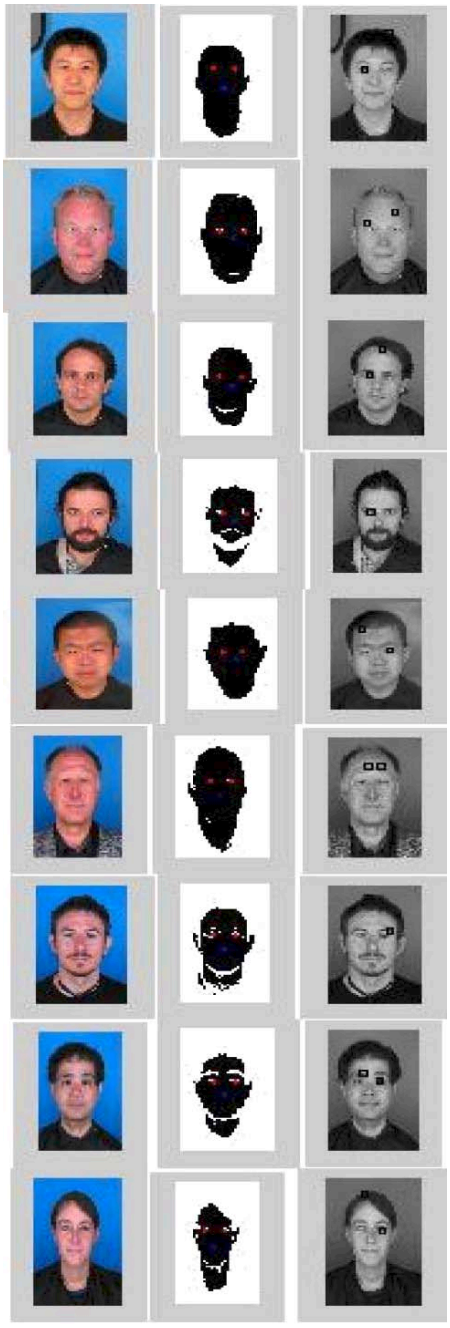

(a) (b) (c)

Fig. 8 The eye pair detection results (a) Original Image (b) Result of proposed fuzzy eye pair detection method (c) Result of Eye variance filter

An Empirical Study to Redefine the Relationship between Software Design Metrics and Maintainability in High Data Intensive Applications

Ruchika Malhotra and Anuradha Chug

***Abstract*—Software maintainability is defined as the ease with which modifications could be made in to the software once it is delivered to the customer. While evaluating the quality of the software product, software maintainability is one of the most important aspects and it is desirable that the software should be designed and coded in such a way that it becomes more maintainable. Tracking the maintenance behavior of the software product is very complex and widely acknowledged by the researchers. We can accurately measure 'maintainability' of any software once it comes into operations but it would be too late by then, hence much has been examined in literature to measure the maintainability before software start operations by making use of software design metrics. It has proved empirically many times that there exists strong relationship between software design metrics and its corresponding maintainability. However, the framework and reference architecture in which the softwares are developing now days have changed dramatically as they make heavy use of databases. There is a strong need to re-define the relationship between software design metrics with subsequent maintainability in this changed scenario. In an attempt to address this issue quantitatively, we have proposed new suite of metrics by the induction of two new metrics which are more important and meaningful in data intensive applications. To analyze the proposed metric suite, their values are computed on five real-life applications which make use of databases with a great deal. The result shows that proposed new metrics suite is very effective indicator of software maintainability in the environment which provide remote connections to the server for accessing large database files. Based on the results it can be reasonably claimed that new metrics suite proposed in the current study would be able to predict software maintainability more precisely and accurately for those applications which makes heavy use of databases during operations.**

***Index Terms* - Object Oriented Metric, Maintainability predictions, Software quality, Empirical validation, Database design metrics**

I. INTRODUCTION

The modifications in the software are required to meet the changing requirements of customers which may arise due to many reasons such as change in the technology, introduction of new hardware or enhancement of the provided features etc. Producing software which is not required to be changed is not only impractical but also very uneconomical. This process of changing the software which has been delivered previously is called software maintenance and the ease with which it could be achieved is defined as software maintainability [1].

Manuscript received Aug 07, 2013; Revised Aug 17, 2013.

Ruchika Malhotra is with Dept of Software Engineering, Delhi Technological University, Delhi, India (ruchikamalhotra2004@yahoo.com)

Anuradha Chug is with USICT, GGSIP University, Dwarka, New Delhi, India (corresponding author +91-11-25302715/25302318; e-mail: a_chug@yahoo.co.in).

It has been observed that the amount of resource, effort and time spent on software maintenance is much more than what is being spent on software development [2]. Thus, producing software that is easy to maintain may potentially save large costs. One of the most common approaches for controlling maintenance cost is by utilizing software design metrics during the development phase [3]. Various metrics have been proposed in the literature along with their corresponding impact on software maintainability. In this paper we have selected significant subset of seven metrics proposed in literature and added two new metrics as they found to be more impactful on software maintainability in current scenario where applications are intensely using databases during operations. The main purpose of this paper is twofold, firstly:

(a) Review the role of various metrics which are proposed in literature on software maintainability and secondly

(b) To purpose and empirically validate a new suite of metrics with the induction of two new metrics which have larger impact on software maintainability in current scenario where more data intensive application development is in progress.

For empirical validation of the proposed metrics suite we have collected the data from five windows based and web based applications. All applications were based on object oriented (OO) methodologies and developed in Microsoft Visual Studio using C# language and exploit the use of databases. Values of proposed metrics are collected for every class of each application. The independent variables are nine design metrics used to measure OO feature and database design feature present in the code. Dependent variable in our study is 'Change' and counted as number of lines of source code added, deleted or modified during operations. Use of Artificial Neural Network (ANN model) for the prediction of maintainability has reported as best fitting machine learning model [8, 9, and 10]; therefore it is used in current study for building the prediction model using data points collected from all five real-life application for new proposed metrics suite. We hope that while designing and coding, developers can analyze and predict maintainability more precisely with the help of proposed metrics suite. Detecting the 'Maintainability' in early phases of Software Development Life Cycle (SDLC) would ensure that correction has no side effects on dependent modules. Further, developers can judge if the application is maintainable or not. This in itself would save time and money for the organization responsible for developing and deploying.

The remainder of the paper is organized as follows: Section II summarizes related work. Section III elucidates empirical data collection method. In Section IV, independent and dependent variables selected in the study are discussed. Section V enumerates research methodology. In Section VI

ISBN: 978-988-19252-3-7
ISSN: 2078-0958 (Print); ISSN: 2078-0966 (Online)

explores characteristics of the collected data using descriptive statistics. The results and analysis is presented in Section VII. Section VIII states threat to validity and finally section IX concludes the paper with future directions.

II. RELATED WORK

There are several models and metrics proposed in literature to predict the maintainability of the software. Chidamber et al. [4] outlined some initial proposals for language-independent OO design metrics in 1991 and proposed six object oriented design metrics to predict the maintainability of OO systems. This suite is further expanded in 1994 and the metric suite was tested on systems developed in C++ and Smalltalk(TM) by Chidamber et al [6]. Two more metrics were added in to existing C&K metrics suite by Li et al [5 and 7]. The proposed metrics suite became quite popular and evaluated analytically in several studies by many researchers including Dagpinar et al. [8], Thwin et al [9], Aggarwal et al [10], Koten et al [11], Zhou et al [12], Elish et al [13] and Kaur et al [14] which were conducted to validate C&K metrics suite. Many prediction models were built using statistical algorithms as well as machine learning algorithms. Neural Network was used by Thwin et al [9], Bayesian Belief Network (BBN) was used by Koten et al [11], Multivariate Adaptive Regression Splines (MARS) was used by Zhou et al [12] and TreeNets was used by Olish et al [13] to build models for the prediction of software maintainability using OO design metrics suite. Ping [15] suggested that more quantitative approach to measure maintainability should be adopted. Jin et al [16] have successfully applied use of Support Vector Machine (SVM) to predict software maintainability using OO metric suite. Recently Malhotra et al [17] have proposed the use of Group Method of Data Handling (GMDH) to predict software maintainability more concisely and precisely. However, there is strong need to redefine the metrics suite used for prediction of software maintainability which is more relevant in data intensive applications. In an attempt to address this problem, the current study was undertaken to ascertain the cumulative effects by the attributes of object oriented paradigm and database design characteristics on software maintainability. To achieve this aim, authors have proposed and validated new metrics suite which is found to be more appropriate and precise in predicting maintainability for data intensive applications.

III. EMPIRICAL DATA COLLECTION

Five customized softwares were selected for empirical validation out of which three were window based applications and two were web based applications. All five applications were data intensive and sophisticated as they concentrate on collecting, maintaining, indexing and computing data from database. Their functioning is described in brief as follows:

- FLM is a customize software to handle the File Letter Monitoring System. (FLM System)
- EASY is a web portal for an Educational Institute which provide study material online. (EASY System)
- SMS system is Student Management System which maintains the record of students & teacher for private educational institute. (SMS System)
- IM System is Inventory Management System which maintains inventory of company at different branch offices in different cities. (IMS System)
- ABP system is Angel Bill Printing software maintains fully editable items list by client itself with generation of a common bill format. (ABP System)

To measure the maintainability we first found out the "change effort" which is defined as amount of average efforts required to add, change or delete lines of source code. To measure the various features of object oriented paradigm such as data hiding, inheritance, cohesion, coupling, memory allocation etc different metrics were carefully selected. We reviewed various metrics proposed in literature and compiled in Malhotra et al [17] and Aggarwal et al [18]. We selected only those software design metrics which were proven to be strongly associated with software maintainability. Further two more metrics were proposed (described in section 4) in the study as they found to be more meaningful in data intensive applications. Two versions of each of the software were taken and analyzed for "Changes" made into it. Changes were counted in terms of added, deleted and modified lines in the recent version with respect to the previous version. Addition and deletion of line in source code was counted as one change whereas modification was counted as two (one line added, one line deleted) changes. Selected Metrics as described in section 4 were collected for these five web and window based applications. Tool was created in visual studio which collected the values of selected metrics which were further used for constructing prediction model to drive object oriented software maintainability.

IV. INDEPENDENT AND DEPENDENT VARIABLES

The selected five applications namely FLM, EASY, SMS, IMS and ABP were developed in Visual Studio 2010. To measure various attributes of OO paradigm such as size, coupling, cohesion and inheritance, one metric alone would not be sufficient hence total nine metrics were selected and compiled in Table I and Table II. Five metrics namely Maintainability Index (MI), Cyclomatic Complexity (CC), Depth of Inheritance (DOI), Coupling between Objects (CBO) and Lines of Code (LOC) were retrieved from the Visual Studio by considering all applications one by one in the .net environment. For description of these metrics please refer Table I wherein the metrics mentioned were calculated from the intermediate language code generated while compiling the project. In the next stage of our research work, we have created a tool in visual studio to collect four metrics namely Code to Comments Ratio (CCR), Number of Data Base Connections (NODBC), Weighted Methods per Class (WMC) and Lack of Cohesion of Methods (LCOM). First two metrics namely CCR and NODBC have been proposed for the first time in the current study and as the part of our research project, we proposed that these two metrics carries more impact on software maintainability in database intensive applications. Apart from database design, all aspects of object oriented design such as coupling, cohesion and inheritance are equally important. Since complexity and cohesion were missing in Table I, two metrics WMC and LCOM were taken from C&K Metrics suite [4-7] to cover complexity and cohesion respectively. For description of these metrics please refer Table II.

Next, source codes of two versions (original version and modified version) were taken for each application. Values of first five metrics as described in Table I were obtained through .net and values of remaining four metrics as described in Table II were obtained through the Tool we created in first phase. We investigated source code of both versions (original version and modified version) for each

ISBN: 978-988-19252-3-7
ISSN: 2078-0958 (Print); ISSN: 2078-0966 (Online)

TABLE I : METRICS COLLECTED FOR OBJECT ORIENTED SOFTWARE

S no	**Metric Name**	**Description**
1	Maintainability Index (MI)	Calculates an index value between 0 and 100 that represents the relative ease of maintaining the code.
2	Cyclomatic Complexity (CC)	Measures the structural complexity of the code. It is created by calculating the number of different code paths in the flow of the program module. A program that has complex control flow will require more tests to achieve good code coverage and will be less maintainable.
3	Depth of Inheritance (DIT)	Indicates the number of class definitions that extend to the root of the class hierarchy. The deeper the hierarchy the more difficult it might be to understand where particular methods and fields are defined or/and redefined.
4	Coupling Between Object classes	Count the number of other classes to which it is coupled. To measures the coupling to unique classes through parameters, local variables, return types, method calls, generic or template instantiations, base classes, interface implementations, fields defined on external types, and attribute decoration.
5	Lines of Code (LOC)	Indicates the approximate number of lines in the code. The count is based on the Intermediate Language (IL) code and is therefore not the exact number of lines in the source code file. A very high count might indicate that a type or method is trying to do too much work and should be split up. It might also indicate that the type or method might be hard to maintain.

application to calculate the amount of 'change' made in each class. It is calculated manually by comparing the recent version of source code for class with the previous version of the same class. Difference is observed in terms of lines of source code added, deleted or modified for each class. The values of collected metrics were finally compiled class wise with respective values of 'change' made in that class in the recent version and combined respectively to generate data points. We have compiled all the classes for each application to generate data points. For FLM System, EASY System, SMS System, IMS System and for ABP System the number of data points are 233, 292, 129, 96 and 114 respectively. Same methodology is adopted in Zhou et al [19].

TABLE II : METRICS COLLECTED BY TOOL FOR SELECTED WEB AND WINDOW BASED APPLICATIONS

SNo	Metric Name	Description
1	CCR (Comments to Code Ratio)	Ratio of number of comments lines to number of code lines in C# code file. Number of comment lines to the tatal number of lines in the source code were compared to find the values of this metric.
2	NODBC (Number of Data Base Connections)	Number of Data Base Connection is a measure to count number of times database connection were made. It is counted by counting 'Open()' function call for database connection in the source code.
3	WMC (Weighted Methods per Class)	The sum of Mc Cabes's cyclomatic complexities of all local methods in a class. Let a class K_1 with method M_1… M_n that are defined in the class. Let C_1…….Cn be the complexity of the methods.
4	LCOM (Lack of Cohesion of Methods)	The number of disjoint sets of local methods. Each method in a disjoint set shares at least one instance variable with at least one member of the same set.

V. RESEARCH METHODOLOGY

Recent research activities have revealed that Artificial Neural Network (ANN) have powerful pattern classification and pattern recognition capacity. They are well suited for prediction problems in which required knowledge is difficult to specify but enough data or observations are available to learn. Although it was proposed in 1964 by Hu [20] brought into use by 1986 when back propagation algorithm was introduced for learning by Rumelhart et al [21]. Originally they were developed to mimic basic biological neural systems particularly the human brain, composed of number of interconnected simple processing elements called neurons which receive input signal from other nodes, process it and produce output signal to other nodes. Before ANN can forecast any desired task, it has to be trained first. Typical case of ANN i.e. Feed Forward Neural Network (FFNN) was used in the current study. In FFNN, information moves in only one direction i.e. forward from input nodes to output nodes through hidden nodes and there are no loops in the network. FFNN is the most practical ANN model and presented in Figure 1. Artificial Neural Network Model (ANN) in Mat Lab Tool was created for the prediction of software maintainability and Multi-Layer Feed-Forward Neural Network Model was selected for learning using empirical data collected in Section-3 and Section-4. The number of hidden neuron selected as 10 for the sample data collected from these five real life applications. Independent variables selected in the current study are nine metrics as described in Table I and Table II and dependent variable is 'Change'. In total, metrics of 864 classes were collected and combined with corresponding 'Changes' made in that class to generate data points for all five applications mentioned in section 3. We partitioned our data into three parts in the ratio of 3:1:1 for training, testing and validation respectively. 60% of the data was used for training i.e. machine learn from the data patterns using specified algorithm, 20% of the data was used for testing where we check how much the predicted values are closer to actual values, 20% of the data was used for validations. Prediction accuracy is calculated by comparing actual value of 'Change' calculated manually in section 4 with predicted values of 'Change'.

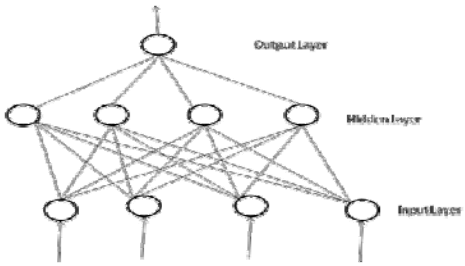

Fig. 1 : A typical Feed Forward Neural Network (FFNN)

VI. DESCRIPTIVE STATISTICS

Descriptive statistics (minimum, maximum, mean, and Median and standard deviation) were calculated and their interpretations are presented in this section. Table-III represents descriptive statistics for class level metrics which were collected for 864 classes consists of five applications FLM, EASY, SMS, IMS and ABP and 233, 292, 129, 96, 114 classes respectively considered in the current study. Following are the observations made from descriptive statistics:

ISBN: 978-988-19252-3-7
ISSN: 2078-0958 (Print); ISSN: 2078-0966 (Online)

TABLE III : DESCRIPTIVE STATISTICS OF CLASS LEVEL METRICS COLLECTED FOR FIVE SELECTED APPLICATIONS

	FLM System					EASY system				
	Max	Min	Mean	Median	Std Dev	Max	Min	Mean	Median	Std Dev
Cyclomatic Complexity (CC)	29	1	19.31	16	13.76	22	1	20.6	19	14.27
Depth of Inheritance (DIT)	7	1	4.379	5	1.321	5	1	3.6	4	2.503
Coupling Between Object classes	50	3	26.14	30	13.86	54	0	33.5	38.5	21.59
Lines of Code (LOC)	7749	33	189.9	113	207.3	4189	91	207	188	171.7
CCR	5	2	3.276	3	2.978	7	3	4.57	5	5.58
NODBC	12	0	2.483	0	3.532	7	0	2.7	0.5	3.433
WMC (Weighted Methods per Class)	16	1	6.276	5	4.978	23	1	10.5	9.5	8.58
LCOM (Lack of Cohesion of Methods)	0	0	0	0	0	0	0	0	0	0
Maintainability Index (MI)	91	40	61.14	56	18.04	94	43	64.1	56.5	17.92
Change	95	5	41.98	67	45.67	87	9	52.52	63	43.23

	SMS System				
	Max	Min	Mean	Median	Std Dev
Cyclomatic Complexity (CC)	27	1	21.5	19.5	19.62
Depth of Inheritance (DIT)	6	1	3.25	4	2.121
Coupling Between Object classes	59	3	45.38	52.5	18.66
Lines of Code (LOC)	9699	83	367.6	351	219.5
CCR	6	2	4.625	16.5	9.18
NODBC	6	0	3	3	2.507
WMC (Weighted Methods per Class)	29	2	16.63	17.5	9.18
LCOM (Lack of Cohesion of Methods)	0	0	0	0	0
Maintainability Index (MI)	81	49	55.25	52	10.57
Change	79	13	67.89	47	32.43

	IMS System					ABP System				
	Max	Min	Mean	Median	Std Dev	Max	Min	Mean	Median	Std Dev
Cyclomatic Complexity (CC)	13	2	10.79	7	12.39	14	2	10.33	8.5	8.886
Depth of Inheritance (DIT)	5	4	4.029	4	0.171	6	3	4.017	4	0.131
Coupling Between Object classes	30	2	13	13.5	8.09	29	4	14.93	17	8.569
Lines of Code (LOC)	8319	117	43.65	21.5	65.46	7156	171	40.91	32	40.37
CCR	12	0	3.147	3	2.572	11	1	2.483	2	1.847
NODBC	5	0	2.118	1	3.859	8	0	4.931	1	1.041
WMC (Weighted Methods per Class)	12	0	3.147	3	2.572	11	1	2.483	2	1.847
LCOM (Lack of Cohesion of Methods)	3	0	0.147	0	0.558	6	0	0.155	0	0.812
Maintainability Index (MI)	100	48	71.79	67	17.85	100	40	69.5	61	21.04
Change	213	18	79.87	103	67.93	189	19	91.23	78	45.63

ISBN: 978-988-19252-3-7
ISSN: 2078-0958 (Print); ISSN: 2078-0966 (Online)

- Value of LCOM for FLM, EASY, SMS, IMS and ABP are 0, 0, 0, 3 and 6 respectively which represents that classes are quite cohesive in first three applications.
- Values of DIT for FLM, EASY, SMS, IMS and ABP are 7, 5, 6, 5 and 6 which represents that inheritance is properly exploited in all the selected applications.
- Comments to code ratio is medium in FLM, EASY and SMS and High in IMS and ABP which means IMS and ABP would be easier to understand in maintenance phase.
- Numbers of database connections are more in IMS and ABP systems and less in FLM, EASY and SMS systems.

VII. RESULTS AND DISCUSSION

Many measures have been proposed in literature to estimate the accuracy of different prediction models as part of the studies carried by Conte [22], Kitchenham [23] and Bryson [24], however in the current study we have used most prevalent model i.e. Mean of Absolute Relative Error (MARE) suggested by Kitchenham[23]. To calculate MARE, first we calculate Absolute Relative Error (ARE) using equation (1) followed by Mean of ARE using equation (2). For n observations it is calculated as follows:

$$ARE = \frac{|AV - PV|}{AV} \dots\dots\dots\dots\dots\dots\dots\dots\dots\dots (1)$$

$$MARE = \frac{1}{n}\sum_{i=1}^{n} AREi \dots\dots\dots\dots\dots\dots\dots (2)$$

AV is actual values of 'Change' and PV is predicted values of 'Change' using FFNN modeling. MARE values of all five applications FLM System, EASY System, SMS System, IMS System and for ABP System are 0.3478, 0.3676, 0.4769, 0.4966 and 0.4568 as plotted in Figure-2. The prediction accuracy achieved in the current study using

ANN Modeling was compared with other proposed models as determined by Dagpinar et al. [8], Thwin et al [9], Aggarwal et al [10], Koten et al [11], Zhou et al [12], Elish et al [13] and Kaur et al [14] for software maintainability prediction. It can be easily observed that noticeable and quite competitive predication accuracy has been achieved using new proposed metric suite.

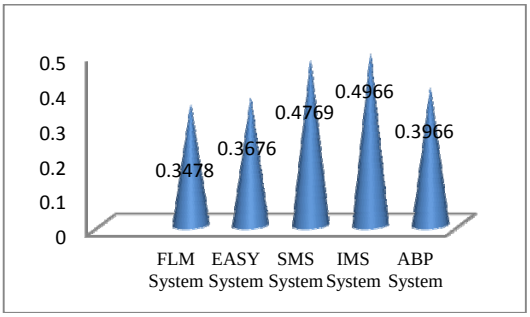

Fig 2 : Applications' and their respective MARE values

To further analyze the results we closely observed the amount of data handled in each application. Maximum values of NODBC for FLM, EASY, SMS, IMS and ABP are 12, 7, 6, 5 and 8 respectively. It is obtained by counting for how many times 'Open ()' is used in each application. We observed that 'EASY' application is more data intensive while IMS is least data intensive when compared against number of database connections made in each application. We also analyzed the results from different perspective to observe the effects of CCR metrics on maintainability which is the ratio of number of code lines to number of comment lines. This metric mainly affects the understandability of the code. The value of CCR metric is highest for FLM system while lowest for SMS system. When the predicted results were compared with actual changes, it was indicated that for FLM systems best prediction accuracy has been achieved and for IMS system, value of MARE is minimum. For FLM systems predictions accuracy was 81% (0.3478/0.4291) more than average prediction accuracy achieved from all other applications. Correlation charts were also drawn between NODBC and 'Change' using SPSS and found to be significant as shown in Figure 3(a). We also observed the correlation between CCR and 'Change' as shown in Figure 3(b). Predicted results are very close to actual values of change. Based on the above findings, followings conclusions are drawn:

- The predicted values are very close to actual values using new metrics suite.
- Proposed metrics (NODBC and CCR) are significantly correlated with software maintainability.
- NODBC and CCR are more impactful while predicting software maintainability for data intensive applications.

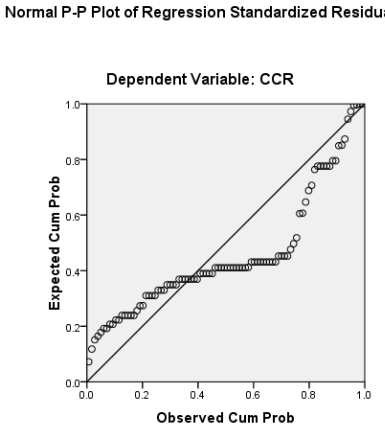

Fig. 3 :(a) Correlation chart between 'NODBC' and 'Change'.

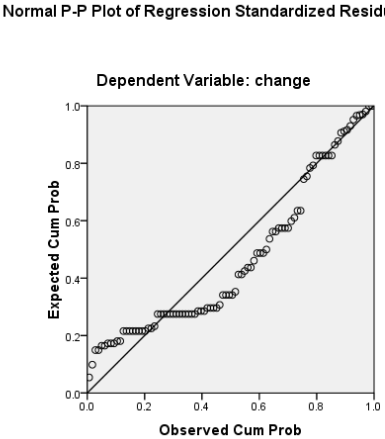

Fig. 3 : (b) Correlation chart between 'CCR' and 'Change'

ISBN: 978-988-19252-3-7
ISSN: 2078-0958 (Print); ISSN: 2078-0966 (Online)

VIII. THREATS TO VALIDITY

An empirical study always carries few threats to its validity which are equally applicable to the current study and taken into consideration. Empirical data collected from real life application got few specific characteristics and cannot be generalized. Judgments were based on cumulative effects of all metrics on maintainability however it would be more preferable to have controlled environment where at any given time only two new metrics proposed in the study are observed and all other metrics remained constant. Apart from the metrics suite which is used to measure internal quality attributes in the current study, maintainability also depends upon external quality attributes such as quality of the code, expertise of developers, familiarity of the code, reusability etc. In the current study we have considered only internal design metrics and external quality attributes have been deliberately ignored. Although we have tried our best to minimize these threats by taking five different applications which varies greatly on account of database handling, comments and lines of source code. However, these threats can only be removed by conducting more replicated studies using different platforms, different architecture and with different datasets.

IX. CONCLUSION

Objective of our current study was to empirically investigate the effect of newly proposed metrics suite on software maintainability in highly data intensive applications. FFNN modeling techniques was used for the prediction of OO software maintainability using five real life applications. A total of nine important metrics were used to capture attributes of object oriented design and database design. Definition of seven OO design metrics were picked up from the literature and two new metrics were proposed to capture attributes of database design. Newly proposed metrics suite was found to be more meaningful in today's application development scenario which is highly data intensive. Proposed new metrics suite was empirically verified as competitive prediction accuracies were achieved. From the results it can be safely suggested that new metrics suite proposed in the current study appears to be more useful in predicting maintainability of the OO software. Researchers and practitioners developing data intensive applications can make use of this metrics suite for the prediction of software maintainability in early phases of software development in order to achieve better planning of resources. We would like to conduct additional empirical studies in future with an aim to verify and support the findings of this paper on other datasets. Finding of this paper are valid for object oriented medium size system. We are planning to replicate this study for large OO systems. We are also planning to investigate the capability of newly proposed metrics suite in emerging software development scenario such as aspect oriented software development, service oriented software development and component based application development in predicting the maintainability.

REFERENCES

[1] Software Engineering Standards Committee of the IEEE Computer Society, IEEE Std. 828-1998 IEEE Standard for Software Configuration Management Plans, standard, 1998

[2] Aggarwal K. K. and Yogesh Singh, “Software Engineering”, New Age International Publishers, Third Edition, 2008.

[3] Dimitris S, Xenos M, Dimitris C. Relation between Software Metrics and Maintainability. Proceedings of Federation of European Software Measurement Association 1999, Amsterdam, Netherlands: 465-476

[4] Chidamber, Shyam R. and Cris F. Kamerer, “Towards a metrics Suite for Object-Oriented Design Proceedings”, OOPSLA'91, July 1991, pp.197-211 Conference 1991

[5] W. Li and S. Henry, "Object-Oriented Metrics that Predict Maintainability," Journal of Systems and Software, vol. 23, pp. 111-122, 1993.

[6] S. Chidamber and C. Kemerer, "A Metrics Suite for Object Oriented Design," IEEE Transactions on Software Engineering, vol. 20, no. 6, pp. 476-493, 1994

[7] W. Li, “Another Metric Suite for Object-oriented Programming”, The Journal of System and Software, 44:155–162,1998

[8] Dagpinar M and Jahnke JH, “Predicting Maintainability with Object-Oriented Metrics - An Empirical Comparison”, Proceeding of WCRE '03 Proceedings of the 10th Working Conference on Reverse Engineering; IEEE Computer Society Washington, DC, USA ©2003.

[9] M. Thwin and T. Quah, "Application of neural networks for software quality prediction using object oriented metrics", Journal of Systems and Software, vol. 76, no. 2, pp. 147-156, 2005.

[10] K. K. Aggarwal, Yogesh Singh, Arvinder Kaur, and Ruchika Malhotra, Application of Artificial Neural Network for Predicting Maintainability using Object- Oriented Metrics, World Academy of Science, Engineering and Technology 22 2006

[11] C. van Koten, A.R. Gray, “An application of Bayesian network for predicting object-oriented software maintainability”, Information and Software Technology, Journal,48(2006)59-67. www.elsevier.com/locate/onfsof

[12] Y. Zhou and H. Leung, "Predicting object-oriented software maintainability using multivariate adaptive regression splines," Journal of Systems and Software, vol. 80, no. 8, pp. 1349-1361, 2007.

[13] M.O.Elish, K.O. Elish, “Application of TreeNet in Predicting OOSoftware Maintainability: A Comparative Study”, European Conference on Software Maintenance and Reengineering , 2009

[14] Arvinder Kaur, Kamaldeep Kaur, Ruchika Malhotra,” Soft Computing Approaches for Prediction of Software Maintenance Effort”, 2010 International Journal of Computer Applications (0975 - 8887) Vol 1,No. 1680

[15] Liang Ping, “A Quantitative Approach to Software Maintainability Prediction “, 2010 International Forum on Information Technology and Applications

[16] Cong Jin, Jin-An Liu , “Applications of Support Vector Machine and Unsupervised Learning for Predicting Maintainability using Object-Oriented Metrics”, 2010 Second International Conference on Multi Media and Information Technology

[17] Ruchika Malhotra and Anuradha Chug,“Software Maintainability Prediction using Machine Learning Algorithms”, Software Engineering: An International Journal (SEIJ). Vol 2 , number 2, pp-19-36, 2012.

[18] K.K.Aggarwal, Yogesh Singh, Arvinder Kaur, Ruchika Malhotra, Empirical Study of Object-Oriented Metrics, Journal of Object Technology, Vol. 5, No. 8, November-December 2006

[19] Zhou Y, Leung H, Xu B, ‘Examining the potentially confounding effect of class size on the associations between object oriented metrics and change proneness’. IEEE Transaction of Software Engineering vol: 35, issue 5 :607–623, 2009

[20] Hu M.CJ. 1964, Application of the adaline system to wether forecasting. master thesis, technical report 6775-i, stanford electronics laboritries, stanford, ca, june

[21] Rumelhart D. E., Hinton GE, Williams RJ: Learning internal Presentation by back-propagating errors, The PDP research Group, Parallel Distributing Processing: Exploration in the Microstructure of cognition, MIT Press, MA, 1994

[22] S. Conte, H. Dunsmore, and V. Shen,” Software Engineering Metrics and Models”. Menlo Park, CA:Benjamin/Cummings, 1986.

[23] B.A. Kitchenham, L.M. Pickard, S.G. MacDonell, M.J. Shepperd,” What accuracy statistics really measure”, IEE Proceedings-Software 148 (3) (2001) 81–85

[24] Bryson AE, Ho YC, “Applied optimal control: optimization, estimation, and control”, Blaisdell Publishing Company or Xerox College Publishing. pp. 481.1969

International Journal of Engineering Research and Technology.
ISSN 0974-3154 Volume 6, Number 3 (2013), pp. 291-306

http://www.irphouse.com

Biodiesel Production of Waste Cooking Oil through Ultrasound Cavitation

Amit Pal[a] and Surendra Singh Kachhwaha[b]

[a]Department of Mechanical Engineering,
Delhi Technological University, Delhi, 110042.
[b]Dept. of Mechanical Engineering, School of Technology,
PDPU, Gandhi Nagar, India.

Abstract

This paper presents the comparative details of biodiesel production process using low frequency ultrasonic energy (28-33 kHz) and conventional mechanical stirrer method. For this purpose, Waste Cooking Oil (WCO) is used as the biodiesel feedstock. The experiments have been performed for molar ratio (alcohol/oil) 6:1 and 4.5:1, with three different catalyst percentages (0.5%, 0.75% and 1%) of Potassium Hydroxide. The important chemical and physical properties of Waste Cooking Oil biodiesel were determined and compared with diesel. It is observed that the density and viscosity values of the biodiesels produces are within the permissible limits but still higher than petroleum diesel. Further an experimental investigation has been carried out on a four cylinder, diesel engine operating on diesel and biodiesel blends [B10, B20, and B30]. It can be concluded from present study that: (i) Biodiesel production through ultrasound energy seems to be a relatively simple, efficient, time saving, eco-friendly and industrially viable process. (ii) The trends for percentage variations of performance parameters for biodiesel blends (in reference to diesel as baseline) do not show any deterioration.(iii) There is tremendous improvement in smoke reduction while operating with biodiesel as compared to petroleum diesel.

Keywords: Biodiesel; Ultrasonic energy; Waste Cooking oil; Performance tests; Engine emissions.

1. Introduction

Majority of the world's energy needs are supplied through petrochemical sources, coal and natural gas, with the exception of hydroelectricity and nuclear energy, all these sources are finite and at current usage rates will be consumed shortly[1]. Economic growth is always accompanied by commensurate increase in the transport. Diesel fuel play important role in the industrial economy of developing countries and commonly used in transports, industrial and agricultural goods, etc. Compared to rest of the world, India's demand for diesel fuel is six times higher than gasoline [2]. Also, petroleum fuels are currently the dominant global source of CO_2 emissions and their combustion is posing stronger threat to clean environment. This has stimulated the recent interest in alternative sources for petroleum-based fuels.

A viable alternative fuel should be easily available, environment friendly and techno-economically competitive. Bio-diesel is an alternative to petroleum-based fuels derived from vegetable oils or animal fats [3]. It is named biodiesel because it is derived from biological products and matches petro diesel in performance. Vegetable oils are widely available from different kind of plants and the glycerides present in the oils can also be separated and used as by-product [4]. Bio-diesel production is a very modern and technological area for researchers due to its environmental advantages the increase in the price of petroleum fuels [5]. The most common way of producing bio-diesel is the transesterification of vegetable oils and animal fats. Vegetable oils have good heating power and provide exhaust gas with almost no sulphur and aromatic polycyclic compounds. It possesses high biodegradability and lubricating property which makes it even better fuel. As vegetable oils are produced from plants, their burning is completely recyclable as it produces carbon dioxide (CO_2), which is consumed by the plants in photosynthesis [6]. Vegetable oils can be directly used as fuel for diesel engines, but their viscosities are much higher (10 to 20 times) than usual diesel fuel and require modifications of the engines [7]. The injection and atomization characteristics of the vegetable oils are significantly different than those of petroleum-derived diesel fuels, mainly due to their high viscosities [8].

In a country like India, having huge agricultural potential vegetable oils proves a promising alternate for petroleum (diesel oil) fuel. In recent years systematic effort have been made by several researchers to use vegetable oils like sunflower, peanut, soybean, rapeseed, palm, olive, cottonseed, linseed, jatropha, coconut, pongamia, rubberseed, jojoba etc. as alternative for diesel. Many of the vegetable oils are edible in nature; therefore their continuous use may cause shortage for food supply and prove far expensive to be used as fuel at present. So far a very few of non-edible vegetable oils have been tried on diesel engine leaving a lot of scope in this area. Different countries are looking for different types of vegetable oils as substitutes for diesel fuels that further depending upon the climate and soil conditions. For example; soya-bean oil in U.S., Rapeseed and Sunflower oils in Europe, Palm oil in Southeast Asia and Coconut oil in Philippines are being used [9].

India is a developing country and its energy demand is increasing day by day. Vegetable oils are good alternative source in Indian context because India is

agriculture based country. Vegetable oil consists edible and non-edible oil, edible oil demand being higher than its domestic production, there is no possibility of diverting these oils for production of bio-diesel. Non-edible oil plants can be planted on under-stocked forest lands, farmer's field boundaries to provide protective hedge, fallow lands, public lands along railway tracks, highways, canals and community and government land in villages. Therefore biodiesel production through non-edible oil is major concerned field for India. The by-products of Bio-diesel from non edible oil are oil cake and glycerol which have good commercial value.

Basic reaction carried out in the biodiesel production is transesterification. In this reaction different catalysts can be used to enhance the transesterification reaction which is namely alkali catalyst, acid catalyst and lipase catalyst [10]. Different technique has been developed so far for biodiesel production like mechanical stirring, hydrodynamic cavitation, ultrasonic cavitation [11] and supercritical methanol [12].

Ji et al. [11], prepared biodiesel through Power Ultrasonic (PU) (19.7 kHz), Hydrodynamic Cavitation (HC) and Mechanical Stirring (MS). The yield of PU and HC are found to be almost similar and are better than MS. Power ultrasonic gave the shortest reaction time and the highest yield. It is found that the PU and HC processes require approximately a half of the energy that was consumed by the MS method. Stavarache et al. [13], studied low frequency ultrasound (40 kHz) with the aim of gaining more knowledge on intimate reaction mechanism with the KOH (potassium hydroxides). it was concluded that by Stavarache et al. [14] that using ultrasounds the reaction time is much shorter (10–40min) than for mechanical stirring and the quantity of required catalyst is 2 or 3 times lower.

Gogate et al. [15] performed the similar experiment on hydrodynamic cavitation, ultrasonic cavitation and mechanical stirring technique for biodiesel production under optimum operating conditions. Production of fatty acid ethyl ester (FAEE) from oleic acid (FFA) with short-chain alcohols (ethanol, propanol, and butanol) under ultrasonic irradiation was investigated by Hanh et al. [16] and it was concluded that Ultrasonic irradiation condition is efficient, time saving and economically functional for esterification of free fatty acid with short-chain alcohols to produce biodiesel fuel. The esterification of fatty acid with ethanol under ultrasonic irradiation provides a possibility for producing cheap alternative fuels, which could reduce air pollution and protect the environment. Hanh et al. [17] also investigated the biodiesel production through transesterification of triolein with various alcohols under ultrasonic irradiation (40 kHz) and mechanical stirring (1800 rot/min) conditions. It was found that the rate of the alkyl ester formation under the ultrasonic irradiation condition was higher than that under the stirring condition. Santos [18], evaluated the production of methyl esters from Oreochromis niloticus (Nile tilapia) oil and methanol. The reaction was carried out applying low-frequency high-intensity ultrasound (40 kHz) under atmospheric pressure and ambient temperature. The optimal operating condition was obtained applying an alcohol to oil molar ratio of 9.0 and a catalyst concentration of 2.0% w/w and temperature of 30 °C.

In the open literature, experimental studies on application of ultrasound energy for biodiesel production of non-edible oils are not available. Therefore, the objectives of present experimental study are to explore the possibility of production of biodiesel from non-edible oils using ultrasound energy in comparison to mechanical stirring method, followed by engine performance testing.

2. Materials

Raw *Citrullus colocyntis* (Thumba) oil, and waste cooking oil have been used for biodiesel production. These Non-edible oils are purchased from the Jodhpur district of western Rajasthan (India), whereas waste cooking oil (WCO) was obtained from Maurya Sheraton the five star hotel in Delhi and commercially available diesel oil was purchased from the nearby IOCL petrol pump.

3. Experimental work

3.1 Test rig for ultrasonic cavitation technique

The transesterification reactions were carried out in the horn type ultrasonic reactor (Figures 1 and 2). In horn type reactor the horn is attached with the transducer which produces ultrasonic irradiation in the mixture. Ultrasonic processor frequency is ranging from 25 kHz to 30 kHz and time limit is ranging from 3 min to 30 min. There is an integrated arrangement for supporting the beaker (100 ml) so as the transducer horn should be submerged at the separating boundary of two immiscible liquids. The horn of the transducer was submerged approx. 2 cm in the reactive mixture of methanol and fatty acid oil. The temperature of the reaction mixture was controlled by a water bath. Heated fatty acid oil (50 gm, 50^{o} C) was poured into the reactor at the beginning. The reaction started when a mixture consisting of desired amount of KOH was dissolved in methanol liquor KOH was poured into the heated reactor.

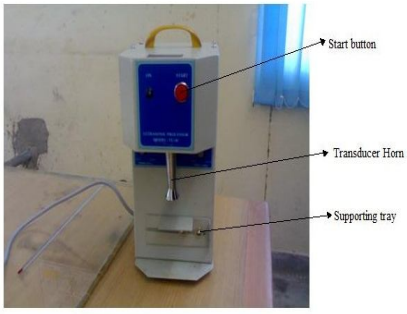

Figure 1: Photograph of ultrasonic horn type processor (TU-50)

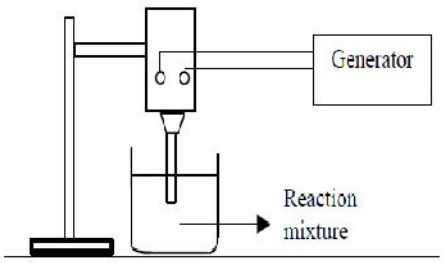

Figure 2: Schematic diagram of ultrasonic horn type reactor

The reaction is carried out by ultrasonic irradiation from the acoustic rod horn incorporated with the transducer. Cavities are created by the irradiation of power ultrasonic with sufficient energy in immiscible liquid (oil and alcohol are not miscible with each other) as a result micro fine bubbles are formed and these bubbles are collapsing at various place of the reactor and disturb the phase boundary between two immiscible liquid and resulted in emulsification of mixture.

3.2 Fuel properties

Biodiesel properties in comparison to diesel are shown in Table 1. Density is almost same for the Thumba and WCO biodiesel but higher than the diesel. Kinematic viscosity of thumba biodiesel is higher than WCO and diesel has the lowest kinematic viscosity. Flash point of WCO biodiesel is much higher than the thumba oil and diesel. Water content (0.005 w/w %) is much lower in case of diesel oil. Sulphur content in all biodiesel is lower than diesel.

Table 1: Comparison of the property of biodiesel and diesel as per BIS: 2796.

Property	Biodiesel from		Unit	Limit	Diesel
	Thumba oil	WCO	----------	----------	----------
Appearance	clear	clear	----	----	clear
Color	Brownish	Yellowish	----	----	----
Density at 15 0C	890	886	kg/m3	860-900	840
Kinematic viscosity at 40 0C	5.86 x 10-6	4.3 x 10-6	m2/sec	3.5-5 x 10-6	4.86 x 10-6
Flash point	>66	>110	0C	Min 100	51
Sulphur contents	0.01	>0.012	w/w%	Max 0.05	0.35-0.55
Water content	0.05	>0.04	w/w%	0.02-0.05	0.005

3.3 Preparation of biodiesel blends

Biodiesel blends of thumba and WCO biodiesel with diesel oil has been prepared for engine performance testing. From the literature it is evident that dilution or blending of non edible oil with other fuels like alcohol or diesel fuel would bring the viscosity close to a specified range. Therefore thumba and WCO biodiesel blends with diesel in varying proportion to reduce its viscosity. Engine experiments are performed with different blends of biodiesel (pure diesel, B-10, B-20, and B-30).

3.4 Experimental setup for performance testing

The setup consists of four cylinder, four stroke, Tata Indica diesel engine connected to eddy current type dynamometer for loading. It is provided with necessary instruments for combustion pressure and crank-angle measurements. The signals are interfaced to

computer through engine indicator for p-θ diagrams. Provision is also made for interfacing airflow, fuel flow, temperatures and load measurement. The set up has stand-alone panel box consisting of air box, fuel tank, manometer, fuel measuring unit and transmitters for air and fuel flow measurements. The setup enables study of engine performance for various engine parameters. The main aim of this experiment is to investigate the suitability and effect on performance of blending of biodiesel (produced through power ultrasound) in comparison to the gasoline diesel fuel.

4. Result and Discussion

4.1 Experimental data of biodiesel production

Vegetable oil (50g) is taken in a 100 ml beaker and filtered it to remove impurities and heated up to 120 ^{0}C in order to remove water content of oil to avoid soap formation. This oil is allowed to cool up to 60 ^{0}C temperature. Methyl alcohol (CH_3OH) with a molar ratio of (1:4.5 & 1:6) and Catalyst KOH is taken as (0.5%, 0.75% and 1%) by weight of oil. Then mixer of methyl alcohol and KOH stirred until KOH dissolve in methyl alcohol. This mixture is mixed with vegetable oil. The mixture of oil, methanol and catalyst come in contact with ultrasonic processor transducer (model TU-50) which works at the ultrasonic frequency of 28.5 kHz. During the reaction the temperature of mixture is kept between 40 -55 ^{0}C. When reaction is completed the beaker is kept for the separation. Fatty acid has higher specific weight therefore it will settle at bottom. Separation of methyl ester and glycerol will take 2 to 3 hr duration. After complete separation bio-diesel (methyl Easter) is visible in the upper layer and the lower layer as glycerol. Bio-diesel is separated from beaker for purification process. To remove the catalyst, water at around 60 ^{0}C is mixed with the methyl ester and left for settling down. Water due to its higher specific gravity collected at bottom. Excess methanol present in biodiesel has been removed by distillation process. The experiments are performed with alcohol to oil molar ratio as 6:1 and 4.5:1. The amount of oil, alcohol and catalyst taken is shown in Table 2.

Table 2: Oil, alcohol and catalyst during the experimentation.

Molar ratio (alcohol/oil)	Quantity of non-edible oil (gm)	Quantity of methanol (gm)	Catalyst (KOH)		
			0.5%	0.75%	1.0%
6:1	50 g	11 g	0.25 g	0.375 g	0.5 g
4.5:1	50 g	8.28 g	0.25 g	0.375 g	0.5 g

Time and yield produced for the different vegetable oils

Experiments have been performed to prepare biodiesel from vegetable oil (Thumba and waste cooking oil) by ultrasonic cavitation method and conventional magnetic stirring method. Main aim of this experiment to calculate reaction time, catalyst percentage and molar ratio (alcohol/oil) for biodiesel production with maximum yield

in comparison to the conventional method. Our emphasis in the present study is to reduce the use of catalyst (KOH) and alcohol because catalyst (KOH) is pollutant for the water and land. If biodiesel produce on industrial scale, large amount of catalyst will be discharged in river or land causing harm to environment. The results obtained from experiments are discussed below:

Experimental Data for Ultrasonic Cavitation Method

Experimental data are collected by performing ultrasonic cavitation on the sample which is a mixture of vegetable oil (thumba and waste cooking oil), methanol (CH_3OH) and catalyst (KOH). For every sample reaction time required for biodiesel production and yield of methyl ester is calculated. Time and yield for every sample is shown in Table 3.

Table 3: Time (Min) and yield (%) of thumba and waste cooking oil for different molar ratio and catalyst (%).

% of catalyst	Molar ratio (alcohol/oil) 6:1				Molar ratio (alcohol/oil) 4.5:1			
	Time (min)	Yield (%)	Time (min)	Yield (%)	Time (min)	Yield (%)	Time (min)	Yield (%)
0.5%	20	92.8	16	91.6	21	95.2	18	94.2
0.75%	14	90.7	15	88.7	18	93.4	16	91.3
1%	9	90	10	84	15	87.7	15	87.5

Experimental Data for Magnetic Stirring Method

For comparison purpose experiment has also been performed with magnetic stirrer. Time and yield of methyl ester for three different oil and catalyst (%) of oil is shown in table 4.

Table 4: Time (Min) and yield (%) of jatropha, thumba and waste cooking oil for different molar ratio and catalyst (%).

% of catalyst	Molar ratio (alcohol/oil) 6:1				Molar ratio (alcohol/oil) 4.5:1			
	Thumba		Waste cooking oil		Thumba		Waste cooking oil	
	Time (min)	Yield (%)	Time (min)	Yield (%)	Time (min)	Yield (%)	Time (min)	Yield (%)

0.5%	38	87	38	87.1	42	88.7	42	89.8
0.75%	34	84.2	36	85.8	39	86.3	37	87.2
1%	30	79.8	30	84.8	36	84.1	35	85.3

5. Discussion on experiment data

With the help of experimental data shown in Tables 4 and 5, graphs have been plotted to compare the power ultrasound and mechanical stirring methods applied for these non-edible oils.

5.1 Comparison for thumba oil

Comparison of ultrasonic and mechnical stirring method for molar ratio 6:1 (alcohol and oil) for different catalyst (%) is shown in Figure 3(a) and 3(b). Thumba biodiesel also exihibit lower reaction time and more yield than conventional method. Maximum yield in case of ultrasonic method for thumba biodiesel is 92.8% and lower reaction time is 9 minutes for 1% catalyst. Comparison of these two techniques for molar ratio 4.5:1 is shown in Figure 3(c) and 3(d). For this molar ratio and same catalyst (%) yield and reaction time is optimum for the ultrasonic cavitation method. It can be seen that using ultrasonic method reaction time is almost half compare to conventional method which is beneficial for industrial applications.

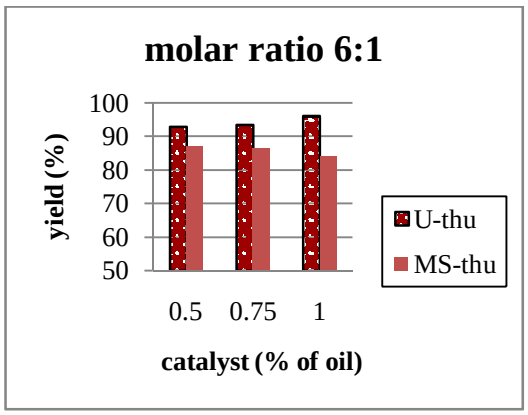

Figure 3(a): Comparison of yield for thumba biodiesel and molar ratio 6:1

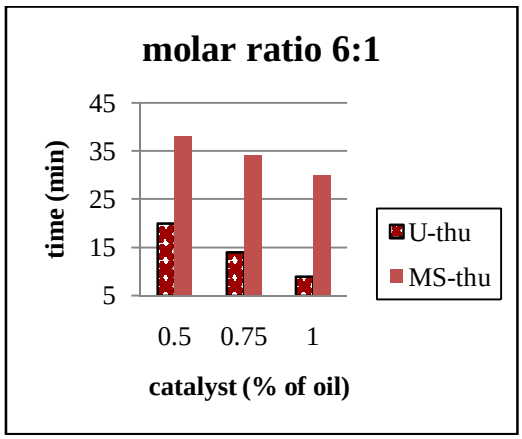

Figure 3(b): Comparison of time for thumba biodiesel and molar ratio 6:1

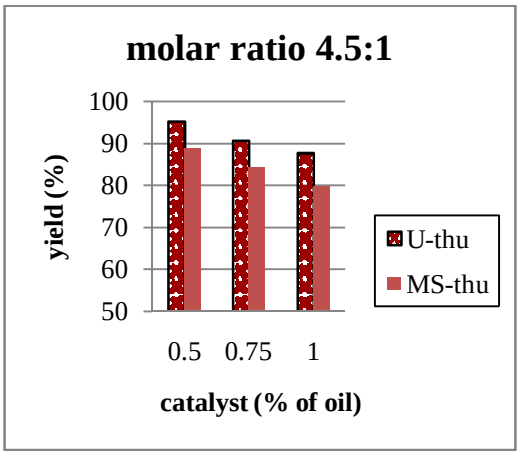

Figure 3(c): Comparison of yield for thumba biodiesel and molar ratio 4.5:1

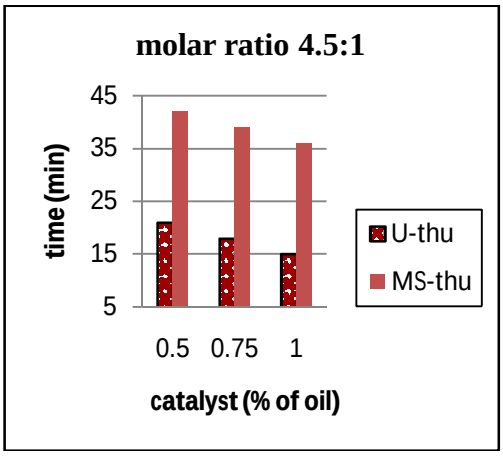

Figure 3(b): Comparison of time for thumba biodiesel and molar ratio 4.5:1

Comparison with waste cooking oil (WCO)

Similar comparison has also been performed for the waste cooking oil for molar ratio 6:1 and different catalyst (%) which is shown in Figure 4(a) and 4(b). Yield is almost same for both method for all catalyst (%) but time is much lower in case of ultrasonic cavitation method.

For molar ratio 4.5:1 (alcohol to oil) comparison between ultrasonic and magnetic stirring method is shown in Figure 4(c) and 4(d) .Yield in case of ultrasonic method higher for 0.5% and 0.75% catalyst of oil and it is lower for 1% compared to conventional method. Reaction time show similar pattern as above.

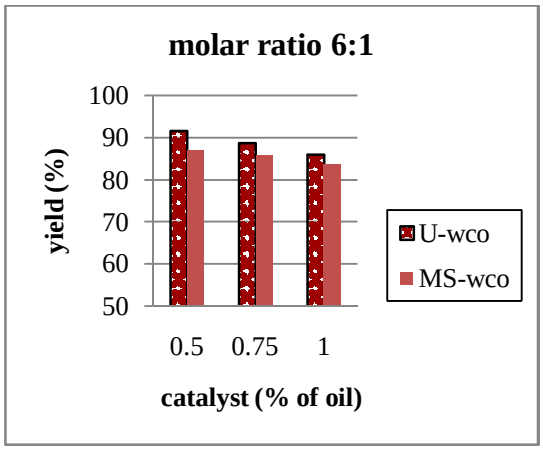

Figure 5(a): Comparison of yield for WCO biodiesel and molar ratio 6:1

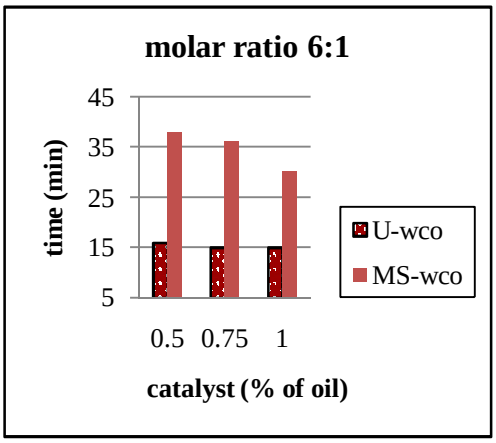

Figure 5(b): Comparison of time for WCO biodiesel and molar ratio 6:1

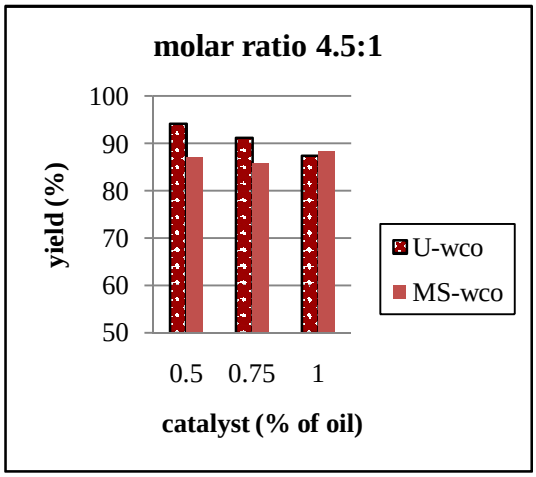

Figure 4(c): Comparison of yield for WCO biodiesel and molar ratio 4.5:1

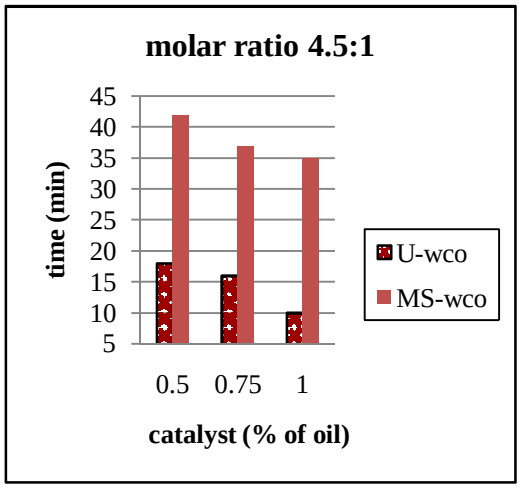

Figure 4(d): Comparison of time for WCO biodiesel and molar ratio 4.5:1

6. Performance and Emission Studies

6.1 Experimental Setup of single cylinder kirloskar Engine

The setup consists of a diesel kirloskar engine single cylinder, water cooled, direct injection, naturally aspirated, four stroke, 87.5 mm bore, 110 mm stroke and compression ratio (17.5). Diesel engine connected to eddy current type dynamometer for loading as shown in Figure 5.

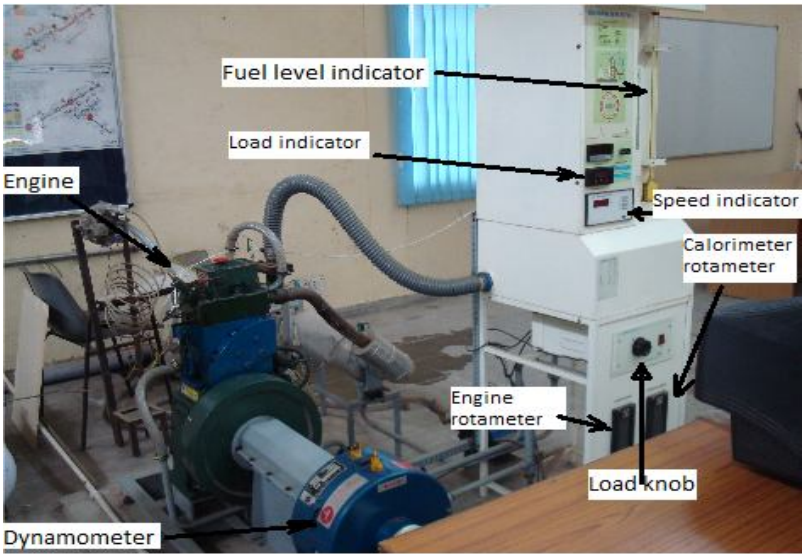

Fig. 5: Engine setup for performance and emissions test.

Variation of brake thermal efficiency w.r.t brake power

Figure 6 (a-c) shows the variation of BTE v/s brake power and % variation of BTE for thumba and WCO blends of B20, B40, B60, respectively compared with diesel. For all blends BTE increases with increases power output. The maximum percentage daviation of BTE for all blends of WCO and thumba is ± (3-10) % w.r.t. diesel operation, this narrow range of variation for wide range of brake power output shows that WCO and thumba can be similar alternative of diesel petrolium. The biodiesel produced from WCO and thumba have good combustion quality due to presence of oxygen and higher lubricity than diesel.

Variation of smoke opacity W.R.T. brake power

Shown in figures 7 (a-c) reperesents the variation of the smoke opacity with brake power for different blends of WCO and thumba biodiesel blends compared with diesel. Smoke opacity is usually found to significantly decrease with biodiesel as compared to diesel with increase in load. The smoke emissions were also sensitive to the oxygen content of the fuel and good combustion characteristics. Because of the heterogeneous nature of diesel combustion, fuel-air ratios, which affect smoke formation, tend to vary within the cylinder of a diesel engine. Smoke formation occurs primarily in the fuel-rich zone of the cylinder, at high temperatures and pressures. If the applied fuel is partially oxygenated, locally over-rich regions can be reduced and primary smoke formation can be limited. Percentage reductions is up to 40 % , higher reductions were observed with higher loads.

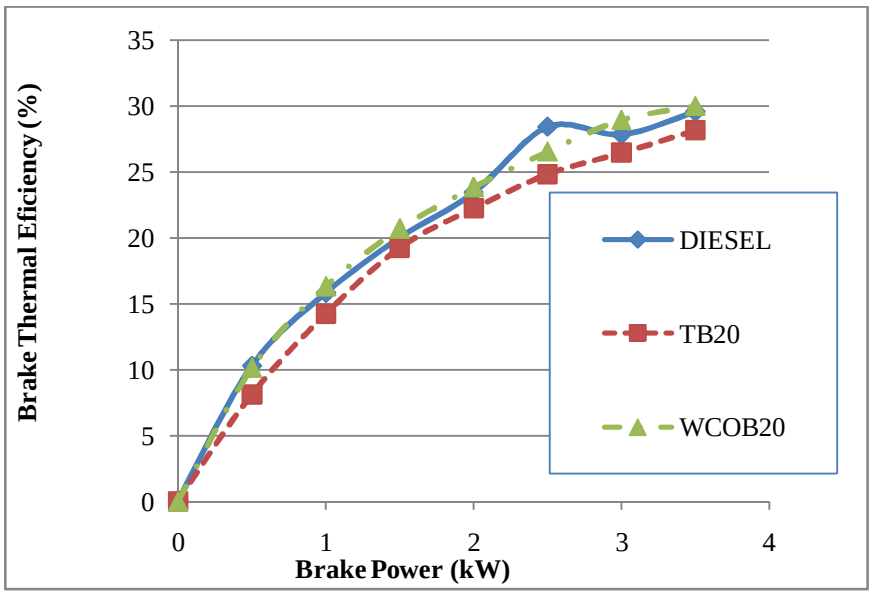

Fig. 6(a): BTE V/s Brake power of WCOB 20,TB.

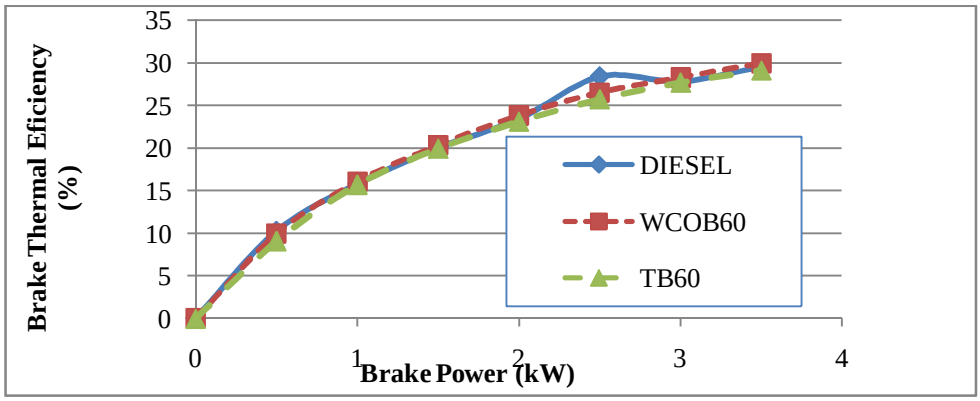

Fig. 6 (c): BTE v/s Brake power of WCOB60,TB60.

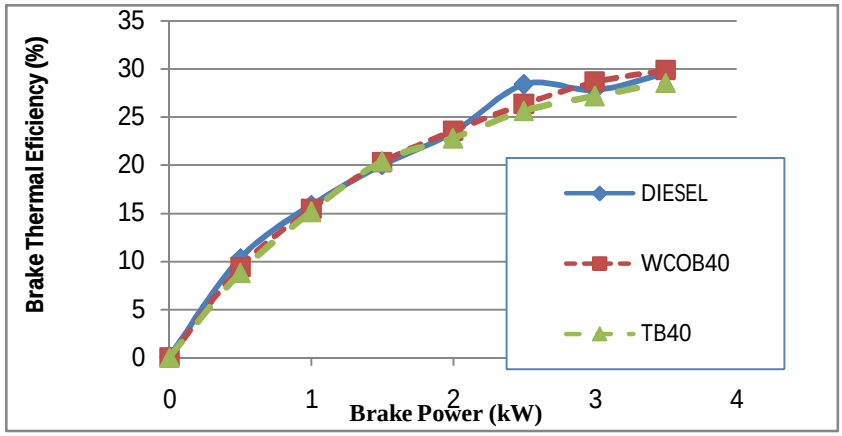

Fig. 6(b): BTE v/s Brake power of WCOB 40,TB 40.

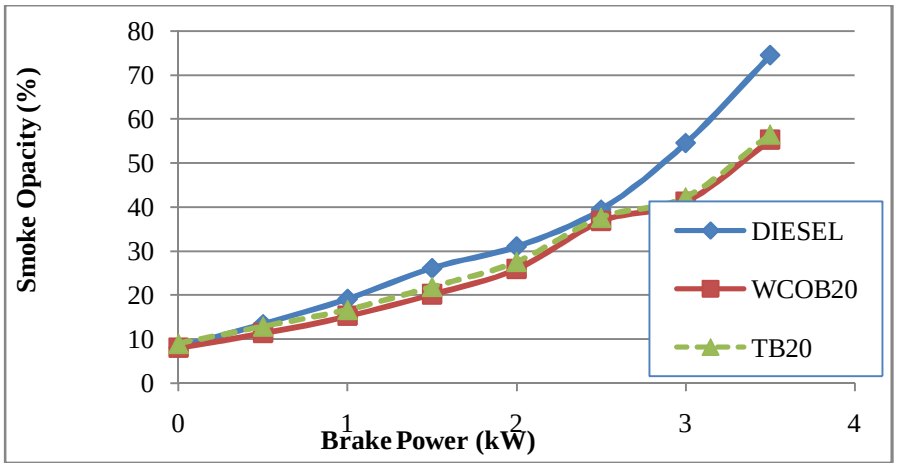

Fig. 7(a): Smoke opacity v/s Brake power of WCOB 20,TB 20.

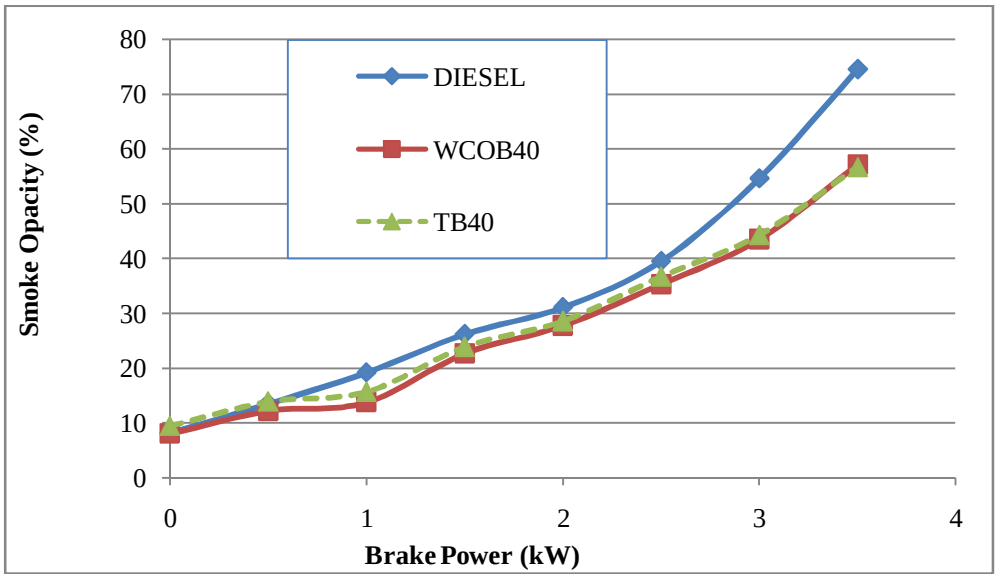

Fig. 7(b): Smoke opacity v/s Brake power of WCOB 40,TB 40.

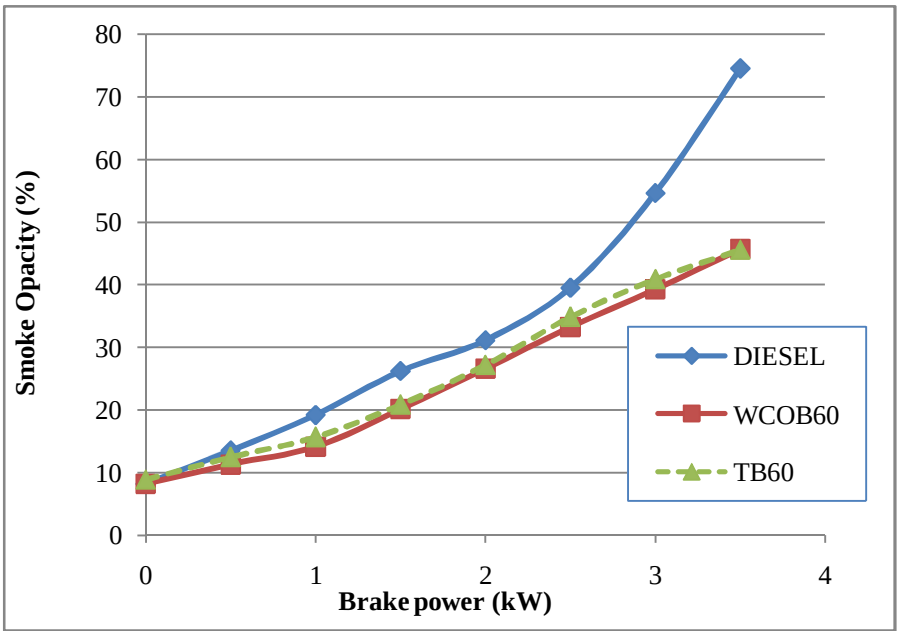

Fig. 7(c): Smoke opacity v/s Brake power of WCOB60,TB 60.

7. Conclusion

Ultrasonic cavitation method is energy efficient, environmental friendly and industrially viable alternative for the biodiesel production. Following conclusions have been made from the experiments:

1. The reaction time required for methyl ester formation is much shorter for ultrasonic cavitation method compare to conventional magnetic stirring method.
2. Relatively better yield has been obtained by ultrasonic cavitation technique compare to convention method of biodiesel production.
3. Thumba and jatropha biodiesel are potential alternative to diesel.
4. From the engine performance testing it can be concluded that the thermal efficiency parameter for both biodiesel (thumba and jatropha) have better results than the diesel oil.

References

[1] Srivastava A, Prasad R. Triglycerides based diesel fuels. Renew Sustain Energy Rev 2000; 4:111–33.

[2] Hebbal O.D., Vijaya kumar Reddy K., Rajagopal K. Performance characteristics of a diesel engine with deccan hemp oil. Fuel 85 (2006) 2187–2194.

[3] Wang YD, Al-Shemmeri T, Eames P, McMullan J, Hewitt N, Huang Y. An experimental investigation of the performance and gaseous exhaust emissions of a diesel engine using blends of a vegetable oil. Appl Thermal Eng 2006; 26:1684–91.

[4] Dmytryshyn SL, Dalai AK, Chaudhari ST, Mishra HK, Reaney MJ. Synthesis and characterization of vegetable oil derived esters: evaluation for their diesel additive properties. Bioresour Technol 2004; 92:55–64.

[5] Marchetti JM, Miguel VU, Errazu AF. Possible methods for biodiesel production. Renew Sustain Energy Rev 2005; 11:1300–11.

[6] Stavarache C, Vinatoru M, Nishimura R, Maed Y. Fatty acids methyl esters from vegetable oil by means of ultrasonic energy. Ultrason Sonochem 2005; 12:367–72.

[7] Kerschbaum S, Rinke G. Measurement of the temperature dependent viscosity of biodiesel fuels. Fuel 2004; 83:287–91.

[8] Cigizoglu KB, Ozaktas T, Karaosmanoglu F. Used sunflower oil as an alternative fuel for diesel engines. Energy Sour 1997; 19:559–66.

[9] Murugesan A., Umarani C., Chinnusamy T.R., Krishnan M., Subramanian R., Neduzchezhain N. Production and analysis of bio-diesel from non-edible oils—A review Renewable and Sustainable Energy Reviews (2008) 825-834.

[10] Miguel V, Trubiano G, Perez G, Borio DO, Errazu AF. Kinetic analysis of enzymatic esterification of fatty acids and ethanol. Stud Surf Sci Catal 2001; 133:619–24.

[11] Jianbing Ji, Jianli Wang, Yongchao Li, Yunliang Yu, Zhichao Xu. Preparation of biodiesel with the help of ultrasonic and hydrodynamic cavitation. Ultrasonics 44 (2006) 411–414

[12] Demirbas A. Biodiesel from vegetable oils via transesterification in supercritical methanol. *Energy Conv Mgmt* 2002; 43:2349–56.

[13] Stavarache Carmen, Vinatoru M., Nishimura R., Maeda Y.Fatty acids methyl esters from vegetable oil by means of ultrasonic energy. Ultrasonic Sonochemistry 12 (2005) 367–372.

[14] Stavarache Carmen, Vinatoru M., Maeda Y. Aspects of ultrasonically assisted transesterification of various Vegetable oils with methanol. Ultrasonics Sonochemistry 14 (2007) 413-417.

[15] Parag R. Gogate and Aniruddha B. Pandit. A review and assessment of hydrodynamic cavitation as a technology for the future. Ultrasonics Sonochemistry 12 (2005) 21–27.

[16] Hoang Duc Hanh, Nguyen The Dong, Kenji Okitsu, Rokuro Nishimura, Yasuaki Maeda. Biodiesel production by esterification of oleic acid with short-chain alcohols under ultrasonic irradiation condition. Renewable Energy 34 (2009) 780–783.

[17] Hoang Duc Hanh, Nguyen The Dong, Kenji Okitsu, Rokuro Nishimura, Yasuaki Maeda. Biodiesel production through transesterification of triolein with various alcohols in an ultrasonic field. Renewable Energy 34 (2009) 766–768.

[18] Francisco F. P. Santos, Jackson Q. Malveira, Márcia G. A. Cruz and Fabiano A. N. Fernandes. Production of biodiesel by ultrasound assisted esterification of Oreochromis niloticus oil. Fuel 89 (2010)275-279.

International Journal of Engineering Research & Technology (IJERT)
ISSN: 2278-0181
Vol. 2 Issue 10, October - 2013

Design and Simulation of High Speed 8-bit Vedic Multiplier Using Barrel Shifter on FPGA

Arnav Gupta
Jaypee Institute Of Information Technology

Harshit Gupta
Delhi Technological University

Abstract

Vedic mathematics[1] is an ancient technique with unique approach and it has got different sutras. Here, in this paper 'Nikhilam Navatascaramam Dasatah' Sutra is been discussed , which is efficient in speed of the multiplier.This paper describes the implementation of an 8-bit Vedic multiplier enhanced in terms of propagation delay when compared with conventional multipliers. In our design we have utilized 8-bit barrel shifter which requires only one clock cycle for 'n' number of shifts. The design is implemented and verified using FPGA and ISE Simulator.The propagation delay comparison was extracted from the synthesis report and static timing report as well. The design could achieve propagation delay of 5.323ns which is significantly less than conventional multipliers.

Keywords– vedic mathematics,multiplier,barrel shifter,delay,fpga

1. INTRODUCTION

A multiplier is one of the key hardware blocks in most of applications such as digital signal processing [2], encryption and decryption algorithms in cryptography and in other logical computations [4]. With advances in technology, many researchers have tried to design multipliers which offer either of the following high speed, low power consumption, regularity of layout and hence less area or even combination of them in multiplier. The Vedic multiplier is considered here to satisfy our requirements. Multipliers are the core component of any DSP applications and hence speed of the processor largely depends on multiplier architecture. A multiplier of size n bits has n^2 gates. For multiplication algorithms performed in DSP applications latency and throughput are the two major concerns

Vedic mathematics [1] is an ancient technique which was used in the time of Vedas. It has got as many as 12 Sutras that can be used for different Arithmetic calculation. Vedic Sutras apply to and cover almost every branch of Mathematics. They apply even to complex problems involving a large number of mathematical operations.

Vedic mathematics has proved to be the most robust technique for arithmetic operations. In contrast, conventional techniques for multiplication provide significant amount of delay in hardware implementation of n-bit multiplier. Moreover, the combinational delay of the design degrades the performance of the multiplier. Hardware-based multiplication mainly depends upon architecture selection in fpga or asic[3][5]. Application of the Sutras saves a lot of time and effort in solving the problems, compared to the formal methods presently in vogue. Though the solutions appear like magic, the application of the Sutras is perfectly logical and rational.

Since the ever growing technology and increased complexity in the design demands for the optimized area and delay. Researchers are constantly working on towards the designing of optimized multiplier architecture. Critical path delay is the key factor in determining the speed of the multiplier, In simpler form multiplication can be developed using successive addition, subtraction and shifting operation as in literature. Different algorithms are implemented for the multiplier and each technique has got its own advantage and trade off in terms speed, area, and power consumption.

Multiplier implementation using Fpga has already been reported using different multiplier architectures but the performance of multiplier was improved in proposed design by employing Vedic multiplier using modified "Nikhilam Navatascaramam Dasatah" sutra. The architecture in [1] is modified using barrel shifter by which significant amount of clock cycles are reduced by virtue of which the speed increases. The performance of the proposed multiplier is compared with the previously implemented multipliers on Fpga.

2. Nikhilam Dasatah Sutra

The Nikhilam Sutra literally means "all from 9 and last from 10". It is more efficient when the numbers

involved are large. The Nikhilam Sutra algorithm is efficient for multiplication only when the magnitudes of both operands are more than half their maximum values. For n-bit numbers, therefore both operands must be larger than 2n-1. Nikhilam Sutra is explained by considering the multiplication of two single digit decimal numbers 8 and 7 where the chosen base is 10 which is nearest to and greater than both these two numbers [6].

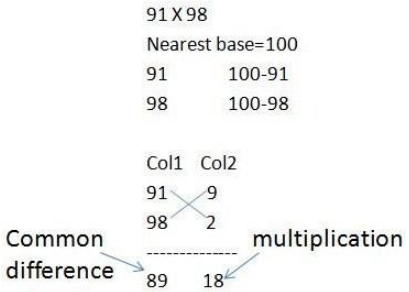

Fig1. Multiplication of Two Digit Decimal Numbers (91 x 98) using Nikhilam Sutra.

As shown in Fig.1, the multiplier and the multiplicand are written in two rows followed by the differences of each of them from the chosen base, i.e., their compliments. There are two columns of numbers, one consisting of the numbers to be multiplied (Column 1) and the other consisting of their compliments (Column 2). The product also consists of two parts which are demarked by a vertical line for the purpose of illustration. The right hand side (RHS) of the product can be obtained by simply multiplying the numbers of the Column 2 i.e., (2x9=18). Common difference is found by subtracting either (91-2=89) or (98-9).

3. PROPOSED MULTIPLIER ARCHITECTURE DESIGN

Assume that the multiplier is A and multiplicand is B. The mathematical expression for nikhilam sutra is given below.

$$P = A.B = 2\hat{}t_2(A \pm Z_2*2^{(t_1 - t_2)}) \pm Z_1*Z_2 \quad (1)$$

Where t_1,t_2 are the maximum power index of input numbers A and B respectively. Z_1 and Z_2 are the residues in the numbers X and Y respectively.

For implementing above expression , hardware is divided into three blocks.

1. Power index determinant module(PID)
2. Base selection module(BSM)
3. Multiplier.

The base selection module (BSM) is used to select the maximum base with respect to the input numbers. The power index determinant(PID) is used to extract the power index of k1 and k2. The multiplier comprises of base selection module (BSM), power index determinant (PID), subtractor, barrel shifter, as sub-modules in the architecture.

3.1 Base selection module.

It comprises of power index determinant (PID) as the sub-module along with barrel shifter, adder, average determinant, comparator and multiplexer.

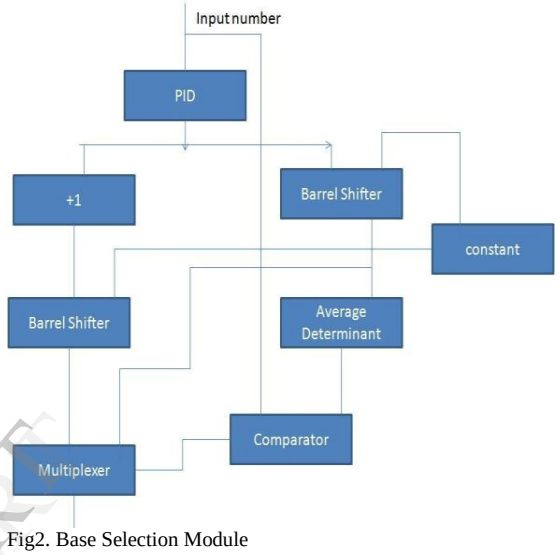

Fig2. Base Selection Module

3.2 Power index determinant.

The input number is fed to the shifter which will shift the input bits by one clock cycle. The shifter pin is assigned to shifter to check whether the number is to be shifted or not. In this power index determinant (PID) the sequential searching has been employed to search for first '1' in the input number starting from MSB. If the search bit is '0' then the counter value will decrement up to the detection of input search bit is '1'. Now the output of the decrementer is the required power index of the input number.

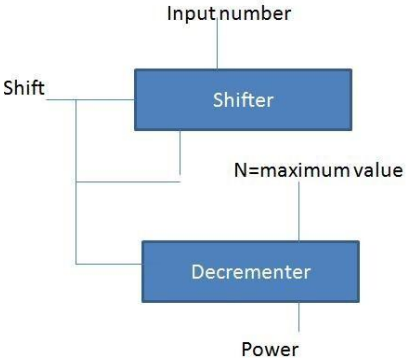

Fig3. Power Index Determinant

3.3 Multiplier Architecture

The architecture implements the equation (1). Base is obtained from BSM when the numbers are provided to it.The output of BSM and the input numbers 'A' and 'B' are fed to the subtractors.Subtractor block provides residual part Z_1 and Z_2.Power Index Determinant(PID)receives values from BSM of respective input numbers. The power of the base is found by sub-section of PID.The outputs of subtractor are fed to the multiplier that feeds the input to the second adder or subtractor[6]. Similarly the outputs of PID are fed to the third subtractor that feeds the input to the barrel shifter. The input number 'A' and the output of barrel shifter are rendered to first adder/subtractor and the output of it is applied to the second barrel shifter which will provide the intermediate value. The last sub-section of this multiplier architecture is the second adder/subtractor which will provide the required result.

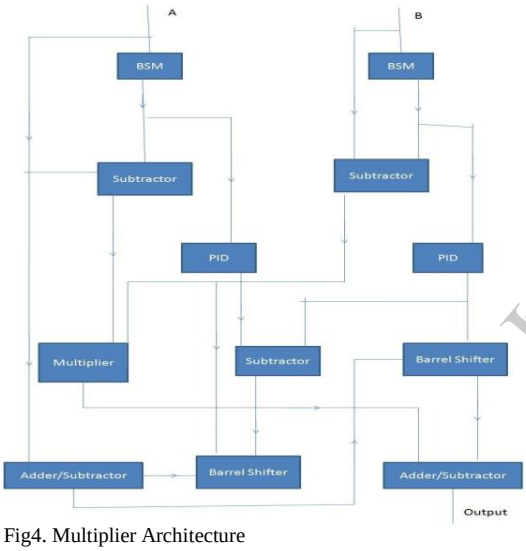

Fig4. Multiplier Architecture

4. RESULTS

Table 1. draws comparison between conventional multipliers and proposed design. Around 89.6% of reduction in delay can be observed from the proposed design with respect to array multiplier and 74.68% of reduction in delay with respect to conventional Vedic Multiplier in Table I.

Table 1. Comparison between various multipliers

Multiplier Type	Vedic Multiplier	Array Multiplier	Proposed Multiplier
Delay(ns)	21.03	51.43	5.323

5. CONCLUSION

Upon completion of the project, we achieve a high percentage of reduction in the propagation delay when compared to array multiplier and conventional Vedic multiplier implementation on FPGA.The wide ranges of applications of multiplier unit can be witnessed in VLSI and signal processing applications.The project can be extended to the power analysis of the multiplier.

6. REFERENCES

[1] Jagadguru Swami Sri Bharati Krisna Tirthaji Maharaja, *Vedic Mathematics: Sixteen Simple Mathematical Formulae from the Veda*, Delhi (1965).

[2] S. S. Kerur, Prakash Narchi, Jayashree C N, Harish M Kittur and Girish V A, "Implementation of Vedic multiplier for Digital Signal Processing", International Conference on VLSI, Communication & Instrumentation (ICVCI) 2011, Proceedings published by International Journal of Computer Applications® (IJCA), pp.1-6.

[3] Himanshu Thapaliyal and M.B Srinivas, "VLSI Implementation of RSA Encryption System Using Ancient Indian Vedic Mathematics", Center for VLSI and Embedded System Technologies, International Institute of Information Technology Hyderabad, India.

[4] Jagadguru Swami Sri Bharati Krishna Tirthaji Maharaja, "Vedic Mathematics: Sixteen simple Mathematical Formulae from the Veda", Delhi(1965).

[5] Devika, K. Sethi and R.Panda, "Vedic Mathematics Based Multiply Accumulate Unit," 2011 *International Conference on Computational Intelligence and Communication Systems*, CICN 2011, pp.754-757, Nov.2011.

[6] Q. LI, G. LIANG, and A. BERMAK, "A High-speed 32-bit Signed/Unsigned Pipelined Multiplier," *IEEE 5th Int. Sym-posium Electronic Design, Test and Application*, pp.207- 211, Jan. 2010.

[7]S.S.Kerur,Prakash.Narchi,Jayashree.C.N,Harish.M. Kittur and Girish.V.A," Implementation of Vedic Multiplier for Digital Signal Processing" *International Conference on VLSI, Communication & Instrumentation (ICVCI)* 2011, *Proceedings published by International Journal of Computer Applications® (IJCA).*

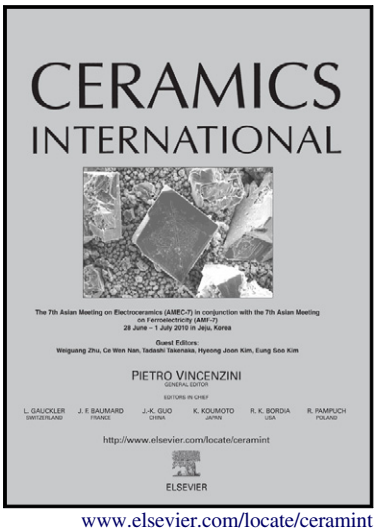

www.elsevier.com/locate/ceramint

Effect of holmium substitution on structural and electrical properties of barium zirconate titanate ferroelectric ceramics

Priyanka A. Jha, A.K. Jha

PII: S0272-8842(13)01357-6
DOI: http://dx.doi.org/10.1016/j.ceramint.2013.10.087
Reference: CERI7514

To appear in: *Ceramics International*

Received date: 26 August 2013
Revised date: 21 October 2013
Accepted date: 21 October 2013

Cite this article as: Priyanka A. Jha, A.K. Jha, Effect of holmium substitution on structural and electrical properties of barium zirconate titanate ferroelectric ceramics, *Ceramics International,* http://dx.doi.org/10.1016/j.ceramint.2013.10.087

Effect of holmium substitution on structural and electrical properties of barium zirconate titanate ferroelectric ceramics

Priyanka A. Jha[1] and A.K.Jha[1, 2*]

[1]Thin Film & Material Science Laboratory

Department of Applied Physics

Delhi Technological University (Formerly Delhi College of Engineering)

Bawana Road, Delhi- 110042, India.

[2]Department of Applied Sciences

A. I. A. C. T. R., Geeta Colony

Delhi- 110031, India.

Ph. No. : +9198 68 24 21 50, Fax No. : +91 11 27 87 10 23

Abstract

The holmium substituted $Ba_{1-3x/2}Ho_x Zr_{0.025}Ti_{0.975}O_3$ (x=0.01, 0.02, 0.025, 0.05) compositions were synthesized by the solid state reaction technique. The synthesized specimens were characterized for their structural and electrical properties using X-ray diffractometer, scanning electron microscopy, impedance analyzer and loop tracer. Phase analysis shows the formation of secondary phase $Ho_2Ti_2O_7$ for Ho $\geq$ 2.5 mol% substitution. The microstructural investigation shows that the holmium substitution significantly reduces the grain size. The substitution of holmium increases the Curie temperature for $x \leq 0.02$ whereas Curie temperature decreases for $x \geq 0.025$. The maximum dielectric constant at transition temperature is observed for x = 0.02. The solubility limit is 2 mol% and for $x \geq 0.025$ some of the holmium atoms enter B-sites and forms the secondary phase. An increase is observed in the coercive field of the specimens with the increasing holmium content.

Keywords: D. Ferroelectricity; A. ceramics; C. X-ray diffraction.

Corresponding author *

Email: prof.akjha@gmail.com (A.K.Jha)

1. Introduction

The phase transition temperature, nature of the phase transition and the electrical properties of the barium titanate ($BaTiO_3$) have been modified by substituting isovalent and aliovalent ions at either Ba^{2+} site (A- site) or Ti^{4+} site (B- site) or at both the sites. The Ba-site substitution with the aliovalent cations either increases or decreases the Curie temperature (T_c) without much influence on the broadening of the phase transition [1]. The lead-free environmentally friendly ABO_3 perovskite $Ba_{1-x}Sr_xTiO_3$ (BST) has been widely studied due to its application in microwave tunable devices, such as the phase shifter, tunable filter, resonator and oscillators [2-7]. However, large dielectric loss restricts its practical applications in tunable microwave devices [8]. On the other hand, the substitution at Ti sites with Zr cations is the possible alternative for the application in tunable devices because Zr^{4+} is chemically more stable than Ti^{4+} ions [9]. The partial substitution of Zr at Ti sites increases the chemical stability of barium zirconate titanate than substituted $BaTiO_3$. The chemical stability of BZT is more than BT due to the substitution of more chemically stable zirconium onto the Ti sites. In pure BT, Ti^{4+} can change to Ti^{3+} whereas in BZT, zirconium remains in Zr^{4+} state [9]. The holmium substitution has been done at optimized zirconium content and processing conditions i.e. 2.5 mol % of Zr substitution [10].

Rare earth ion substitution [11-13] studies have been carried out to understand their influence; however, major concern is on their solubility levels and the occupancy of the substituted rare earth ions in BZT structure. An extensive literature survey revealed that there are very few reports on the microstructural characterization and electrical properties of the rare earth substituted $BaZr_{0.025}Ti_{0.975}O_3$ and correlation between the microstructure and

maximum permittivity is not clearly understood [14-17]. The increase in dielectric constant is attributed to the formation of barrier layer capacitors and the resultant Maxwell-Wagner polarization or interfacial polarization [18]. This polarization often occurs in materials with the grains surrounded by the insulating grain boundary. This prompted the authors to conduct a detailed study on the effect of Ho substitution in $BaZr_{0.025}Ti_{0.975}O_3$ compound and characterize the structural and electrical properties.

2. Experimental

$Ba_{1-3x/2}Ho_x$ $Zr_{0.025}Ti_{0.975}O_3$ compositions with x=0.01, 0.02, 0.025, 0.05 were synthesized by the solid state reaction technique taking high purity $BaCO_3$, TiO_2, ZrO_2 and Ho_2O_3 (all from M/s Aldrich, USA) in their stoichiometric proportions. The powder mixtures were thoroughly ground in an agate mortar and passed through a sieve of appropriate size. The powder mixture was then calcined at 1150^{o}C for 2 hours in an alumina crucible. The calcined mixtures were grounded and admixed with polyvinyl alcohol (PVA) as a binder and then pressed at 150 MPa into disk shaped pellets. The pellets were then sintered at 1300^{o}C for 2 hours in air. X- ray diffractograms of all the sintered samples were recorded using a Bruker X-ray diffractometer with CuKα (λ=1.5406 A^o) radiations in the range $10^o \leq 2\theta \leq 70^o$ at a scanning rate of 1^o/ minute. The microstructural studies of the samples were carried out using scanning electron microscope (Hitachi S-3700N). The sintered pellets were polished and silver paste was applied on both sides to act as electrodes and then cured at 300 ^{o}C for 30 min. The dielectric measurements were carried out in the temperature range of room temperature to 300^{o}C at different frequencies 1 kHz, 10 kHz and 100 kHz using a high precision impedance analyzer (HP 4284A) at an oscillation amplitude of 1 volt. P-E hysteresis loops were recorded at room temperature using an automatic hysteresis loop tracer based on Sawyer- Tower circuit. The dielectric measurements for the unsubstituted data i.e. BZT has been published somewhere else [10].

3. Results and Discussions

3.1 Structural Analysis

Fig. 1(a) shows the X-ray diffractograms of the studied samples and reveal the formation of perovskite structure with tetragonal phase. The structure of the holmium substituted samples has been analyzed by Rietveld analysis using FULL PROF software package (Fig. 1(b)). Fig. 1(b) shows the Rietveld refinement of the studied compositions. It is concluded that the compositions possess tetragonal structure (P4mm). Further, the Bragg R-factor, RF-factor and χ^2 has been mentioned in Fig. 1(b). The diffraction peaks shift towards the higher angle with the increasing holmium (Ho) content. This is possibly due to the fact that the ionic radius of Ho^{3+} ions (0.90Å) is lower than that of Ba^{2+} ions (1.35 Å) indicating that the Ho atoms occupy Ba site. For x > 0.02, a secondary phase $Ho_2Ti_2O_7$ [13] is formed as some of the Ho^{+3} atoms enter Ti sites [18] and intensity of secondary phase is increasing for x ≥ 0.025. Moreover, the splitting of tetragonal peaks (100) and (001); (200) and (002) is observed at $2\theta=22.355^o$, 45.262^o respectively indicating that the growth of tetragonal phase [19]. This is attributed to the distortions in the original BZT structure with the substitution of Ho at Ba sites.

When Ba sites are occupied by Ho atoms, an electronic compensation is formed with the formation of barium vacancies $V_{Ba}^{X}, V_{Ba}', V_{Ba}''$ (where V_{Ba}^{X} denotes neutral barium vacancy, V_{Ba}' denotes barium vacancy with single -ve charge, V_{Ba}'' denotes barium vacancy with double -ve charge) [20]. Hence the substitution process can be represented by the following Kroger-Vink Equation as:

$$Ho_2O_3 \xrightarrow{BaO} 2Ho_{Ba}^{\bullet} + V_{Ba}'' + 3O_O^X \ldots\ldots\ldots\ldots\ldots\ldots (1)$$

It is well known that Ti^{4+} ions are chemically less stable than Zr^{4+} [21] ions as the bond dissociation energy 117.6 kJ/mol is much less than the bond formation energy 473 kJ/mol.

Therefore, it is assumed that traces of TiO_2 are lost in the sintering process leaving titanium and oxygen vacancies as shown in Eq.1

$$Ti_{Ti} + 2O \rightarrow V_{Ti}'''' + 2V_O^{\bullet\bullet} + TiO_2 \uparrow \quad \ldots\ldots\ldots\ldots\ldots\ldots (2)$$

With the increase in Ho^{3+} content, some of the Ho^{3+} ions occupy Ti sites rather than Ba sites (as shown in Fig.1 (inset)), there is a secondary pyrochlore phase of $Ho_2Ti_2O_7$. The phenomenon occurs in two stages. In the first stage,

$$Ho^{\bullet\bullet\bullet} + V_{Ti}'''' \rightarrow Ho_{Ti}' \quad \ldots\ldots\ldots\ldots\ldots\ldots (3)$$

In the second stage, Ho^{3+} tends to substitute B-site ions (Ti^{4+} and Zr^{4+}) and more oxygen vacancies are created, as shown in Eq.4

$$Ho_2O_3 \xrightarrow{B=ZrO_2/TiO_2} 2Ho_{Ti}' + 3O_O^X + V_O^{\bullet\bullet} \quad \ldots\ldots\ldots\ldots\ldots\ldots (4)$$

where '•' represents +ve charge and ''represents -ve charge.

Moreover, the lattice parameters are decreasing with the increase in Ho content as shown in Table 1.

3.2 Surface Morphology

It is well known that the diffusion coefficient is directly proportional to the sintering temperature and inversely proportional to the radius of the diffusing particles [22]. The microstructure has been examined using SEM and the obtained micrographs are shown in Fig.2. The specimen with Ho content (x=0.01) has smaller grains. For x=0.02 well developed

grains with uniform grain distribution are observed whereas for $x \geq 0.025$, grain size reduces and a porous microstructure is observed.

3.3 Dielectric Study

Fig.3 shows the temperature dependence of dielectric constant of the studied specimens at 1 kHz, 10 kHz and 100 kHz. The figures show that the value of dielectric constant increases gradually to a maximum value (ε_m) with increasing temperature up to the transition temperature and then decreases gradually indicating the phase transition. A diffuse phase transition with the substitution of holmium is observed [9].

There is an increase in the value of maximum dielectric constant at Curie temperature for 10 kHz frequency for x = 2 mol% and a gradual decrease has been observed for $x \geq 0.025$. The value of maximum dielectric constant is highest for x=0.02 which is due to the well developed grains observed in Fig.2. The well developed grains make the domain wall motion easier and hence higher value of dielectric constant [18]. The increase in dielectric constant can be understood as follows: As the sintering is carried out in air reoxidation takes place around the grains during the cooling process and hence the lattice picks up oxygen from the ambient. The reoxidation results in the formation of strong insulating layer around grains with higher resistance. This creates a difference in the conductivity of bulk and grain boundary. As grain boundary is responsible for the large resistance and capacitance compared to the grain which leads to the surface charge accumulation and consequent increase in interfacial polarization [23, 24]. This results in an increase in the dielectric constant of the specimen [9].

Further, Curie temperature increases on Ho substitution for $x \leq 0.02$ and for $x \geq 0.025$, the Curie temperature decreases. This can be understood as follows: The bond dissociation energy for Ba-O bond is 562 kJ/mol and the bond dissociation energy for Ho-O bond is 606 kJ/mol. The Zr-O bonds (776.1 KJ/mol) are stronger than Ti-O bonds (672.4

KJ/mol) [25]. As mentioned earlier, Ho atoms start entering Ti sites (B-sites) after 2 mol% of Ho substitution and the formation of Ho-O bonds take place. For the lower Ho content, Ba-O bonds are larger in number than Ho-O bond and Ti-O bond is stronger than Ba-O bond. This will lead to the stronger interactions between Ti^{4+} ions and O^{2-} ions in the TiO_6 octahedra and the occurrence of phase transition at comparatively higher temperature. For $x \geq 0.025$, the number of Ho-O bonds increases and Ho-O bonds are stronger than Ti-O bonds; this will lead to the weaker interactions between Ti^{+4} ions and O^{-2} ions in the TiO_6 octahedra and the decrease of Curie temperature (T_c) [26-28].

Fig. 3(b) shows the dielectric loss as a function of temperature for the studied specimens. It is observed that the loss is independent of temperature up to 200^{o}C at lower frequencies and then increases rapidly with the increase in temperature. This sharp increase of dielectric loss in high temperature region is attributed to the increased mobility of charge carriers arising from the defects or vacancies in the sample [29]. The behavior is also attributed to the domain boundary vibrations or excitations that are readily stimulated under the weak a.c. drive conditions [30]. The loss peaks observed in the plots are associated with the phase transitions. The increase in tan δ could be due to the associated domain dissolution at the transition temperature [30].

There is a broad dielectric constant versus temperature curve in the transition temperature region leading to the diffuse phase transition, as seen in Fig.3 (a). A diffuse phase transition is generally characterized by: (a) broadening in the dielectric constant ( ) versus temperature (T) curve; (b) a relatively large separation (in temperature) between the maximum of the real (dielectric constant) and imaginary (dielectric loss) parts of the dielectric spectrum; (c) a deviation from Curie-Weiss law in the vicinity of T_m and (d) frequency dispersion of both ε and tan δ in the transition region thereby implying a frequency dependence of T_m [31].

The broad dielectric constant temperature curve is attributed to the tolerance factor of the perovskite structure. The strain in the structure is characterized by Goldschmidt tolerance factor [32]. For perovskites with the general formula of ABO_3, the following equation is used to calculate the tolerance factor, t:

$$t = \frac{R_O + R_A}{\sqrt{2}(R_B + R_O)} \quad \text{.....(5)}$$

where R_A, R_B and R_O are the respective radii of the A- site, B- site and O atoms.

For the composition in the present work, the above equation can be rewritten as:

$$t = \frac{R_O + xR_{Ho^{+3}} + (1-3x/2)R_{Ba^{+2}}}{\sqrt{2}((0.025)R_{Zr^{+4}} + (0.975)R_{Ti^{+4}} + R_O)} \quad \text{.....(6)}$$

For a stable perovskite structure, value of t should be unity. As t changes, the normal ferroelectric phase gets destabilized [33]. The Ho^{3+} ion substitution at A- site will induce normal ferroelectric behavior due to the lower ionic diameter as it reduces the value of tolerance factor from 0.91 for x=0.01 to 0.895 for x=0.05 (Table1). The disorderness in the system will lead to the diffuse phase transition and enhanced ferroelectric properties.

A modified Curie-Weiss law [34] has been proposed to describe the diffuseness of the phase transition using the empirical relation

$$(1/\varepsilon - 1/\varepsilon_m) = (T - T_m)^{\gamma}/C' \text{.....(7)},$$

where, ε is relative permittivity at temperature T and ε_m is maximum relative permittivity at temperature T_m, C' is Curie constant. The parameter γ is regarded as a measure of the diffuseness of the phase transition: $\gamma = 1$ corresponds to the normal ferroelectric behavior while $1 < \gamma < 2$ corresponds to the diffuse phase transition. The plots of $\ln(1/\varepsilon - 1/\varepsilon_m)$ as a function of $\ln(T - T_m)$ for the different Ho content at different frequencies are shown in Fig.4.

The values of diffusivity constant calculated from Fig. 4 are increaing (Table 2) with the increase in Ho content showing the disorderness in the system [35].

3.4 Conductivity studies

DC conductivity

Fig.5 shows the effect of the temperature on the dc electrical conductivity (σ) of all the samples. In all the samples, conductivity decreases with the increase in temperature up to Curie temperature and then it increases subsequently. The decrease in conductivity is due to decrease in the drift mobility of the charge carriers [36]. Table 2 lists the values of activation energy in the ferroelectric and paraelectric region for the studied samples, using Fig. 6 and the Arrhenius equation:

$$\sigma_{dc} = \sigma_o \exp\left(\frac{-E_a}{k_B T}\right) \text{.....(8)}$$

where k_B is the Boltzmann constant. It is known that the specimen with a smaller grain size contains higher number of grain boundaries resulting in higher contribution of grain boundary resistance towards the overall resistance [37]. The observed existence of two activation energies may be associated with the structural changes taking place at transition temperature [38]. It is well known that conductivity in ferroelectrics is a complex phenomenon. It is affected by the presence of defects, vacancies, imperfections and changes in lattice parameters [37]. These materials are sintered at higher sintering temperature where they are expected to lose traces of oxygen as per the following representation:

$$O_O \leftrightarrow \frac{1}{2} O_2 + V_O^{\bullet\bullet} + 2e' \text{.....(9)}$$

where all the species are written in accordance with Kroger- Vink equation of defects. The conduction is due to the singly and doubly charged oxygen vacancies [39]. For the formation

of singly charged oxygen vacancies, the value of activation energy lies in the range of 0.2-0.4eV and for the doubly charged oxygen vacancies the value of activation energy lies in between 0.8-1.0eV [39]. As seen in the Table 2, the values of activation energy lie in between 0.7- 1.0eV, therefore, the observed conductivity variations are attributed to the doubly charged oxygen vacancies in the specimens.

3.5 Ferroelectric studies

Fig. 6 shows the hysteresis loops of the studied specimens recorded at room temperature. The P-E hysteresis loops are saturated indicating the ferroelectric nature of the compounds [40]. The remanent polarization ($2P_r$) increases for $x \leq 0.02$ and decreases for $x \geq 0.025$. The variation in remanent polarization can be understood on the basis of grain size. There are two major effects of grain boundary on polarization. The smaller grain size results in the large number of grain boundaries [41] and it is well known that grain boundaries are low permittivity regions, hence poor ferroelectricity. On the other hand there is polarization discontinuity between bulk and grain boundary and hence remanent polarization ($2P_r$) decreases. The coercive field decreases for $x \leq 0.02$ and for $x \geq 0.025$, coercive field increases. This is attributed to the reduction of energy barrier for switching ferroelectric domain with the increase in grain size. Polarization reversal of a ferroelectric domain is easier inside a larger grain compared to that in a smaller grain.

3.6 Piezoelectric Studies

Fig.7 shows the variation of piezoelectric constant (d_{33}) with x. The piezoelectric properties in ferroelectric materials arise from the electrostriction coupling with spontaneous polarization P_s expressed as [42]:

$$d_{33} = 2\, \varepsilon_{33}\, \varepsilon_o\, k_{33}\, P_s \qquad (10)$$

where ε_{33} is the dielectric constant, ε_o is dielectric constant of free space. The electrostrictive coupling originates from the anharmonic motion of dipoles in the materials and this causes a change in the lattice parameter and produces a strain.

There are two major contributions to the piezoelectric coefficients: extrinsic and intrinsic. Influence of grain size, preferred orientation and the morphotrophic phase boundary condition determines the intrinsic component of the piezoelectric constant in the specimens [43, 44]. The extrinsic contribution is related to 180^o and 90^o domain wall motion in the specimens [45]. For $x \leq 0.02$ the value of piezoelectric coefficient increases initially but for $x \geq 0.025$, the value of the coefficient decreases. As seen in the SEM micrographs, the grain size increases for $x \leq 0.02$ and then grain size decreases for $x \geq 0.025$. The grain size affects the coercive field (E_c) and low E_c values facilitate the orientation of ferroelectric domains during electrical poling and hence the intrinsic responses of the piezoelectric constant [46]. On the other hand, near the Curie temperature, lattice distortion introduces large strains in the individual grains leading to domain structures that influence permittivity and hence piezoelectric constant [47].

3.7 Pyroelectric Studies

Fig.8 shows the temperature variation of pyroelectric coefficient of all the samples. The pyroelectric coefficient relates a change in temperature to a change in electrical displacement D ($\mu C/m^2$) as change in temperature causes variation in spontaneous polarization. The pyroelectric current depends on the rate of change of temperature and the pyroelectric coefficient is the constant of proportionality between electric displacement and temperature [48]

$$p = \frac{P_I}{A(dT/dt)} \qquad (11)$$

where p is pyroelectric coefficient, P_I is pyroelectric current, A is the area of electrodes and dT/dt is the rate of change of temperature.

The pyroelectric coefficient passes through a peak at a temperature lower than the ferroelectric transition temperature (T_c). The maximum pyroelectric coefficient increases for $x \leq 0.02$ but for $x \geq 0.025$, the pyroelectric coefficient decreases considerably.

The pyroelectric coefficient is represented as [49]:

$$p_i^{\sigma} = (\partial P_s / \partial T)_{E,S} + d_{31}(C_{11}\alpha_1 + C_{12}\alpha_1 + C_{13}\alpha_3) + d_{33}(2C_{13}\alpha_1 + C_{33}\alpha_3) \quad (12)$$

where p_i^{σ} is the total pyroelectric coefficient measured at constant stress and $(\partial P/\partial T)_{E,S}$ is the primary pyroelectric coefficient which is defined as the change in spontaneous polarization with temperature. The next two terms represent the secondary pyroelectric effect which is contributed by the piezoelectric effect because the thermal expansion generates a strain on the change in temperature. The constants d_{31} and d_{33} are the piezoelectric coefficients, C_{11}, C_{12}, C_{13} represent the elastic stiffness coefficients and α_1 and α_3 are the linear expansion coefficients in the I and III directions. The terms E, S and σ represent the constants electric field, strain and stress respectively.

The piezoelectric coefficient, d_{33} at x=0.02 is higher than the other studied samples as shown in Fig. 7, therefore the secondary pyroelectric coefficient would be greater than the primary pyroelectric coefficient [49]. It is known that in diffuse phase transition, the rate of change of spontaneous polarization with temperature is maximum at a temperature below T_c which has been confirmed in the present work [50]. This is attributed to the crystal deformation due to the substitution of Ho^{3+} ions on the Ba^{2+} sites, i.e., secondary pyroelectric effect.

4. Conclusions

The specimens $[Ba_{1-3x/2}\ Ho_x](Zr_{0.025}Ti_{0.975})O_3$ with different Ho concentrations were synthesized by solid state reaction method. X-ray diffractograms show that the specimens have tetragonal structure at room temperature. Secondary phases are not detected in the samples up to 2 mol % of Ho content. Moreover, the substitution of Ho has reduced the

lattice parameters and unit cell volume. The solid solubility limit is found to be 2.5 mol% of Ho and after that some of the holmium atoms enter B-sites and forms the secondary phase $Ho_2Ti_2O_7$ for Ho ≥ 2.5 mol% substitution. The dielectric constant and remanent polarization is found to be higher at x=0.02. The piezoelectric and pyroelectric coefficients are found to be maximum at x=0.02 proving the suitability for infrared detectors applications.

References

1.B. Jaffe, W. R. Cook, Jr. and H. Jaffe, Piezoelectric Ceramics, Academic Press, New York, London,1971 p. no. 91.

2. T. Yamada, V.O. Sherman, A. Noth, P. Muralt, A.K. Tagantsev, N. Setter, Epitaxial⁄amorphous $Ba_{0.3}Sr_{0.7}TiO_3$ film composite structure for tunable applications Appl. Phys. Lett. 89 (2006) 032905.

3. M.W. Cole, W.D. Nothwang, J.D. Demaree, Integration of $Ba_{1-x}Sr_xTiO_3$-based active thin films with silicon-compatible materials and process science protocols to enable affordable on-the-move communications technologies, J. Appl. Phys. 98 (2005) 024507.

4. H.S. Kim, T.S. Hyun, H.G. Kim, I.D. Kim, T.S. Yun, J.C. Lee, Orientation effect on microwave dielectric properties of Si-integrated $Ba_{0.6}Sr_{0.4}TiO_3$ thin films for frequency agile devices, Appl. Phys. Lett. 89 (2006) 052902.

5. C. Fu, F. Pan, H. Chen, S. Feng, W. Cai, C. Yang, Coplanar pahse shifters based on ferroelectric thin films, Int. J. Infrared Milli. Waves 28 (3) (2007) 229–235.

6. C.L. Chen, J. Shen, S.Y. Chen, G.P. Luo, C.W. Chu, F.A. Miranda, E.W.V. Keuls, J.C. Jiang, E.I. Meletis, H.Y. Chang, Epitaxial growth of dielectric $Ba_{0.6}Sr_{0.4}TiO_3$ thin film on MgO for room temperature microwave phase shifters, Appl. Phys. Lett. 78 (2001) 652.

7. W. Zhu, O.K. Tan, J. Ding, J.T. Oh, Preparation, Property, and Mechanism Studies of Amorphous Ferroelectric (Ba, Sr)TiO_3 Thin Films for Novel Metal–ferroelectric–metal Type Hydrogen Gas Sensors**,** J. Mater. Res. 15 (6) (2000) 1291–1302.

8. H. Chen, C. Yang, J. Zhang, B. Wang, Hong Ji, Electrical behavior of $BaZr_{0.1}Ti_{0.9}O_3$ and $BaZr_{0.2}Ti_{0.8}O_3$ thin films, Appl. Surf. Sci. 255 (2009) 4585-4589.

9. D. Hennings, A. Schnell, and G. Simon, Diffuse ferroelectric phase transitions in Ba (Ti_{1-y} Zr_y) O_3 ceramics J. Am. Ceram. Soc. **65**, 539 (1982). Priyanka Arora Jha and A.K. Jha, J Mater Sci: Mater Electron (2013) 24:1511- 1518.

10. Z. Yu, R. Guo, A.S. Bhalla, Dielectric behavior of $Ba(Ti_{1-x}Zr_x)O_3$ single crystals, J. Appl. Phys. 88 (2000) 410; Priyanka A. Jha and A.K. Jha, J Alloy Comp. 513 (2012) 580-585.

11. M. T. Buscaglia, V. Buscaglia, M. Viviani, P. Nanni, and M. Hanuskova, Influence of foreign ions on the crystal structure of $BaTiO_3$, J. Eur. Ceram. Soc. **20**, 1997 (2000).

12. Y. Tsur, A. Hitomi, I. Scrymgeour, and C. A. Randall, Site occupancy of rare earth cations in $BaTiO_3$ Jpn. J. Appl. Phys., Part 1 40, 255 (2001).

13. D. Makovec, Z. Samardzija, and M. Drofenik, Solid solubility limit of Holmium, Yttrium and Dysprosium in $BaTiO_3$, J. Am. Ceram. Soc. 87, 1324 (2004).

14. Finlay D. Morrison, Derek C. Sinclair, and Anthony R. West, Electrical and structural characteristics of lanthanum-doped barium titanate ceramics, J. Appl. Phys. 86, 6355 (1999).

15. Jin Hyun Hwang and Young Ho Han, Dielctric properties of erbium doped barium titanate, Jpn. J. Appl. Phys., Part 1 40, 676 (2001).

16. Y. Pu, W. Chen, S. Chen, and Hans T. Langhammer, Microstructure and dielectric properties of dysprosium doped barium titanate ceramics, Ceramica (Sao Paulo, Braz.) 51, 214, (2005).

17. Y. Wang, L. Li, J. Qi, and Z. Gui, Ferroelectric characteristics of ytterbium-doped barium zirconium titanate ceramics, Ceram. Int. 28, 657 (2002).

18. S. Bhaskar Reddy, M. S. Ramachandra Rao and K. Prasad Rao, Observation of high permittivity in Ho substituted $BaZr_{0.1}Ti_{0.9}O_3$ ceramics Appl. Phys. Lett. 91, 022917 (2007).

19. Sheela Devi, Jha A.K., Phase transitions and electrical characteristics of tungsten substituted barium titanate, Physica B 404 (2009) 4290-4294.

20. D. Shan, Y. F. Qu, J. J. Song, Dielectric properties and substitution preference of yttrium doped barium zirconium titanate ceramics, Solid State Commun 141 (2007), 65-68.

21. Ingeborg Kaus, Kjell Wiik, Kjersti Kleveland, Bente Krogh, Siv Aasland, Oxygen transport properties in $La_{1-x}Sr_xFe_{1-y}M_yO_{3-\delta}$ (M = Cr, Ti), $0.2 < x < 0.8$, $0.2 < y_{Ti} < 0.5$, $0.1 < y_{Cr} < 0.5$, Solid State Ionics, 178 (2007) 817–826.

22. K. Huang, Statistical Mechanics (John Wiley & Sons, New York, 1987).

23. D. C. Sinclair and A. R. West, Impedance and modulus spectroscopy of semiconducting $BaTiO_3$ showing positive temperature coefficient of resistance, J. Appl. Phys. 66,3850 (1989).

24. D.C. Sinclair, T. B. Adams, F. D. Morrison, and A. R. West, $CaCu_3Ti_4O_{12}$: One-step internal barrier layer capacitor, Appl. Phys. Lett. 80, 2153 (2002).

25. W. R. Huo, Y. F. Qu, Effects of $Bi_{1/2}Na_{1/2}TiO_3$ on the Curie temperature and the PTC effects of $BaTiO_3$-based positive temperature coefficient ceramics, Sens. Actuators A 128 (2006) 265.

26. B. Li, Inorganic Dielectric Material, National Defence Industry Press, Beijing, 1980, p. 263.

27. N. Sawangwan, J. Barrel, K. Mackenzie, T. Tunaksiri, The effect of Zr content on

electrical properties of $Ba(Ti_{1-x}\ Zr_x\ O_3)$ ceramics, Appl. Phys. A 90 (2008) 723.

28. Prasun Ganguly, A. K. Jha A.K., Structural and electrical properties of $Ba_{5-x}Ca_xSmTi_3Nb_7O_{30}$ (x = 0–5) ferroelectric ceramics, J. of Alloys and Comp.495 (2010) 7-12.
29. X. Zong, Z. Yang, H. Li., M. Yuan, Effects of WO_3 addition on the structure and electrical properties of Pb_3O_4 modified PZT–PFW–PMN piezoelectric ceramics Mater. Res. Bull. 41(2006) 1447.
30. S. K. Rout, E. Sinha, S. Panigrahi, Dielectric properties and diffuse phase transition in $Ba_{1-x}Mg_xTi_{0.6}Zr_{0.4}O_3$ solid solutions, Mater. Chem. Phys. 101 (2007) 428.
31. U Weber, G Greuel, U Boettger, S Weber, D Hennings, R. Waser, Dielectric properties of Ba(Zr, Ti) O_3 - based ferroelctrics for capacitor applications, J. Am. Ceram. Soc. 2004, 84:759.
32. V M Goldschmidt, Shrifter Nofke Videnskaps-Akad. Oslo I: mat-Naturv. No. 2, 8 (1926).
33. W D Callister, D G Rethwisch, Materials Science and Engineering: An Introduction. John Wiley & Sons; 2010.
34. G Burns, Dirty displacive ferroelectrics, Phys. Rev. B 1976; 13:215.
35. M Kumar, A Garg, R Kumar, M C Bhatnagar, Structural, dielectric and ferroelectric study of $Ba_{0.9}Sr_{0.1}Zr_xTi_{1-x}O_3$ ceramics prepared by the sol–gel method, Physica B, 2008; 403: 1819.
36. N Ponpandian, A Narayanasamy, Influence of grain size and structural changes on the electrical properties of nanocrystalline zinc ferrite, J. Appl. Phys. 2002; 92:2770.
37. S A Fadnavis, A G Katpatal, Anomalous d.c. conductance in Nd^{+3}-doped ferroelectric lead germanate single crystal, Bull Mater Sci 1997; 20:1097.

38. P Ganguly, A K Jha, Enhanced characteristics of $Ba_5SmTi_3Nb_7O_{30}$ ferroelectric nanocrystalline ceramic prepared by mechanical activation process: A comparative study Mater Res Bull 2011; 46:692.

39. R K Dwivedi, D Kumar, O Prakash, Valence compensated perovskite oxide system $Ca_{1-x}La_xTi_{1-x}Cr_xO_3$ Part I Structure and dielectric behaviour, J. Mater. Sci. 36 (2001) 3641 – 3648.

40. N Nanakorn, P Jalupoom, N Vaneesorn, A. Thanaboonsombut, Dielectric and ferroelectric properties of $Ba(Zr_xTi_{1-x})O_3$ ceramics, Ceram. Int. 34 (2008) 779-782.

41. Wei Cai , Chunlin Fu, Jiacheng Gao, Huaqiang Chen, Effects of grain size on domain structure and ferroelectric properties of barium zirconate titanate ceramics, J Alloys Comp. 480 (2009) 870-873.

42. A V Bune, C Zhu, S Ducharme, L M Blinov and V M Fridkin Piezoelectric and pyroelectric properties of ferroelectric Langmuir–Blodgett polymer films, J. Appl. Phys. 85, 7869- 7873, (1999).

43. S Tsurekawa, K Ibaraki, K Kawahara and T Watanabe, The continuity of ferroelectric domains at grain boundaries in lead zirconate titanate, Scrip. Mater., 56, 577 – 580 (2007).

44. Y Chang, Z Yang, L Wei, Microstructure, Density, and Dielectric Properties of Lead-Free $(K_{0.44}Na_{0.52}Li_{0.04})(Nb_{0.96-x}Ta_xSb_{0.04})O_3$ Piezoelectric Ceramics, J. Am. Ceram. Soc. 90, 1656-1658 (2007).

45. K Ramam, M Lopez, Microstructure, dielectric and electromechanical properties of PLSZFT nanoceramics for piezoelectric applications, J. Mater. Sci. Mater. Electron., 19, 1140-1145 (2008).

46. Qing Xua, Xinliang Chen, Wen Chen, Shutao Chen, Bokhee Kim, Joonghee Lee, Synthesis, ferroelectric and piezoelectric properties of some $(Na_{0.5}Bi_{0.5})$ TiO_3 system

compositions, Mater. Letters 59, 2437 – 2441, (2005).

47. Mark P. McNeal, Sei-Joo Jang, and Robert E. Newnham, The effect of grain and particle size on the microwave properties of barium titanate ($BaTiO_3$), J. Appl. Phys. 83, 3288-3297(1998).

48. A Batagiannis, M Wiibbenhorst, J Hulliger, Piezo- and pyroelectric microscopy, Current Opinion in Solid State and Mater. Sci, 14, 107-115 (2010).

49. J Zhang, B I Lee, R W Schwartz and Z Ding, J Grain oriented crystallization, piezoelectric, and pyroelectric properties of $(Ba_xSr_{2-x})TiSi_2O_8$ glass ceramics J. Appl. Phys. 85, 8343- 8348, (1999).

50. E S Gomez, R G Ballesteros, V C Rivas, Pyroelectric properties of $Pb_{0.88}Ln_{0.08}Ti_{0.98}Mn_{0.02}O_3$ (Ln=La, Sm, Eu) ferroelectric ceramic system, Mater. Char. 50, 349-352 (2003).

Figure Captions

Fig. 1(a) shows the X-ray diffractograms of the $[Ba_{1-3x/2}\,Ho_x]\,(Zr_{0.025}Ti_{0.975})O_3$ compounds.

Fig. 1(b) shows the Reitveld refinement of the X-ray diffractograms of the specimens.

Fig.2 shows the SEM micrographs of Ho substituted specimens sintered at 1300^{o}C.

Fig.3 shows the temperature dependence of dielectric constant and dielectric loss of the studied specimens at 1 kHz, 10 kHz and 100 kHz.

Fig.4 shows the of ln $(1/\varepsilon - 1/\varepsilon_{m})$ as a function of ln $(T- T_m)$ for the different Ho content at 1 kHz, 10 kHz and 100 kHz.

Fig.5 shows the effect of the temperature on the dc electrical conductivity σ of the studied specimens.

Fig. 6 shows the hysteresis loops of the studied specimens recorded at room temperature.

Fig.7 shows the variation of piezoelectric constant (d_{33}) as a function of Ho content in the studied specimens.

Fig.8 shows the temperature variation of pyroelectric coefficient of the studied specimens.

Table Captions

Table 1 shows the values of tolerance factor, lattice parameters, volume and tetragonal strain in holmium substituted specimens.

Table 2 shows the values of diffusivity constant and activation energy in ferroelectric and paraelectric regions in holmium substituted specimens.

Table 1

Sample	a(Å)	b(Å)	c(Å)	c/a	Volume($Å^3$)	Tolerance factor
0.01	4.0278	4.0278	4.0199	0.9927	64.091	0.91062
0.02	4.0165	4.0165	3.9997	1.004954	64.504	0.906883
0.025	4.0135	4.0135	3.9997	1.000337	64.612	0.905014
0.05	3.9999	3.9999	3.9997	0.998184	64.575	0.895671

Table 2

Sample	Frequency (kHz)	γ	E_a(eV) dc conductivity	
			Ferroelectric region	Paraelectric region
x=0.01	1	1.08	0.87	0.34
	10	1.14		
	100	1.3		
x=0.02	1	0.72	1.03	0.44
	10	0.75		
	100	0.76		
x=0.025	1	1.09	1.16	0.54
	10	1.15		
	100	1.21		
x=0.05	1	1.16	1.2	0.58
	10	1.21		
	100	1.24		

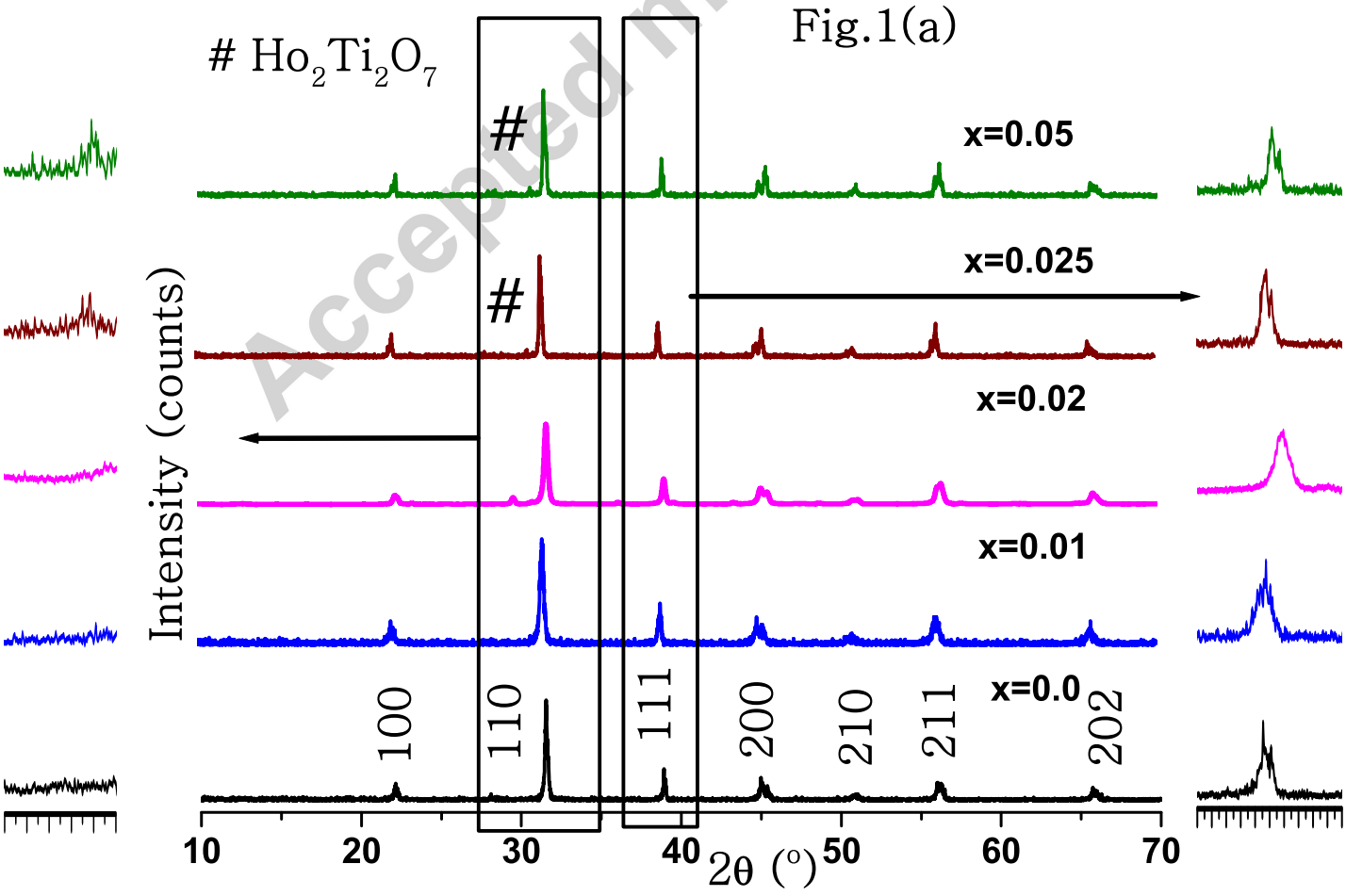

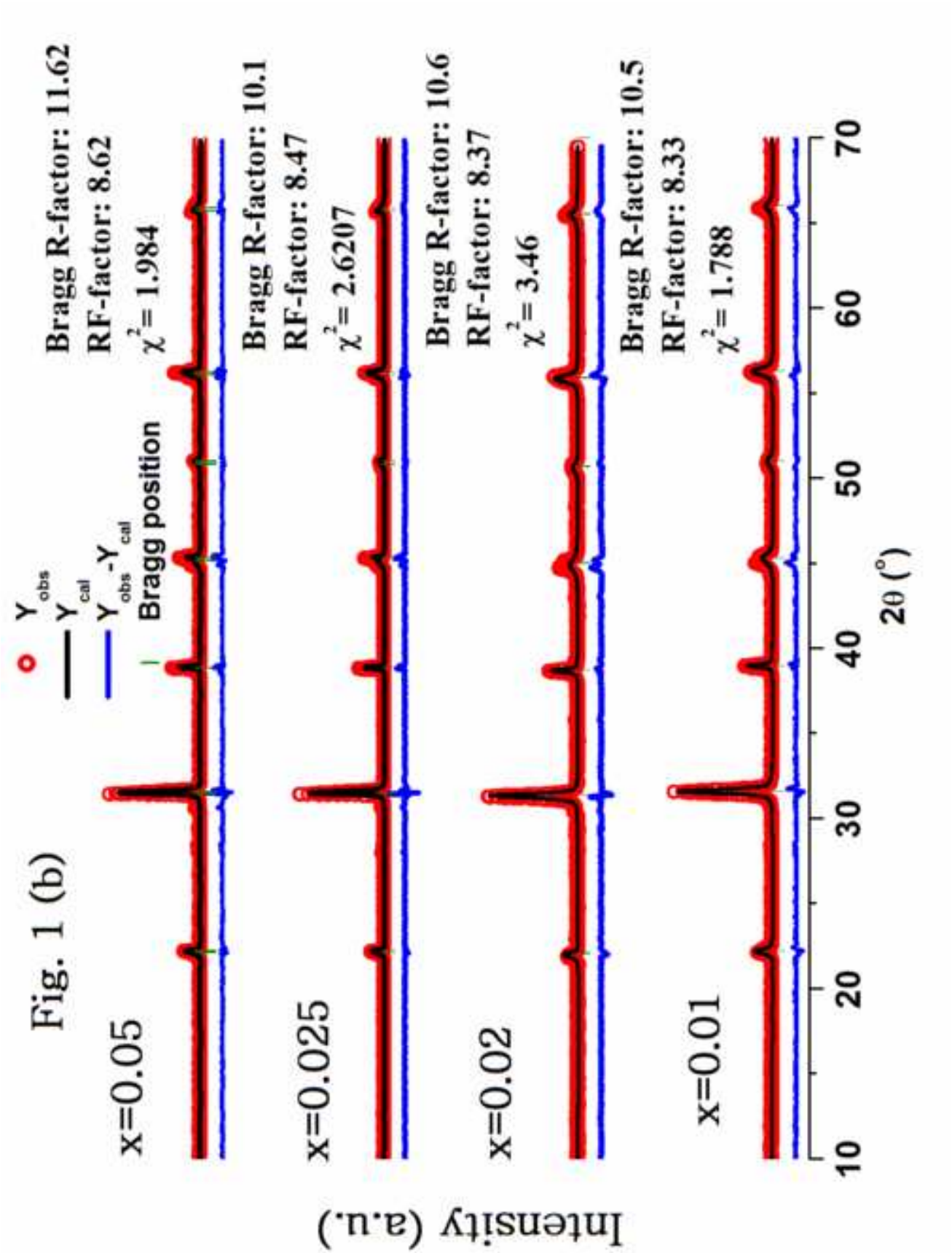

Figure

Figure

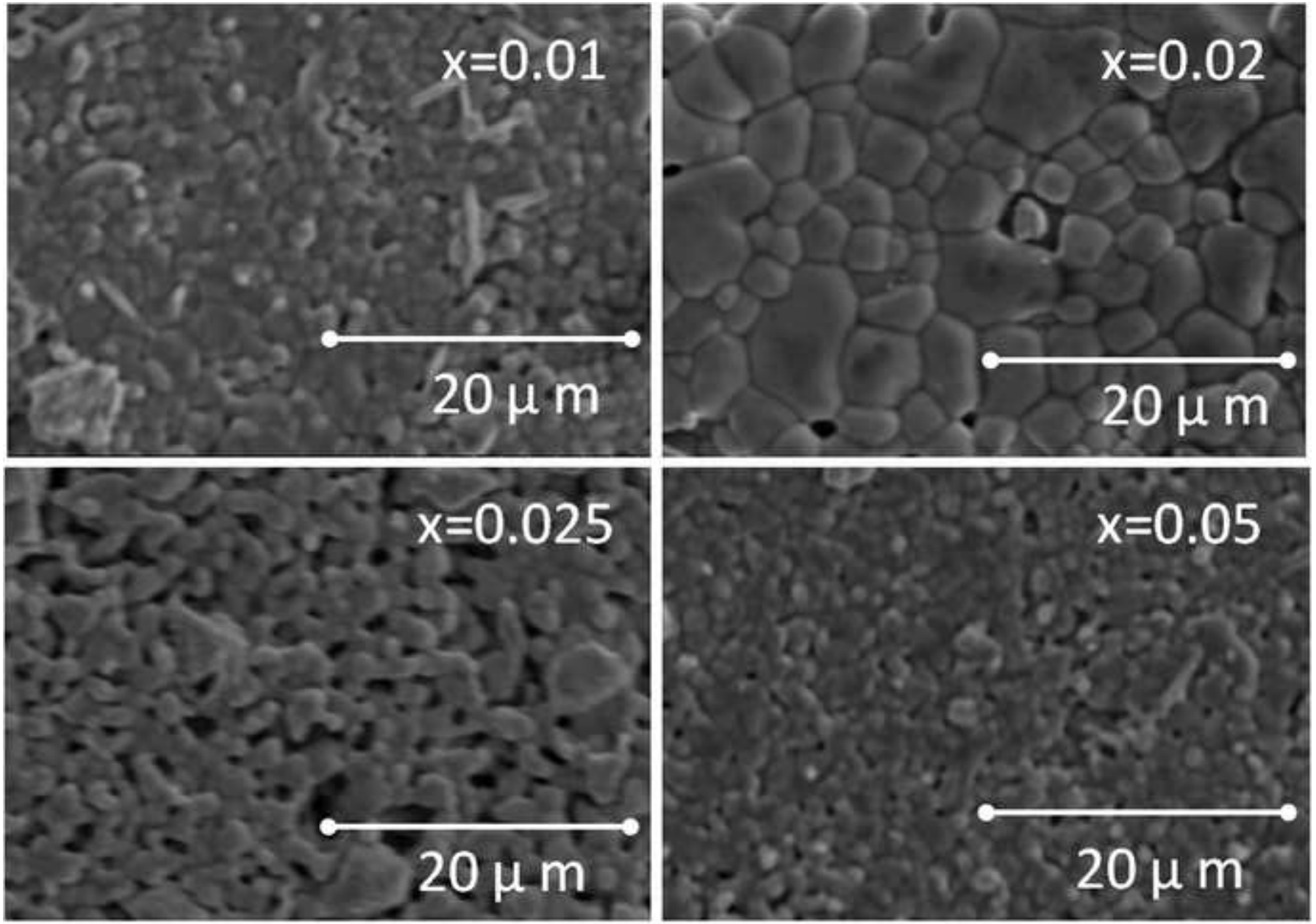

Fig.2

Fig.3

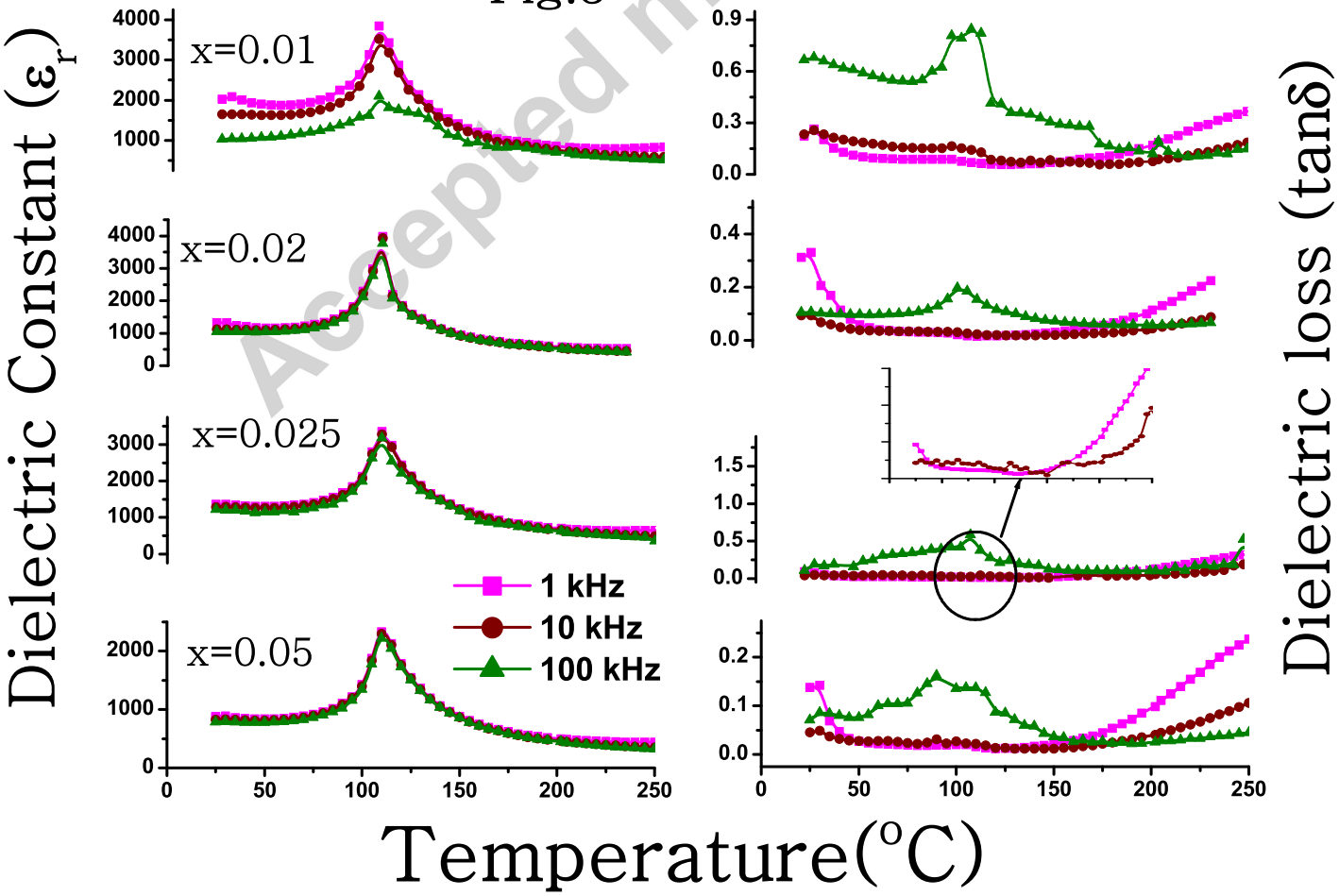

Fig.4

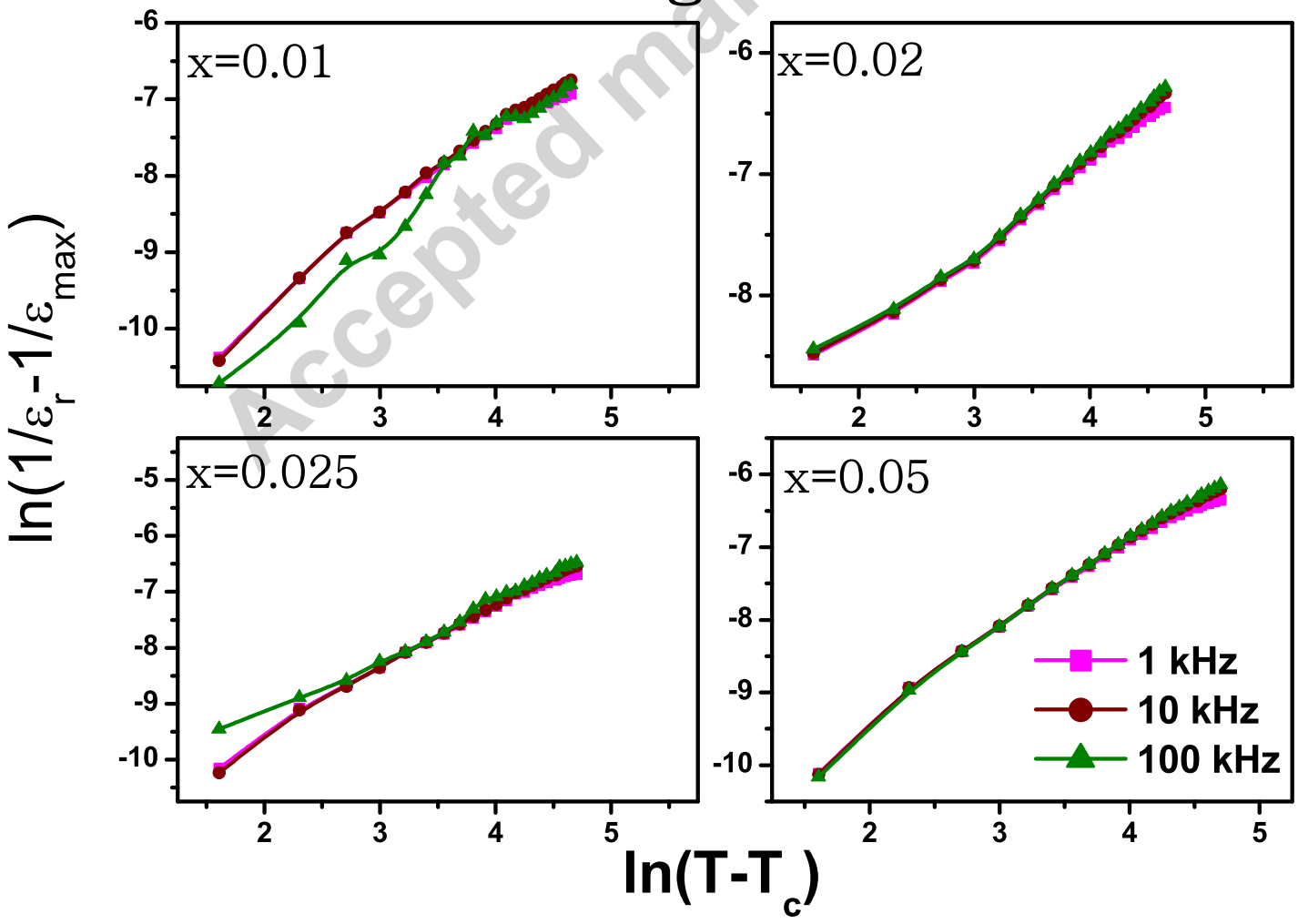

Fig.5

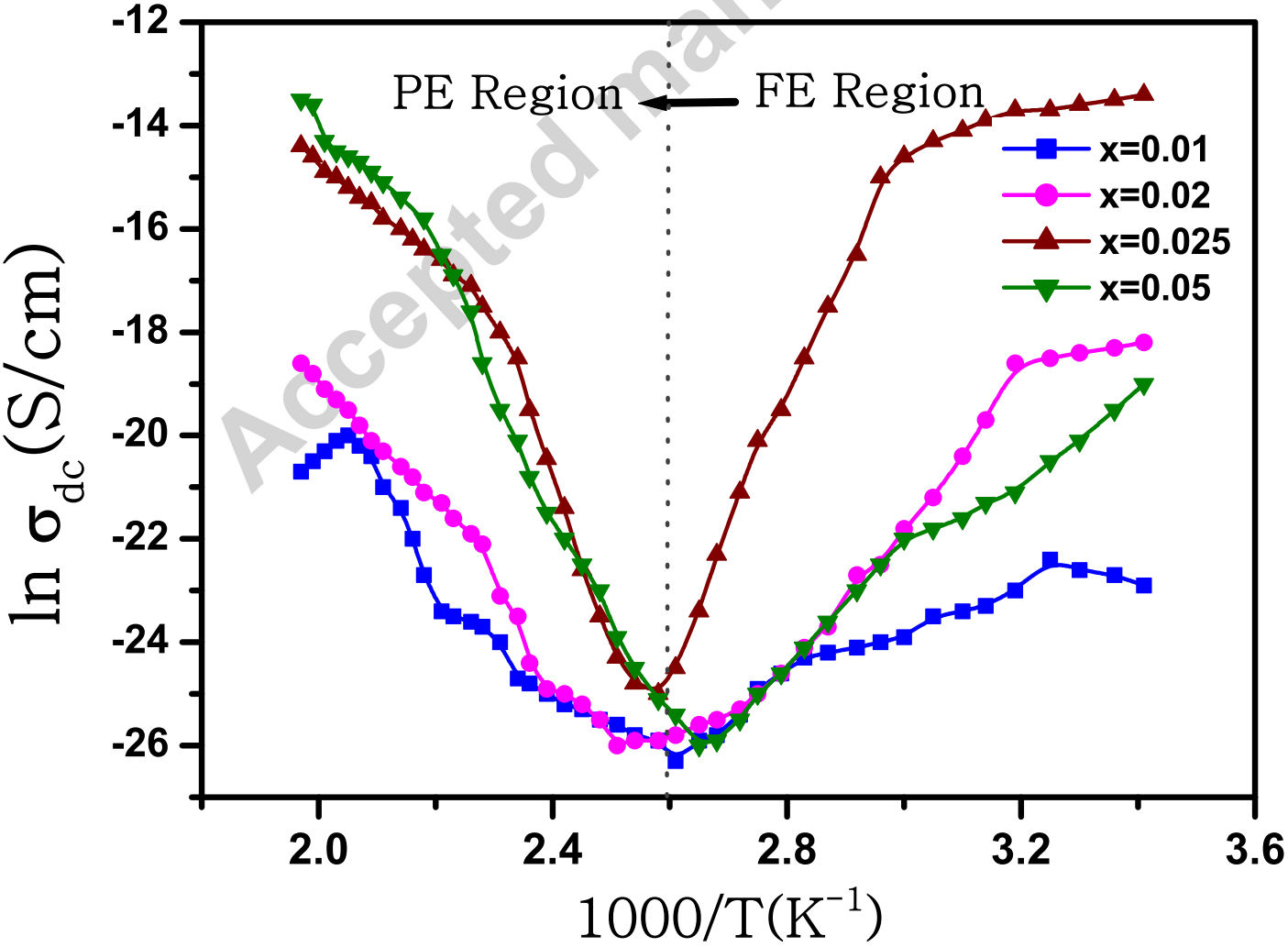

Fig.6

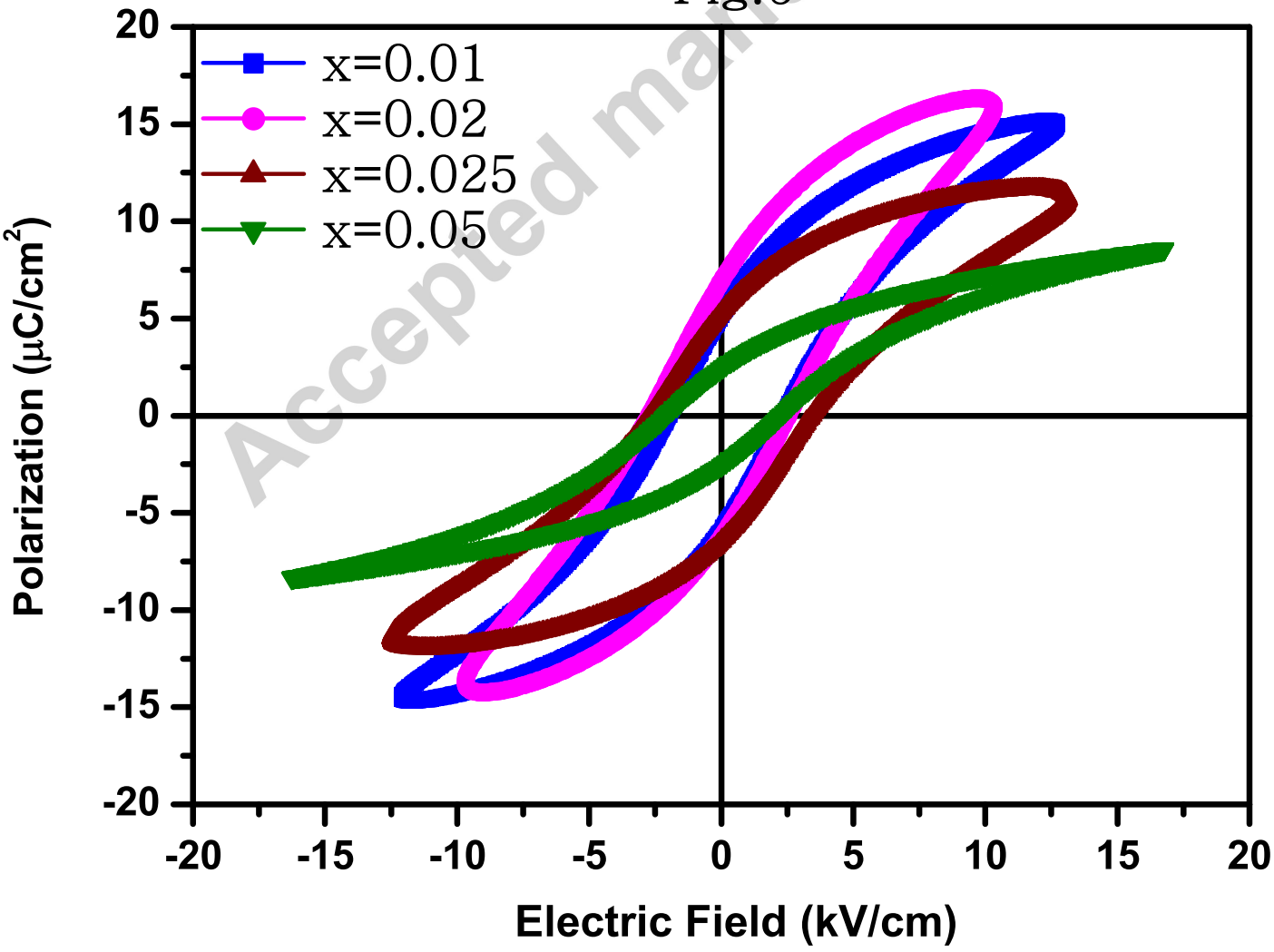

Fig.7

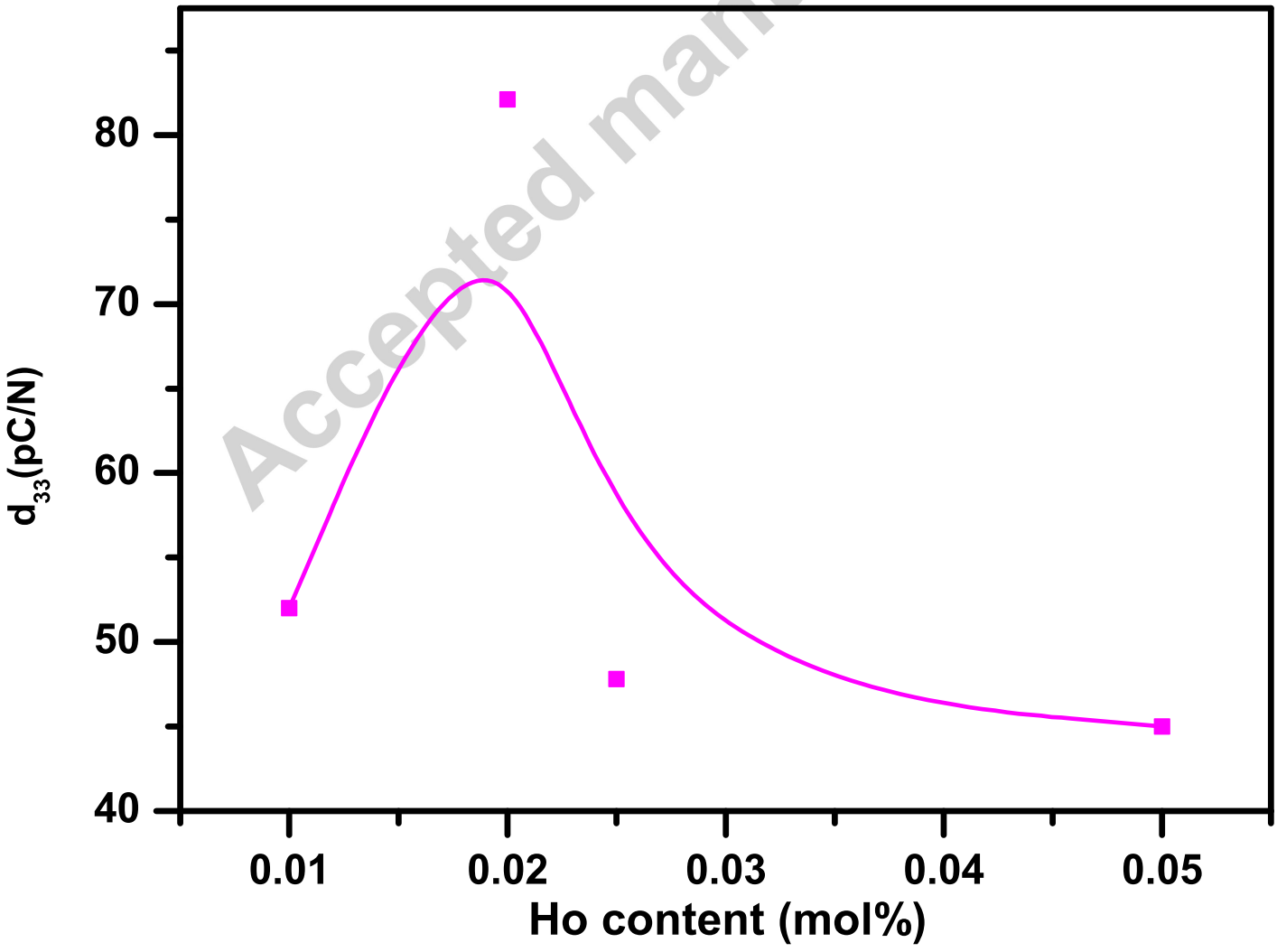

Fig.8

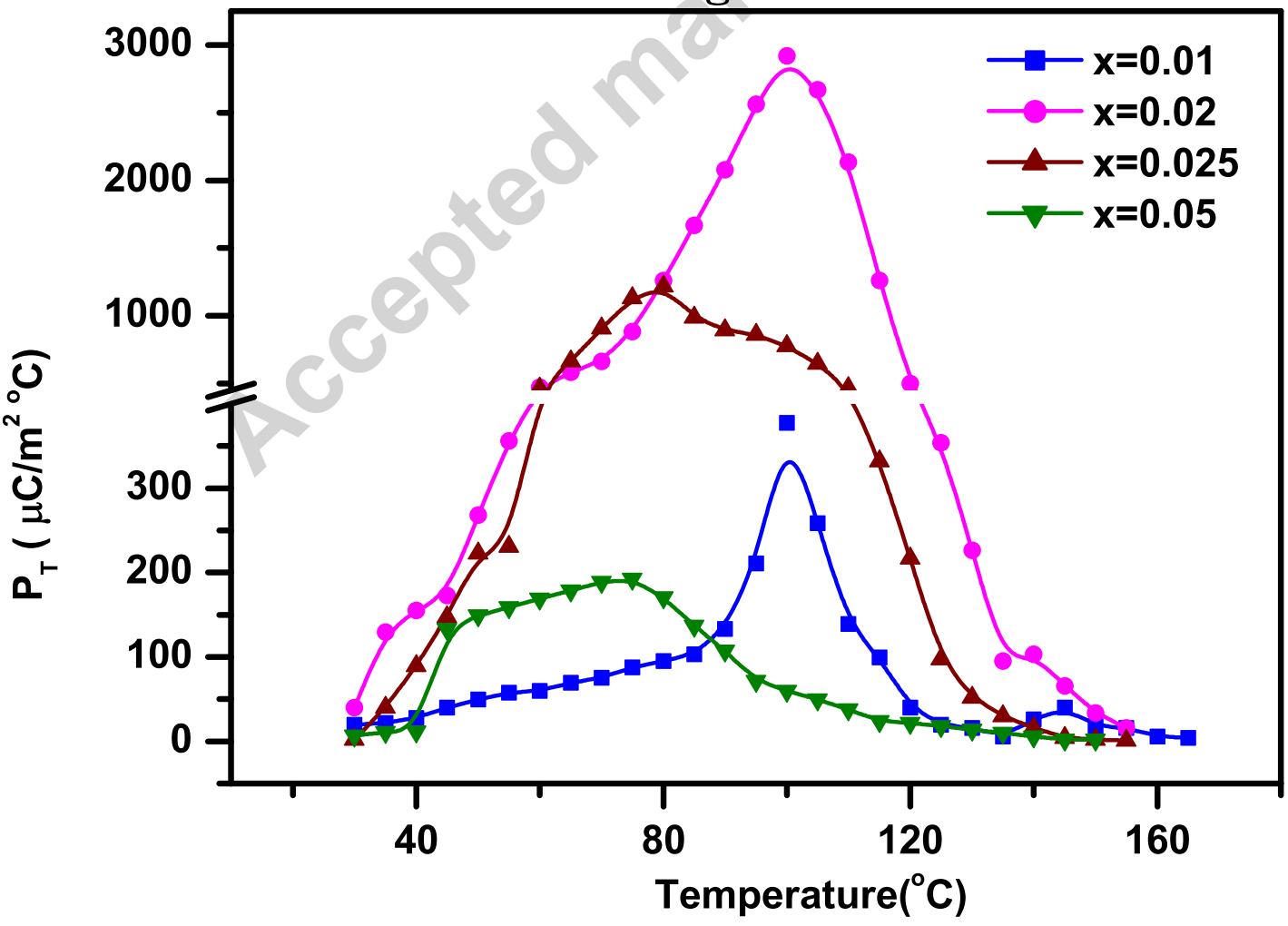

ISSN (Print) : 2320 – 3765
ISSN (Online): 2278 – 8875

International Journal of Advanced Research in Electrical, Electronics and Instrumentation Engineering

(An ISO 3297: 2007 Certified Organization)

Vol. 2, Issue 10, October 2013

Indirect Adaptive Control of Robot Manipulator and Magnetic Ball Suspension System

Bharat Bhushan

Associate Professor, Dept. of Electrical Engineering, Delhi Technological University, Delhi, India

ABSTRACT: This paper shows implementation of indirect adaptive control law for nonlinear systems using Takagi-Sugeno fuzzy system. Takagi-Sugeno fuzzy system is used to identify nonlinear system components theta alpha and theta beta. Stable Indirect Adaptive control law is such that it has two control components one is certainty equivalence control and other is sliding mode control. Sliding mode controller is used to ensure the stability of Lyapunov Function. Stability of adaptive control law is tested on two nonlinear systems Robot manipulator with the inclusion of DC motor dynamics and magnetic ball suspension system. Simulation is performed on nonlinear systems using MATLAB.

Keywords: Fuzzy System, Lyapunov Function, Adaptive Control, Robot Manipulator, DC motor dynamics, Magnetic Ball Suspension System

I. INTRODUCTION

There is extensive literature available on fuzzy logic application on nonlinear system. A mathematical way is building a fuzzy model for any nonlinear system. The fuzzy implications of the system model and the least square identification method [1] have been used to describe the nonlinear systems. Simulation can be performed using tuned fuzzy logic controllers. The fuzzy logic controller [2] displayed good stability and performance robustness characteristics for a wide range of operation. Self tuning features [3] for both the data base and the rule base can be designed using fuzzy controller. A PD controller, [4] a linear quadratic controller, a nonlinear controller are based on differential geometric notions. Adaptive tracking control architecture for a class of continuous time nonlinear systems is performed for an explicit linear parameterization of the uncertainty in the dynamics is either unknown or impossible. The architecture employs fuzzy systems, [5] which are expressed as a series expansion of basis functions, to adaptively compensate for the plant nonlinearities. The controller output [6] will be the result of applying fuzzy logic theory to manipulate the given set of control laws for nonlinear systems. The parameters of the membership functions in the fuzzy rule base [7] are changed according to some adaptive algorithm for the purpose of controlling the system state to hit a user-defined sliding surface and then slide along it. The fuzzy sliding mode controller [8] can well control most of the complex systems without known their mathematical model. The dynamics behavior of the controlled system can be approximately dominated by a fuzzified sliding surface. Fuzzy logic control and sliding mode control techniques have been integrated to develop a fuzzy sliding mode controller. A decentralized fuzzy logic controller [9] has been designed for large-scale nonlinear systems. An approximate method [10] is formulated for analyzing the performance of a broad class of linear and nonlinear systems controlled using fuzzy logic. Decision rules can be automatically [11] generated for FLC to provide a stable closed loop system using Lyapunov function. Fuzzy logic system [12] that uses adaptive sliding mode control can approximate the unknown system function of nonlinear system. A fuzzy logic controller [13] which produces desirable transient performance for nonlinear systems guarantee closed loop stability. An adaptive fuzzy control scheme [14] employs a fuzzy controller and a compensation controller for a class of nonlinear continuous systems. Stable fuzzy controllers [15] can be synthesized in terms of Mamdani model to stabilize nonlinear systems. Fuzzy logic controller [16] can control a cart balancing a flexible pole under its first mode of vibration. Adaptive fuzzy logic controller [17] uses the uniform ultimate boundedness of the closed-loop signals for a class of discrete-time nonlinear systems. The overall system stability [18] for each rule governing the control of the plants cannot be guaranteed when all of these rules are put together into a rule base for the fuzzy logic controller. Design of fuzzy logic controllers [19] for nonlinear systems with guaranteed closed loop stability and its application on combining controller is based on heuristic fuzzy rules. Adaptive sliding mode schemes [20] along with fuzzy approximators are used to approximate the unknown system function of nonlinear systems. A hybrid [21] fuzzy logic proportional plus conventional integral derivative controller is more effective in comparison with the conventional PID controller when

ISSN (Print) : 2320 – 3765
ISSN (Online): 2278 – 8875

International Journal of Advanced Research in Electrical, Electronics and Instrumentation Engineering

(An ISO 3297: 2007 Certified Organization)

Vol. 2, Issue 10, October 2013

the controlled object operates under uncertainty or in the presence of a disturbance. A direct adaptive [22] fuzzy logic controller can be used for tracking for a class of nonlinear dynamic systems. A nonlinear system [23] can be represented by Takagi-Sugeno fuzzy model and a fuzzy logic controller can be constructed by blending all local state feedback controllers with a sliding mode controller. A robust adaptive fuzzy controller [24] can be used for a class of nonlinear systems in the presence of dominant uncertain nonlinearities. Fuzzy logic system can be used to compensate [25] the parametric uncertainties that has the capability to approximate any nonlinear function with the compact input space. Limit cycle of a system [26] can be controlled by a fuzzy logic controller via some of the classical control techniques used to analyze nonlinear systems in the frequency domain. Adaptive control schemes [27] using fuzzy logic control can be used for robot manipulator which has the parametric uncertainties'. A model based fuzzy controller [28] can be used for a class of uncertain nonlinear systems to achieve a common observability Gramian. [29] Exact fuzzy modeling and optimal control can be used for inverted pendulum on cart. The nonlinear fuzzy PID [30] controller can be applied successfully in control systems with various nonlinearities. The uncertain nonlinear system [31] can be represented by uncertain Takagi-Sugeno fuzzy model structure. Most of real word systems [32] have dynamic features, i.e. the actual output depends on the previous values, and these are called autoregressive dynamic fuzzy system. A fuzzy variable structure controller [33] based on the principle of sliding mode variable structure control can be used both for the dynamic as well as for static control properties of the system. Adaptive fuzzy sliding mode control scheme [34] which incorporates the fuzzy logic into sliding mode control is used to approximate the equivalent control and the upper bound of uncertainty which involved the disturbance and approximation error. The control algorithm [35] of robust controller for a nonlinear system is based on sliding mode control that incorporates a fuzzy tuning technique, and it superposes equivalent control, switching control and fuzzy control. Based [36] on the Lyapunov approach, the adaptive laws and stability analysis can be used for a class of nonlinear uncertain systems. A neuro-fuzzy learning algorithm [37] has been applied to design a Takagi-Sugeno type FLC for a biped robot walking problem. This paper comprises of following sections. Section 2, the fuzzy logic control system concerned in this paper will be discussed. The proposed stability design approach using Lyapunov Function will be presented in Section 3. Section 4 presents dynamics of nonlinear systems. Section 5 presents simulation results and discussion. Conclusion is given in Section 6 followed by References.

II. TAKAGI-SUGENO FUZZY SYSTEMS

For the functional fuzzy system singleton fuzzification is used and the premise is defined the same as it is for the rule for the standard fuzzy system .The consequents of the rules are different, however instead of a linguistic term with an associated membership function, in the consequent a function $b_i = g_i(.)$ have been used that does not have an associated membership function. The argument of g_i contains the fuzzy system inputs which are used in the premise of the rule.

R denote the number of rules .For the functional fuzzy system an appropriate operation for representing the premise and defuzzification is obtained as

$$y = \frac{\sum_{i=1}^{R} b_i \mu_i(z)}{\sum_{i=1}^{R} \mu_i(z)} \quad (1)$$

Where $\mu_i(z)$is the premise membership function.

$$b_i = g_i(.) = a_{i,0} + a_{i,1}u_1 + \cdots + a_{i,n}u_n \quad (2)$$

where $a_{i,j}$ is fixed real number .The functional fuzzy system is referred to as a"Takagi-Sugeno fuzzy system"..

A Takagi-Sugeno fuzzy system is given by

$$y = F_{ts}(x, \theta) = \frac{\sum_{i=1}^{R} g_i(x)\mu_i(x)}{\sum_{i=1}^{R} \mu_i(x)} \quad (3)$$

Where $a_{i,j}$ are constants.

III. STABLE ADAPTIVE CONTROL USING LYAPUNOV STABILITY APPROACH

A. *Adaptive control*

For adaptive control aim is that reference model trajectory to be tracked be $y_m(t)$ and its derivatives are $\dot{y}_m(t),\ldots,y_m^{(d)}(t)$ such that output $y(t)$ and its derivatives $\dot{y}(t),\ldots,y^{(d)}(t)$ follow the reference trajectory.

ISSN (Print) : 2320 – 3765
ISSN (Online): 2278 – 8875

International Journal of Advanced Research in Electrical, Electronics and Instrumentation Engineering

(An ISO 3297: 2007 Certified Organization)

Vol. 2, Issue 10, October 2013

Assume that $y_m(t)$ and its derivatives $\dot{y}_m(t),\ldots,y_m^{(d)}(t)$ are bounded. For a reference input $r(t)$ and reference trajectory $y_m(t)$,

$$\frac{Y_m(s)}{R(s)} = \frac{q(s)}{p(s)} = \frac{q_0}{s^d + p_{d-1}s^{d-1} + \cdots + p_0} \tag{4}$$

For $r(t) = 0, t \geq 0,\ y(t) \to 0$ as $t \to \infty$.
Hence choose $y_m(t) = \dot{y}_m(t) = \cdots = y_m^{(d)}(t) = 0.$ (5)
Figure 1 shows the block diagram for indirect adaptive control.

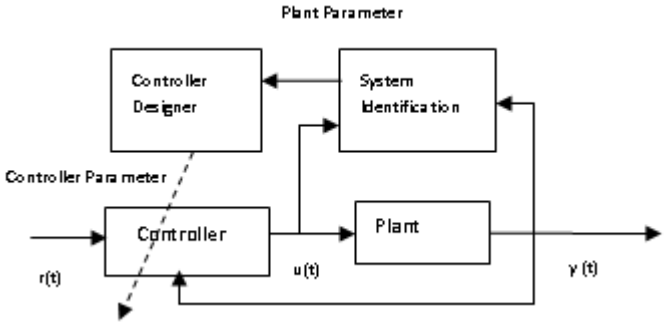

Fig.1 Indirect Adaptive Control using Takagi-Sugeno Fuzzy System

B. Online Approximator

Consider the plant

$$\dot{x} = f(x) + g(x)u \tag{6}$$
$$y(k+d) = \alpha\big(x(k)\big) + \beta\big(x(k)\big)u(k) \tag{7}$$
$$y^{(d)} = \big(\alpha_k(t) + \alpha(x)\big) + (\beta_k(t) + \beta(x))u \tag{8}$$

Here d is the order of the plant. $y^{(d)}$ denotes the d- th derivative of y. $\alpha_k(t)$ and $\beta_k(t)$ are the known components of the plant dynamics, $\alpha(x)$ and $\beta(x)$ represent the nonlinear dynamics of the plant that are unknown. $\alpha(x)$ and $\beta(x)$ are approximated with ${\theta_\alpha}^T\phi_\alpha(x)$ and ${\theta_\beta}^T\phi_\beta(x)$ by adjusting the θ_α and θ_β.
The approximations of $\alpha(x)$ and $\beta(x)$ of the actual system are

$$\hat{\alpha}(x) = {\theta_\alpha}^T(t)\phi_\alpha(x) \tag{9}$$
$$\hat{\beta}(x) = {\theta_\beta}^T(t)\phi_\beta(x) \tag{10}$$

where the vectors $\theta_\alpha(t)$ and θ_β are updated online.
The parameter errors are

$$\widetilde{\theta_\alpha}(t) = \theta_\alpha(t) - \theta_\alpha^* \tag{11}$$
$$\widetilde{\theta_\beta}(t) = \theta_\beta(t) - \theta_\beta^* \tag{12}$$

The adaptive control law $u = u_{eq} + u_{sm}$ (13)
where u_{eq} is the certainty equivalence control term and u_{sm} is the sliding mode term.

C. *Certainty Equivalence control term*

The tracking error be

$$e(t) = y_m(t) - y(t) \tag{14}$$

$K = [k_0, k_1, k_2, \ldots k_{d-2}, 1]^T$ be a vector of design parameters.
The shape of the error dynamics is controlled by the choice of k_0. The equivalence control term can be defined as

$$u_{eq} = \frac{1}{\beta_k(t) + \hat{\beta}(x)}\big(-\big(\alpha_k(t) + \hat{\alpha}(x)\big) + z(t)\big) \tag{15}$$

$\gamma > 0$ is a design parameter.

ISSN (Print) : 2320 – 3765
ISSN (Online): 2278 – 8875

International Journal of Advanced Research in Electrical, Electronics and Instrumentation Engineering

(An ISO 3297: 2007 Certified Organization)

Vol. 2, Issue 10, October 2013

D. Parameter update laws

Consider following Lyapunov function:

$$L_i = \frac{1}{2}e_s^2 + \frac{1}{2\xi_\alpha}\tilde{\theta}_\alpha^T\tilde{\theta}_\alpha + \frac{1}{2\xi_\beta}\tilde{\theta}_\beta^T\tilde{\theta}_\beta \quad (16)$$

Where ξ_α and ξ_β are design parameters.

$$\dot{L}_i = e_s\dot{e}_s + \frac{1}{\xi_\alpha}\tilde{\theta}_\alpha^T\dot{\tilde{\theta}}_\alpha + \frac{1}{\xi_\beta}\tilde{\theta}_\beta^T\dot{\tilde{\theta}}_\beta \quad (17)$$

$$\dot{\theta_\alpha}(t) = -\xi_\alpha\phi_\alpha(x)e_s \quad (18)$$

$$\dot{\theta_\beta}(t) = -\xi_\beta\phi_\beta(x)e_s u_{eq} \quad (19)$$

$\xi_\alpha > 0$ and ξ_β are adaptation gains.

Assume ideal parameters are constant. $\dot{\tilde{\theta}}_\alpha = \dot{\theta}_\alpha$ and $\dot{\tilde{\theta}}_\beta = \dot{\theta}_\beta$.

$$L_\iota = -\gamma e_s^2 - \left(f_\alpha(x) + f_\beta(x)\dot{u_{eq}}\right)e_s - \left(\beta_k(t) + \beta(x)\right)u_{sm}e_s \quad (20)$$

E. Sliding mode control term

Assume

$$u_{sm} = \frac{(F_\alpha(x)+F_\beta(x)|u_{eq}|)}{\beta_0}sgn(e_s) \quad (21)$$

So $\dot{L}_\iota \leq -\gamma e_s^2$

Since $\gamma e_s^2 \geq 0$ this shows that L_i, which is a measure of the tracking error and parameter estimation error, is a non-increasing function of time.

IV. DYNAMICS OF NONLINEAR SYSTEMS

A. Robot Manipulator Dynamics

Schematic diagram of robot manipulator with permanent magnet brush DC motor is shown in figure 2. The mechanical system dynamics for a single-link direct-drive manipulator actuated by a permanent magnet dc motor are assumed to be of the form

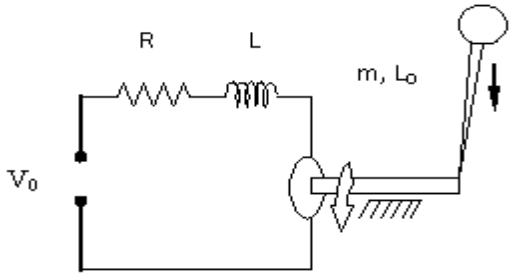

Fig.2 Robot Manipulator with Permanent Magnet Brush DC Motor

$$M\ddot{q} + B\dot{q} + N\sin(q) = I \quad (22)$$

$$M = \frac{J}{K_\tau} + \frac{mL_0^2}{3K_\tau} + \frac{M_0L_0^2}{K_\tau} + \frac{2M_0R_0^2}{5K_\tau} \quad (23)$$

$$N = \frac{mL_0G}{2K_\tau} + \frac{M_0L_0G}{K_\tau},\ B = \frac{B_0}{K_\tau} \quad (24)$$

where J is rotor inertia ,m is the link mass , $M_0$is the load mass , $L_0$is the link length , R_0 is the radius of the load, G is the gravity coefficient , B_0 is the coefficient of viscous of friction at the joint , $q(t)$is the angular motor position (and hence the position of load) , $I(t)$is the motor armature current and $K_\tau$is the coefficient which characterizes the

ISSN (Print) : 2320 – 3765
ISSN (Online): 2278 – 8875

International Journal of Advanced Research in Electrical, Electronics and Instrumentation Engineering

(An ISO 3297: 2007 Certified Organization)

Vol. 2, Issue 10, October 2013

electromechanical conversion of armature current to torque. The electrical subsystem dynamics for the permanent magnet brush dc motor assumed to be

$$L\dot{I} = V_e - RI - K_B\dot{q} \quad (25)$$

Where L is the armature inductance, R is the armature resistance, K_B is the back –emf coefficient and V_e is the input control voltage.

B. Magnetic Ball Suspension System

The magnetic ball suspension system is given by

$$\frac{dx_1(t)}{dt} = x_2(t) \quad (26)$$

$$\frac{dx_2(t)}{dt} = g - \frac{x_{3(t)}^2}{Mx_1(t)} \quad (27)$$

$$\frac{dx_3(t)}{dt} = -\frac{R}{L}x_3(t) + \frac{1}{L}\text{v(t)} \quad (28)$$

Where M=0.1Kg is the mass of the ball, g=9.81 m/s^2 is the gravitational acceleration, R=50 Ω is the resistance of winding, L=0.5 H is the winding inductance, v(t) is the input voltage and i(t) is the winding current.

V. RESULTS AND DISCUSSION

A. Indirect adaptive control of Robotic Manipulator

Universe of discourse for membership function has been taken from -0.3 to 0.3 and total nine rules have been used.

1) *For desired position [1.9 0.02 0.0]*

The nonlinear unknown components which affects the dynamics of the robotic manipulator are identified using Takagi-Sugeno Fuzzy System. The indirect adaptive control technique has been used to identify nonlinear components θ_α and θ_β . The simulation of robotic manipulator for system conditions described in Table 1 has been performed in MATLAB.

Table 1 Tuned Design Parameters for Robot Manipulator

Desired position	Initial Position	K0	K1	γ	ξ_α	ξ_β
[1.9 0.02 0.0]	[0.6 0.01 0.0]	100	20	2	4	4
[0.9 -0.02 0.0]	[0.4 -0.01 0.0]	98	19.9	4	2	2

The response of robotic manipulator with indirect adaptive control and identified nonlinear components is demonstrated for initial position [0.6 0.01 0.0] and desired position [1.9 0.02 0.0] in figures 3. It is observed that with identified nonlinear dynamics based on Takgi Sugeno based adaptive control the system tracks the desired angular position accurately with rise time of 0.4 sec The system is able to reduce the tracking error in steady state.

ISSN (Print) : 2320 – 3765
ISSN (Online): 2278 – 8875

International Journal of Advanced Research in Electrical, Electronics and Instrumentation Engineering

(An ISO 3297: 2007 Certified Organization)

Vol. 2, Issue 10, October 2013

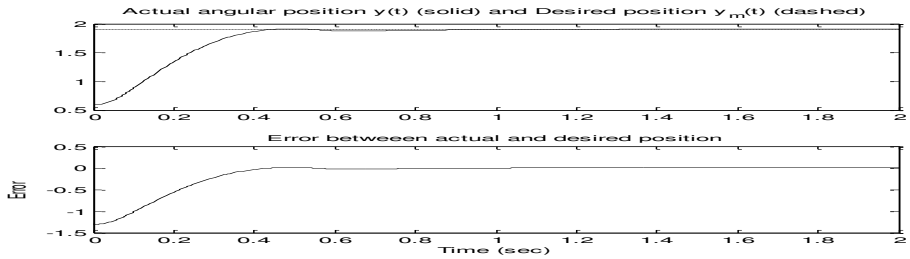

Fig.3 Variation of desired, actual angular position and their error magnitude for robotic manipulator.

2) *For desired position [0.9 -0.02 0.0]*

The developed adaptive control algorithm is also tested for different initial and desired angular position of manipulator and it is found that algorithm effectively controls the dynamics of the system under variation in initial condition and other system parameters. The dynamical behaviour of response of robotic manipulator during its transition from initial position [0.4 -0.01 0.0] and desired position [0.9 -0.02 0.0] is also shown in the figures 4.

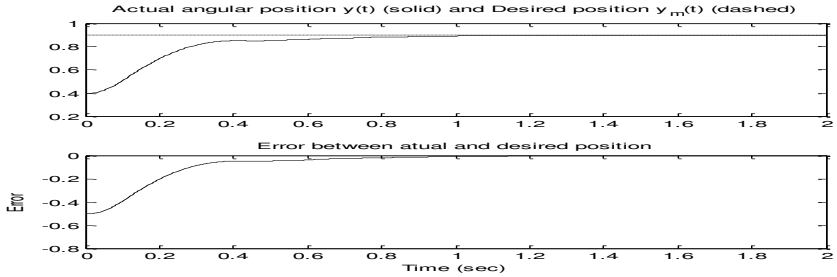

Fig .4 Variation of desired, actual angular position and their error magnitude for robotic manipulator.

B. Indirect adaptive control of Magnetic Ball Suspension System

The nonlinear unknown components which affects the dynamics of the magnetic ball suspension system are identified using Takagi-Sugeno Fuzzy System. The simulation of magnetic ball suspension system for system conditions described in Table 2 has been performed in MATLAB.

Table 2 Tuned Design Parameters for Magnetic Ball Suspension System

Desired position	Initial Position	K0	K1	γ	ξ_α	ξ_β
[1.9 0.02 0.0]	[0.6 0.01 0.0]	13	7.2	4	4	4
[0.9 0.02 0.0]	[0.4 0.01 0.0]	18	9	4	4	4

1) For desired position [0.6 0.01 0.0]

The response of magnetic ball suspension system with indirect adaptive control and identified nonlinear components is demonstrated for initial position [1.9 0.02 0.0] and desired position [0.6 0.01 0.0] in figures 5 . It is observed that with identified nonlinear dynamics based on Takgi Sugeno based adaptive control the system tracks the desired angular position accurately. The system is able to reduce the tracking error in steady state.

ISSN (Print) : 2320 – 3765
ISSN (Online): 2278 – 8875

International Journal of Advanced Research in Electrical, Electronics and Instrumentation Engineering

(An ISO 3297: 2007 Certified Organization)

Vol. 2, Issue 10, October 2013

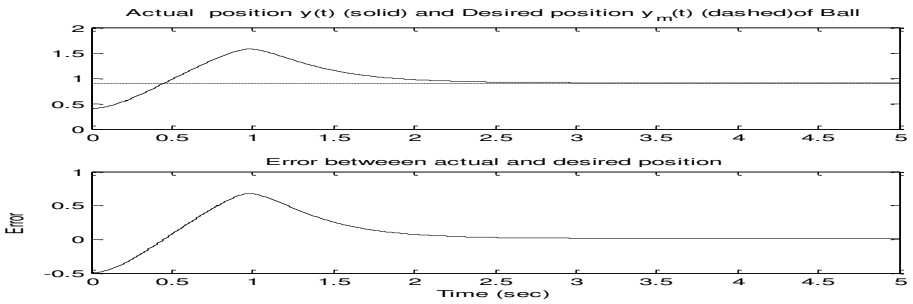

Fig .5 Variation of desired, actual angular position and their error magnitude for magnetic ball suspension system.

2) For desired position [0.4 0.01 0.0]

The developed adaptive control algorithm is also tested for different initial and desired position of ball and it is found that algorithm effectively controls the dynamics of the system under variation in initial condition and other system parameters. The dynamical behavior of response of magnetic ball suspension system during its transition from initial position [0.9 0.02 0.0] and desired position [0.4 0.01 0.0] is also shown in the figures 6.

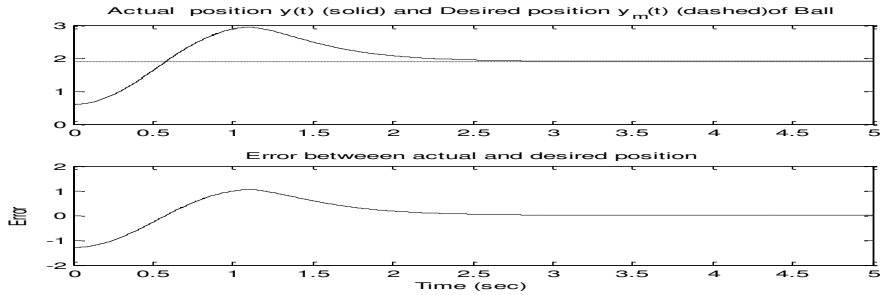

Fig .6 Variations of desired, actual angular position and their error magnitude for magnetic ball suspension system

VI. CONCLUSIONS

An indirect adaptive control law is developed using Takagi-Sugeno Fuzzy System and stability of the system is investigated using Lyapunov Stability Criterion. The necessary adaptive gains and controller parameters are determined for desired operation of system under test. Nonlinear components of the systems which affect the performance of controller are identified and used to improve the system performance. Two different classes of nonlinear systems are considered for implementation of developed adaptive control law and effectiveness of the controller under different operating conditions of the system are demonstrated. The nonlinear systems considered in the present study are Robot Manipulator with DC motor dynamics and Magnetic Ball Suspension System. Identification and Control of the systems under study were performed using Takagi-Sugeno Fuzzy system with different nine rules. It has been observed that Robot manipulator and Magnetic Ball Suspension System tracks the desired position with good accuracy in the entire range of its operation. Error between actual and desired positions is presented under different operating conditions. This confirms the stability of proposed indirect adaptive control law.

REFERENCES

[1]. C.T. Ayday and I. Eksin, "Fuzzy Identification of Nonlinear Systems," Proc. Of IEEE Int. Conf., pp. 289-292, 1993.
[2]. P. Ramaswamy, M. Riese, R. M. Edwards and K. Y. Lee, "Two Approaches For Automating the Tuning Process of Fuzzy Logic Controllers," Proc. Of IEEE Int. Conf. on Decision and Control, pp. 1753-1758, 1993.
[3]. C. Y. Shieh and S. S. Nair, "A New Self Tuning Fuzzy Controller Design and Experiments," Proc. Of IEEE Int. Conf., pp. 309-314, 1993.
[4]. D. J. Pack, M. Meng and A. C. Kak, "Comparative Study of Motion Control Methods for a Nonlinear System," Proc. Of IEEE Int. Conf. pp. 1413-1418, 1993.

ISSN (Print) : 2320 – 3765
ISSN (Online): 2278 – 8875

International Journal of Advanced Research in Electrical, Electronics and Instrumentation Engineering

(An ISO 3297: 2007 Certified Organization)

Vol. 2, Issue 10, October 2013

[5]. C. Y. Su and Y. Stepanenko, "Adaptive Control of A Class of Nonlinear Systems with Fuzzy Logic," Proc. Of IEEE Int. Conf., pp. 779-785, 1994
[6]. C. K. Chak and G. Feng, "Nonlinear System Control with Fuzzy Logic Design," Proc. Of IEEE Int. Conf., pp. 1592-1596, 1994.
[7]. S. C. Lin and Y. Y. Chen, "Design of Adaptive Fuzzy Sliding Mode for Nonlinear System Control," Proc. Of IEEE Int. Conf., pp. 35-39, 1994.
[8]. C. C. Kung and C. C. Liao, "Fuzzy-Sliding Mode Controller Design for Tracking Control of Nonlinear System," Proc. Of American Control Conference, pp.180-184, June 1994.
[9]. Z. M. Yeh, "A Decentralized Fuzzy Logic Controller Design," Proc. Of IEEE Int. Conf., pp. 602-607, 1994.
[10]. S. S. Farinwata, "Robust Stability of Fuzzy Logic Control Systems," Proc. Of American Control Conference, pp. 2267-2271, June 1995.
[11]. C.Y. Tsai and T. H. S. Li, "Design of Lyapunov Based Fuzzy Logic Controller," Proc. Of IEEE Int. Conf., pp. 396-401, 1996.
[12]. S. Jeoung, J. Han, K. Im and W. Ham, "Adaptive Fuzzy Sliding Mode Control of Nonlinear System: The Second Control Scheme," Proc. Of IEEE Int. Conf., pp. 269-274, 1996.
[13]. F. H. F. Leung, L. K. Wong and P. K. S. Tam, "Fuzzy model based controller for an inverted pendulum," Electronic Letters, vol. 32, no. 18, pp. 1683-1685, 1996.
[14]. Y. Tang, N. Zhang and Y. Li, "Stable Fuzzy Logic Control of a Class of Nonlinear Systems," Proc. Of IEEE Int. Conf. , pp. 361-365, 1996.
[15]. S. Lei and R. Langari, " An approach to Synthesis and Approximation of Stable Fuzzy Logic Controllers," Proc. Of IEEE Int. Conf., pp. 1446-1452, 1996.
[16]. E. P. Dadios and D.J. Williams, "Multiple Fuzzy Logic Systems: A Controller for the Flexible Pole-Cart Balancing Problem," Proc. Of IEEE Int. Conf. on Robotics and Automation, pp. 2276-2281, 1996.
[17]. S. Jagannathan, "Adaptive Fuzzy Logic Control of Feedback Linearizable Discrete-Time Nonlinear Systems," Proc. Of IEEE Int. Conf., pp. 133-138, 1996.
[18]. L. K. Wong, F.H.F. Leung and P. K. S. Tam, "Lyapunov function Based Design of Heuristic Fuzzy Logic Controllers," Proc. Of IEEE Int. Conf., pp. 281-285, 1997.
[19]. L.K. Wong, F.H.F Leung and P. K. S. Tam, " Lyapunov Function Based Design of Fuzzy Logic Controllers and its Application on Combining Controllers," IEEE Trans. On Industrial Electronics, vol. 45, no. 3, pp. 502-509, June 1998.
[20]. B. Yoo and W. Ham, " Adaptive Fuzzy Sliding Mode Control of Nonlinear System," IEEE Trans. On Fuzzy Systems, vol. 6, no. 2, pp. 315-321, May 1998.
[21]. W. Li, "Design of a Hybrid Fuzzy Logic Proportional Plus conventional Integral-Derivative Controller," IEEE Transaction on Fuzzy Systems, vol. 6, no. 4, pp. 449-463, Nov. 1998.
[22]. P. Y. Guo, Z. H. Guang and Z. Bien, "Design of fuzzy direct adaptive controller and stability analysis for a class of nonlinear system," Proc. Of the American Control Conferences, pp. 2274-2279, 1998.
[23]. W. Chang, Y. H. Joo, J. B. Park and G. Chen, "Robust Fuzzy Model Based Controller for Uncertain Systems," Proc. Of IEEE Int. Fuzzy Systems Conf., pp. 486-491, 1999.
[24]. H. Han and C. Y. Su, "Further Results on Adaptive Control of a Class of Nonlinear Systems with Fuzzy Logic," Proc. Of IEEE Int. Fuzzy Systems Conf. , pp. 1309-1314, 1999.
[25]. B. K. Yoo and W. C. Ham, "Adaptive Control of Robot Manipulators using Fuzzy Compensator, Part-II," Proc. Of the IEEE Int. Conf. on Intelligent Robots and Systems," pp. 52-57, 1999.
[26]. E. Kim, H. Lee and M. Park, "Limit Cycle Prediction of a Fuzzy Control System Based on Describing Function Method," IEEE Transactions on Fuzzy Systems, vol. 8, no. 1, pp. 11-22, Feb. 2000.
[27]. B. K. Yoo and W. C. Ham , "Adaptive Control of Robot Manipulator using Fuzzy Compensator," IEEE Transaction on Fuzzy Systems, vol. 8, no. 2, pp. 186-199, April 2000.
[28]. W.J. Chang, "Model Based Fuzzy Controller Design with Common Observability Gramian Assignment," Journal of Dynamic Systems, Measurement and Control, vol. 123, pp. 113-116, March 2001.
[29]. P.P. Mohanlal and M.R. Kaimal, "Exact Fuzzy Modeling and Optimal Control of the Inverted Pendulum on Cart," Proc. Of the IEEE Conf. on Decision and Control, pp. 3255-3260, 2002.
[30]. M. Petrov, I. Ganchev and A. Taneva, "Fuzzy PID Control of Nonlinear Plants," Proc. Of IEEE Int. Symposium, pp.30-35, 2000.
[31]. W. Chang, J. B. Park, Y. H. Joo and G. Chen, "Output Feedback Fuzzy Control for Uncertain Nonlinear Systems," Journal of Dynamic Systems, Measurement and Control, vol. 125, pp. 521-530, 2003.
[32]. Z. Vicek, "Analysis of Autoregressive Fuzzy Systems," Proc. Of IEEE Int. Conf., pp. 1233-1238, 2004..
[33]. Y. H. Cheng, X. S. Wang and J. Q. Yi, "Fuzzy Variable Structure Control For Trajectory Tracking of Two Link Flexible Manipulators," Proc. Of IEEE Int. Conf. on Machine Learning and Cybernetics, pp. 711-714, 2003.
[34]. J. Yu, W. Gu and Y. Zhang, "New Adaptive Fuzzy Sliding Mode Control System for SISO Nonlinear System," Proc. Of the 5th World Congress on Intelligent Control and Automation, pp. 1196-1199, 2004.
[35]. Z. Chen, C. Shan and H. Zhu, "Adaptive Fuzzy Sliding Mode Control Algorithm for a Non-Affine Nonlinear System," IEEE Transactions on Industrial Informatics, vol. 3, no. 4, pp. 302-311, 2007.
[36]. C. H. Lee, B.R. Chung, F. K. Chang and S. K. Chang, "Adaptive Back stepping Control for a Class of Nonlinear Uncertain Systems Using Fuzzy Neural Networks," Proc. Of IEEE Int. Conf. on Machine Learning and Cybernetics, pp. 431-436, 2007.
[37]. S. L. C. Maciel, O. Castillo, L. T. Aguilar and J. R. Castro, " A T-S Fuzzy Logic Controller for Biped Robot Walking based on Adaptive Network Fuzzy Inference System," Proc of Int. Joint Conf on Neural Networks, pp. 1-8, 2010.

Volume 3, Issue 9, September 2013 ISSN: 2277 128X
International Journal of Advanced Research in Computer Science and Software Engineering
Research Paper
Available online at: www.ijarcsse.com

Efficient AODV using Improved flooding with Sectorized Antenna for Mobile Adhoc Networks

Rajesh Kumar Yadav
Computer Engineering
Delhi Technological University
Delhi, India

Dr. Daya Gupta
Computer Engineering
Delhi Technological University
Delhi, India

Viomesh Kumar Singh
Computer Engineering
Delhi Technological University
Delhi, India

Abstract—Mobile Adhoc Networks (MANET) is decentralized, self configuring, wireless network of mobile devices without using any infrastructure. MANET required dynamic routing to respond to the topological changes as nodes are dynamic in nature. Dynamic routing protocol such as Adhoc on demand distance vector routing (AODV) with Expanding Ring Search (ERS) is widely used technique to reduce energy consumption and broadcast cost of searching in MANET. In AODV, network-wide flooding is initiated whenever any node wants to communicate with some other node to find the route between source and destination whereas in ERS, flooding performed in successively larger area in network. In this paper, we reduce number of transmissions by each forwarding node using sectorized antenna in high density networks. The selective flooding shows expected 35% reduction in the routing overhead during route discovery when applied to various standard regular models.

Keywords— Mobile Adhoc Networks, Adhoc on Demand Distance Vector Routing, Expanding Ring Search, Directonal Antenna, Sector Antenna

I. INTRODUCTION

Mobile Ad hoc Networks (MANETs) is a collection of mobile wireless devices (nodes) that form decentralized, self organizing and infrastructure-less wireless network among them [1]. The communication between any two nodes is accomplished via forwarding of messages by other member nodes known as intermediate nodes. Nodes in MANET are with limited power, independent of each other and free to move. Due to the mobility of nodes, mulitpath propagation, path loss and interference topological changes occur in network which makes routing difficult. Dynamic routing is required to respond to the topological changes as nodes are dynamic in nature. Routing protocols in MANET are categorized as flat routing, hierarchical routing and geographic position assisted routing. According to routing strategy flat routing is further subdivided into proactive routing and reactive routing [2]. The proactive routing algorithms (e.g. FSR,OLSR) are table driven that find the routes constantly and maintain routing information for all source-destination pairs in routing table which cause high routing overhead. Reactive routing protocols such as AODV, DSR discover the route between source and destination pair only when it needed. These algorithms also known as on demand routing protocols.

Adhoc On Demand Distance Vector (AODV) routing protocol is widely used routing algorithm for MANET [3]. Whenever any source need to communicate with some other node it starts blind flooding of RREQ (Route request packet, message initiated by the source to find the destination) in whole network to find and establish unicast route between source and destination. Due to network-wide flooding, Each and every nodes of the network have to entertain the Route request packet which causes overhead in terms of wireless node processing, energy consumption and bandwidth. Overhead in bandwidth occurred when an RREQ broadcasted by source in the process of on demand route discovery. To solve this problem Expanding Ring Search (ERS) concept is applied [4]-[6]. In ERS based on AODV, flooding performed in successively larger area in network to avoid network-wide broadcast. In this paper we perform selective flooding to improve AODV and ERS routing algorithms which utilizes a sectorized antennas at each mobile wireless node. Each node is equipped with multiple identical directional antennas facing in different directions covering all 360 degrees in non-overlapping manner instead of single omnidirectional antenna. It divides omnidirectional transmission range into multiple sectors. Each node can broadcast only in selected sectors to reduce the total number of transmissions compared to broadcasting using blind flooding.

In a comparative analysis between blind flooding and selective flooding applied on AODV and ERS using three sector, four sector and eight sector antenna, considerable reduction of up to 35% in the routing overhead during route discovery is achieved. We perform this analysis based on standard eight neighbor regular 2D grid model, four neighbor regular 2D grid model, and hexagonal model and also describe their behavior in a general model.

II. OVERVIEW OF AODV AND ERS

The topologies in MANET are so unstable and dynamic in nature as it is formed by mobile nodes; So MANET required dynamic routing to respond to the topological changes. Reactive routing protocols such as Adhoc On Demand Distance Vector (AODV) Routing and Expanding Ring Search (ERS) based on AODV are most widely used reactive

routing protocol, in which routes are establish only when they are needed. At each node in the network, Route information is maintained in traditional routing tables, one entry per destination, distance information (total number of inter mediate nodes), sequence numbers to determine whether routing information is up-to-date and to prevent the routing loop. Routing entries which are not recently used are expired in AODV. AODV fallows simple blind flooding, i.e. when a node want to communicate with some other node (unknown destination), it broadcast RREQ for that destination. If receiving node (has not received RREQ before) has route to destination or itself is the destination node, it generates a RREP (Route Reply) back to the source in hope-by-hope fashion via all intermediate nodes, otherwise it simply rebroadcasts the RREQ [3]. When the source receives the RREP for desired destination, it records the path for the same and start unicasting the data. In case of multiple RREP received by the source, the route with minimum hope count is chosen.

In AODV, network-wide flooding is performed and route is established whenever needed. Each nodes of the network have to entertain the RREQ, it causes overhead in terms of energy consumption, node processing and bandwidth [7]. To overcome the network wide broadcast problem, expanding ring search (ERS) technique is applied. To discover the route to the required destination, ERS performs searching in successively larger area in network to avoid network-wide broadcast.

In ERS based on AODV, flooding of RREQ starts with small TTL (time to live) counter value for route discovery. Time-To-Live (TTL) counter is used to count the number of hops to end of the current ring. Each node decrement the TTL value by 1 before rebroadcasting RREQ. Nodes encounter RREQ with TTL zero; do not forward RREQ any further and flooding halts. Using TTL value, source node can control flooding radius. If source does not receive any RREP within the predefined time-out period, it modify old TTL value to a new value by adding some appropriate pre-decided TTL_increment (to increase the search radius) and the flooding is repeated up to new TTL. A TTL_increment variable is used to gradually increase the size of successive rings. This repetitive process is continues until TTL threshold value encounters or destination found. Whenever source receives RREP, source records the route and won't modify TTL again and flooding stops. If TTL reaches to threshold value the RREQ is broadcast throughout the entire network like AODV. Using TTL value, source node can control flooding [4]-[6].

III. SECTORIZED ANTENNA

An antenna redirects the energy it receives from the transmitter. It provides three fundamental properties direction, gain and polarization. Gain measure the amount of energy increase to a radio frequency by that antenna [8][9]. Direction measure the transmission coverage angle or radiation pattern in degrees. These angles are measured in degrees and are called beamwidths. Omnidirectional antenna provides uniform two-dimensional radiation pattern. In other words, Omnidirectional antenna has perfect 360 degree horizontal beamwidth radiation pattern. Omni antenna is used in order to increase the probability of receiving signal in a multipath environment. Omnidirectional antennas such as Cisco Aironet Antennas (HGA9N and HGA7S) are used for small office environments.

Directional antenna is used to redirect the energy in some specific direction as it decreases angle of radiation [10][11]. The coverage angle is measured in degrees and called beamwidths. Directional antenna focus reduced coverage angle but increase coverage distance in one direction. Therefore, we can transmit RF energy to farther distances in particular direction as effective beamwidh decreases. In this system, antenna should face in the direction where the coverage is desired. Sectorized antenna is made of multiple identical directional antennas radiating at equal size coverage angle in non-overlapping manner that makes a angularly-separated sector-shaped radiation pattern which divides transmission range into equal size sectors. Sectorized antenna system can be used to transmit in one or more selective sectors as well as in whole 360° omnidirectional transmission range. This configuration provides good data rates and good signal consistency within the coverage area. Sectorized antenna systems are mainly used to reduce interference. If any sectorized system built up of k directional antennas aimed in different direction then each node in this system is assigned different channels to different interfaces is assigned to reduce interface. In this paper, we are applying sectorized antenna system for efficient broadcasting to reduce routing over head by selective transmission of RREQ.

IV. SELECTIVE FLOODING IN AODV AND ERS USING SECTORIZED ANTENNA

Nodes equipped with single omnidirectional antenna is replaced with k directional antennas that equally divide the omnidirectional transmission range into k non-overlapping sectors where one or more such sectors can be switched on for selective transmission. Each antenna supports communication with multiple nodes using different channels. In this proposed scheme using sectorized antenna, each node is capable of selective transmission over multiple sectors. At each node efficient broadcasting is performed by switching on some of the sectors for transmission using directional antennas to avoid broadcast storm problem caused by blind flooding [12]. Each node can control RREQ broadcast which follows blind flooding. In this technique, routing overhead can be reduced and channel capacity can be improved by switching on some of the sectors for transmission using directional antennas while restricting the transmission in others sectors by switching them off.

In this paper, we analyze selective flooding in AODV and ERS routing protocols using sectorized antenna. In this configuration, each node is capable of selective transmission in specific direction with its neighbours. In conventional flooding mechanism, each node sends the RREQ to all its neighbours by following uniform two-dimensional radiation pattern. The improved flooding technique uses sectorized antenna to greatly reduce number of transmission links in route discovery process to reduce routing overhead. As shown in the Fig 1, Node A transmits the RREQ packet only to the sectors with black nodes, in contrary node A do not broadcast RREQ to sectors with white nodes. This mechanism provides increased efficiency by reducing redundant transmission. In this paper, the sectorized antenna of each node provides selective communication in specific direction with it's neighbours. We are using three kind of different sectorized

antenna system using 3 sector antenna, 4 sector antenna and 8 sector antenna system. In an adhoc system of mobile nodes which all consist of identical 3 sector antenna or 4 sector antenna, Nodes do not transmit RREQ to the sector from where it receive RREQ packet, whereas in 8 sector antenna configuration, the sector of the source node of RREQ and its adjacent sectors do not receive RREQ packet.

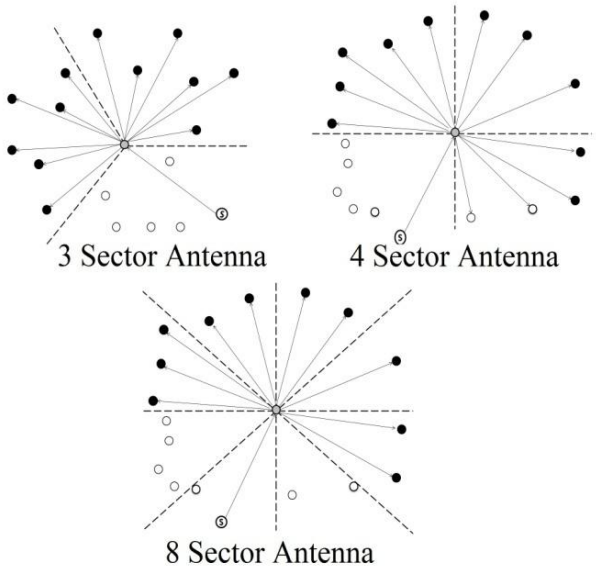

Fig. 1. Selective flooding in sectorized antenna.

V. REGULAR TOPLOGIES

We consider three regular topologies here: standard eight neighbours regular 2D grid model, standard four neighbours regular 2D grid model and hexagonal topologies. These topologies are shown in Figure 2. In regular topology [5], total nodes belonging to the rings follow a regular pattern.

There are total R rings in the topology, ring R being R hops away from the source node. For hexagonal and 2D grid(8 neighbours and 4 neighbours), nodes that are 1 hop away from the source belong to first ring, nodes that are 2 hop away from the source belong to second ring. In standard eight neighbours regular 2D grid model, standard four neighbours regular 2D grid model, each node has directly connected to 8 neighbours and 4 neighbours respectively, whereas in hexagonal topology each node has 6 neighbours.

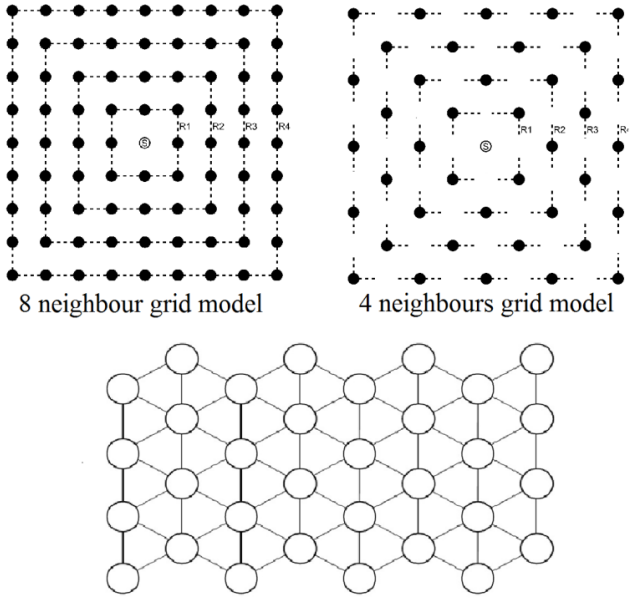

Fig. 2. The Regular Topologies

Transmission cost can include many things, such as, processing cost, network bandwidth, etc. In this paper, we consider number of RREQ messages transmitted in the network, for a particular query.

VI. ANALYSIS AND RESULT

To analyze the efficiency of route discovery cost in AODV and ERS using sectorized antenna, we compare the number of RREQ transmitted in omnidirectional antenna, three sector antenna, four sector antenna and eight sector antenna. To

theoretically analyze the performance, we use standard eight neighbor regular 2D grid model, four neighbor regular 2D grid model, and hexagonal model. The standard model provides a set of nodes with uniform density and distribution [5]. We also provide a comparative general description of ERS and EAODVSA.

Here first we analyze effect of selective flooding in AODV in terms of number of RREQ for route discovery process afterwards we analyze its effect on ERS for various standard model.

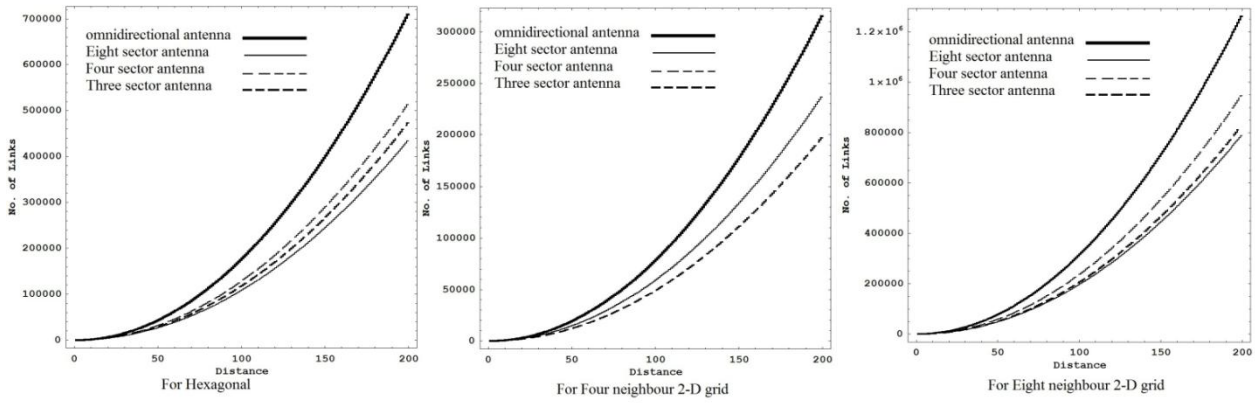

Fig. 3. No. of Links used in route discovery in AODV

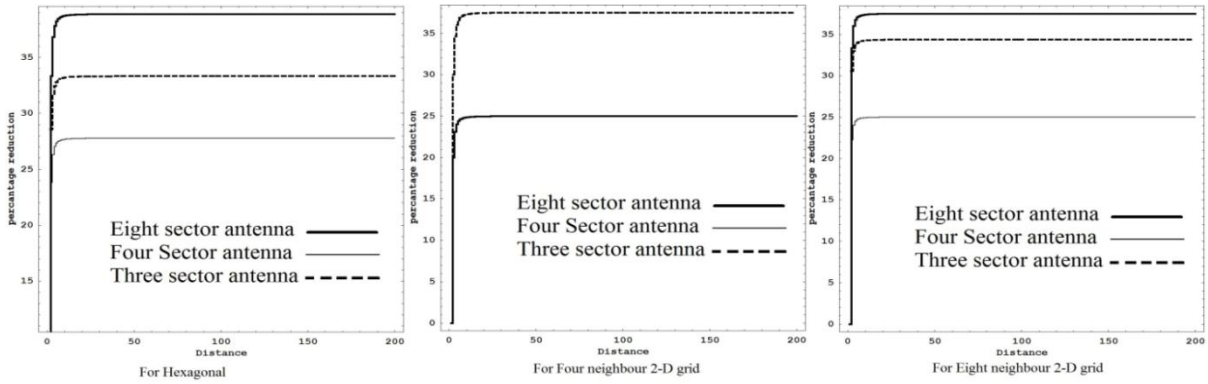

Fig. 4. Comparative reduction of routing overhead graph of selective flooding and blind flooding in AODV

Fig 4, shows the number of transmitted RREQ packet for blind flooding and selective flooding using eight sector on standard hexagonal model, four neighbor regular 2D grid model and eight neighbor regular 2D grid model. For standard hexagonal model and eight neighbor regular 2D grid model, eight sector antenna transmit least RREQ packet after that three sector antenna and four sector antenna number of links comes respectively in increasing order. But in four neighbor regular 2D grid model, three sector antenna provides best performance and eight sector antenna and four sector antenna provide near about same performance which is lesser than three sector antenna.

Fig 5, shows percentage reduction in number of transmitted link between selective flooding (using sectorized antenna) and blind flooding. For standard hexagonal model and eight neighbor regular 2D grid model, eight sector antenna provides best performance which is little more than 35% reduction in number of RREQ transmitted where as three sector antenna provides near about 33% reduction and four sector antenna around 25 % reduction in both models. In four neighbor regular 2D grid model three sector antenna provide best performance with little more than 35% reduction in number of links for route discovery whereas eight sector antenna and four sector antenna provide same reduction which is about 25%.

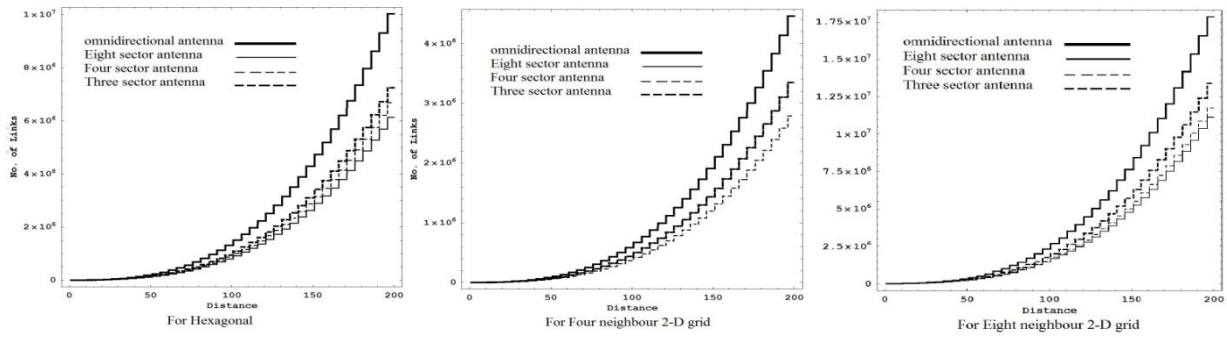

Fig. 5. No. of Links used in route discovery in ERS

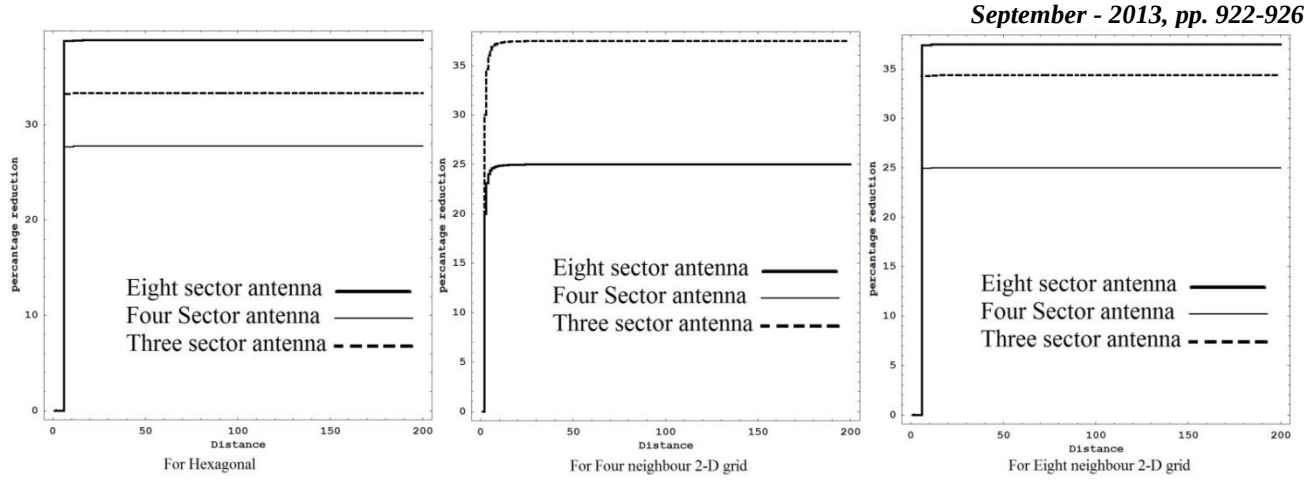

Fig. 6. Comparative reduction of routing overhead graph of selective flooding and blind flooding in ERS

When we applied selective flooding in ERS, it provides exactly the same result for the number of transmitted RREQ packet showed in Fig 5, and reduction in number of transmitted link showed in Fig 6, as we got in case of AODV because ERS is based on AODV and follows the same flooding concept.

VII. CONCLUSION

In this paper, we analyze efficient broadcasting applied on AODV and ERS routing algorithm using sectorized antenna. Sectorized antenna is able to provide selective flooding in required direction, is used to reduce redundant rebroadcast during route discovery.

REFERENCES

[1] C.E.Perkins, *AdHoc Networking*, Addison-Wesley Publication, Singapore, 2001.

[2] E.M. Royer and C.K. Toh, "A *review of current routing protocols for ad-Hoc mobile wireless networks*," IEEE Personal Communications, vol. 6, no. 2, pp. 46-55, April 1999.

[3] C. E. Perkins and E. M. Royer, "*The adhoc on-demand distance vector protocol*," in Ad hoc Networking, C. E. Perkins, Ed. Addison-Wesley, 2000, pp. 173–219.

[4] I. Park and I. Pu, "*Energy efficient expanding ring search*," in Proc. IEEE AMS'07, Phuket, Thailand**,** Mar. 27-30, 2007, pp. 198-199.

[5] J. Hassan and S. Jha, "*Performance analysis of expanding ring search for multi-hop wireless networks*," in Proc. IEEE VTC2004-Fall., vol. 5, Los Angeles, CA, USA, Sept. 26-29, 2004, pp. 3615-3619.

[6] W. Heo and M. Oh, "*Performance of expanding ring search scheme in AODV routing algorithm*," in Proc. IEEE FGCN'08, vol.2, China, Dec. 13-15, 2008, pp. 128-132.

[7] Perkins, Charles E., and Elizabeth M. Royer. "*Ad-hoc on-demand distance vector routing*," In Mobile Computing Systems and Applications, 1999. Proceedings. WMCSA'99. Second IEEE Workshop on, pp. 90-100. IEEE, 1999

[8] H. Okada, and K. Mase, "*Performance analysis of wireless mesh networks with three sector antenna*," in Proc. ACM IWCMC '10, Caen, France, June 2010, pp.1232-1236

[9] X. Liu, H. Okada and K. Mase, "*Performance of wireless mesh networks with three sector antenna*," in Proc. IEEE MSN'08, Dec. 20-22, 2010, pp. 146-153.

[10] J. Janeček, "Application *of sector antennas in ad-hoc topologies*," in Proc. ACM IWCMC '09, Leipzig, Germany, June 21-24, 2009, pp. 207-211.

[11] Yang, Shuhui, and Jie Wu. "*Efficient broadcasting using network coding and directional antennas in MANETs*," Parallel and Distributed Systems, IEEE Transactions on 21, no. 2 (2010): 148-161

[12] Hu, Chunyu, Yifei Hong, and Jennifer Hou. "*On mitigating the broadcast storm problem with directional antennas*," In Communications, 2003. ICC'03. IEEE International Conference on, vol. 1, pp. 104-110. IEEE, 2003.

Vol.1 Issue.6, October 2013. Pgs: 42-47

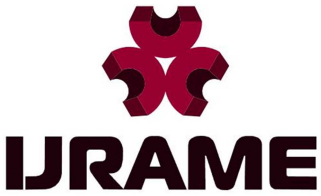

ISSN (ONLINE): 2321-3051
INTERNATIONAL JOURNAL OF RESEARCH IN AERONAUTICAL AND MECHANICAL ENGINEERING

Finite element analysis of deflection of rolls and its correction by providing camber on rolls

Vijay Gautam[1]
[1]Department of Mechanical Engg., Delhi Technological University, *vijay.dce@gmail.com*

Author Correspondence: Mech. Engg. Deptt.,DTU, Bawana Road, Delhi-110042, Telephone: 011-27871438, vijay.dce@gmail.com

Abstract

Rolling process is a key step in the production of flat steel products. Because of automation commonly implemented in flat product rolling mills, the products should meet the requirements of tight tolerances. one of the major defects observed in the rolling process is flatness and lack of attainment of the desired surface profile due to deflection of the rolls. The spatial shape and dimensions of the roll gap are influenced by the elastic deformation of all parts of the rolling stand equipment affected by the roll pressure. The current study aims to determine the variation of the deflection in rolls in a two high mill with varying percentage reduction of the sheet i.e, 20%, 25% and 30% on annealed and non-annealed IF steel sheet and analyzing possible solutions to reduce the elastic deflection of rolls with special emphasis on cambering and modelling of the same in Abaqus CAE.

***Keywords**:* cold rolling; recrystallization-temperature; elastic deflection; percentage reduction.

1. INTRODUCTION

Rolling is a metal forming process in which the metal ingot or sheet is pressed between two rotating rolls. Besides the compression by rolls, the friction between the work metal and surfaces of rolls also gives rise to compressive forces in the longitudinal and lateral directions. The demand for producing strips with narrow dimension tolerances is imposing a necessity to construct the stand with respective mill modulus and working rolls of optimum diameter (Janusz Po´spiech, 2005).

Yu Hai-Liang et al., 2007 presented an extensive situation review of deflection of rolls in a four high mill and analysed deflection of Sendzimir mill using 3D FEM under different rolling forces, strip widths and rolls assignments. Problem of deflection of rolls was treated by many authors and the literatures are relatively rich, both from theoretical and measuring point of view.

The problem on how to improve its shape and flatness, and the dimensional accuracy has always been of major interest to the steel manufacturers. Researchers have found solutions to these problems by introducing new types of mills, such as continuous variable crown (CVC) and pair cross (PC) mills equipped with roll shifting, roll crossing and work roll bending (B. Paolo et al. 1999, V. B. Ginzberg et al., 1997). A 3D Finite Element Method (FEM) has been used in the analysis of strip rolling by Kobayashi et al., 1989; Chenot et al. 1991 in the past. In his studies Z. Y. Jiang et al.,2003 showed that the specific force such as rolling force, intermediate force and the profile of the rolled strip for rolling is significantly

different with the traditional strip cold rolling process. When the entry thickness of strip increases, the edge contact force increases, the edge contact of work rolls becomes more significant, which has a significant effect on the intermediate force, and the shape of exit strip becomes poor. The flatness defects in rolling were studied and a numerical approach for prediction of defects were coined by S. Abdelkhalek et al., 2011.

2. Objective

This work is focused on the simplest rolling mill having two deforming rolls and the mill known as two-high mill. The rolls have to support the Roll Separating Force (R.S.F.), which has a shearing effect on the necks. Thus, the roll diameter should be large. However, since bigger rolls have greater R.S.F., the two-high is used in only cases of very narrow strip (for example, flattened wire) and a very light reduction (skinpass operation).

A two high mill with work roll diameter of 0.95m and 3.6m in length is selected to cold roll a strip of width 900mm with length of 0.5m and a thickness of 0.002m in a single pass. The dimensions of the roll shoulder are: Diameter 0.475m and length 0.2375m.

The percentage reductions taken to study the variation in the roll deflection are 20%, 25%, and 30%. The material chosen for the reduction by rolling is interstitial free (IF) steel which is widely used in automobile body panels and is deep drawable. The material received was in annealed and non-annealed condition to determine the effect of strain hardening on roll deflection.

The roller is made of D2 (Chromium Alloy) steel with Young's modulus 210GPa and 0.3 Poisson's ratio and the sheet is low carbon steel with Young's modulus of 202GPa and Poisson's ratio 0.3. The co-efficient of friction between the roll and sheet 0.147 to 0.176 and the roll rotating at a speed of 60 rpm were used in FEA simulations.

3. Methodology

The sheet samples of interstitial free steel were collected at entry and exit of the two high 4-stand rolling mills, rated 4000HP with soluble oil used as lubricant with a speed of 150m/min in the first stage reduction. Were tensile tested as per ASTM-E8M standard to characterize the tensile properties affecting the deflection of rolls in a two high mill. The sheet samples collected before and after a given reduction were tensile tested as per ASTM-E8M standard and mechanical properties are shown in table 1. The annealed tensile properties were used in FE-simulations to determine the roll deflection.

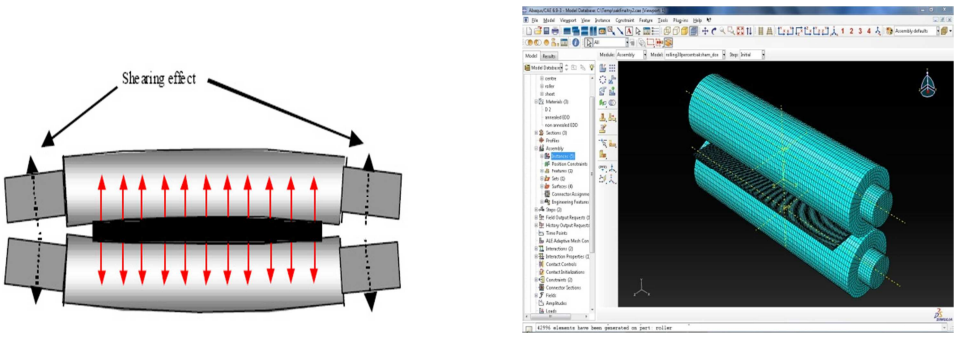

Figure 1: Figure shows two high mill with higher central deflection and as modelled in FEA

Table 1. *Showing Properties of IF steel for both Annealed and Non-Annealed after reduction*

IF-steel	0.2%-offset yield(MPa)	UTS (MPa)	Strain hardening exponent 'n'	Strength coefficient 'K'(MPa)	% Elongation
Annealed(CRCA)	123	205	0.33	428	51
Non -annealed (after deformation)	219	415	0.17	690	11

The following parameters are calculated prior to the rolling analysis:

- $\text{Tan } \alpha = \sqrt{((R*\Delta h)/(R-(\Delta h/2)))} \approx \sqrt{(\Delta h / R)}$ (1)
  Where, R = Radius of Roll and α = Angle of Bite, and Δh is Draft= $(h_i - h_o)$
- $L_p = \sqrt{(R * \Delta h)}$, (2)
  Where L_p = Projected Length
- $\mu \geq \text{Tan } \beta$ (3)
  μ = Friction Coefficient and β = varies from 0 to α

Table 2. *Various Rolling parameters used in simulations*

Percentage Reduction / Material	Angle of Bite (degrees)	Projected Length of Contact (m)	Minimum Value of μ for unaided entry
20% reduction	8.255	0.0689	0.145
25% reduction	9.214	0.077	0.162
30% reduction	10.076	0.0844	0.176

4. Results of 3D-fea model for cold rolling of a strip in a 2-high mill.

The numerical model developed in this study considers a percentage reduction of 20%, 25% and 30% on two types of material – annealed and non- annealed to establish the relationship between the camber of the sheet and the stress developed in the rolls. The subsequent pages of this chapter show the stress developed in the roll and the respective sheet profile.

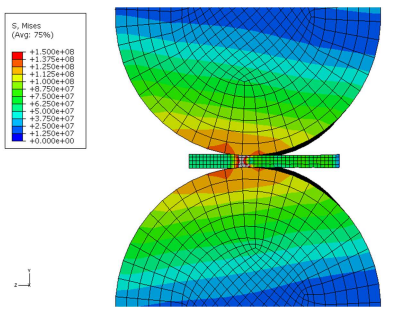

Fig. 2a: *Stress developed in the rolls.*

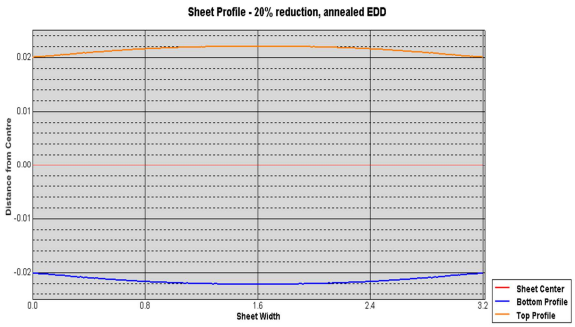

Fig. 2b: *Sheet surface profile during rolling*

Figure 2: *Stress analysis for 20% reduction of annealed IF-steel Sheet*

Vol.1 Issue.6,
October 2013.
Pgs: 42-47

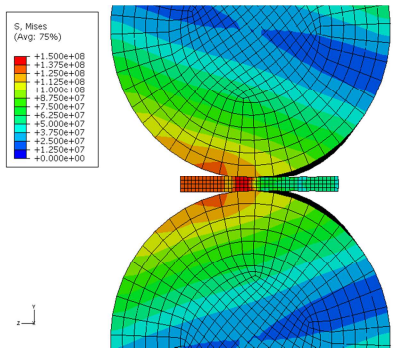

Fig. 3a: *Stress developed in rolls*

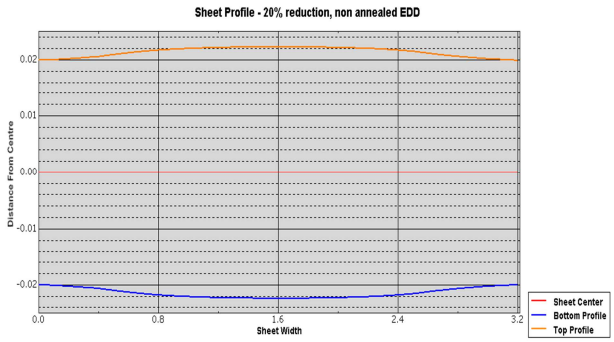

Fig. 3b: *Sheet surface profile during rolling*

Figure 3. *Stress analysis for 20% reduction with Non-Annealed IF-steel Sheet*

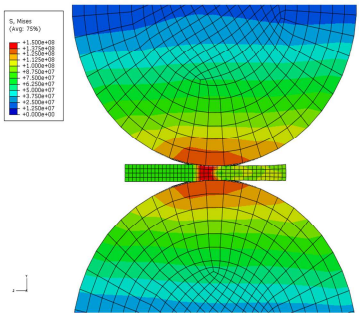

Fig. 4a: *Stress developed in the rolls*

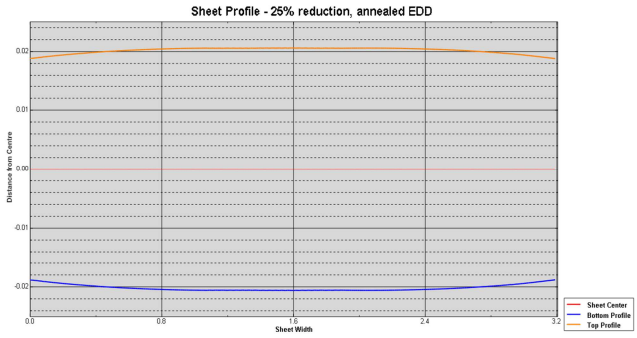

Fig.4b: *Sheet surface profile during rolling*

Figure 4. *Stress analysis for 25% reduction with annealed IF-steel Sheet*

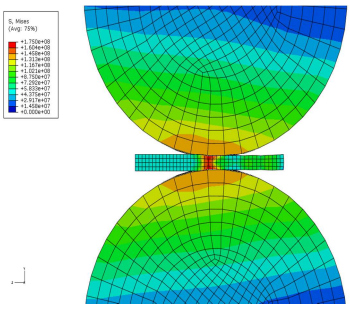

Fig. 5a : *Stress developed in the rolls*

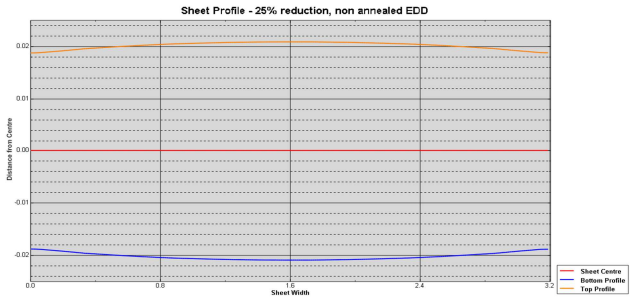

Fig.5b: *Sheet surface profile during rolling*

Figure 5. *Stress analysis for 25% reduction with non-annealed IF-steel Sheet*

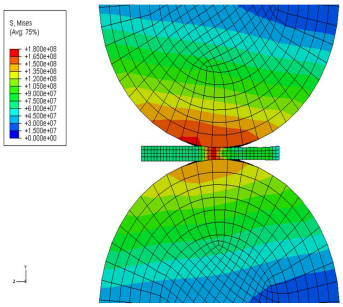

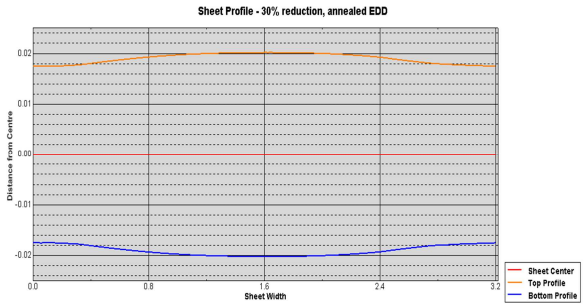

Fig. 6a: *Stress developed in the rolls*

Fig. 6b: *Sheet surface profile during rolling*

Figure 6. *Stress analysis for 30% reduction with annealed IF-steel Sheet*

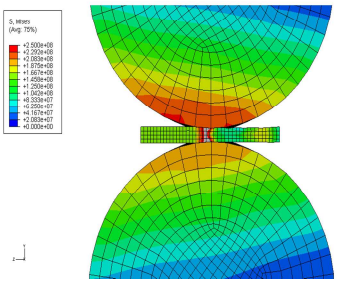

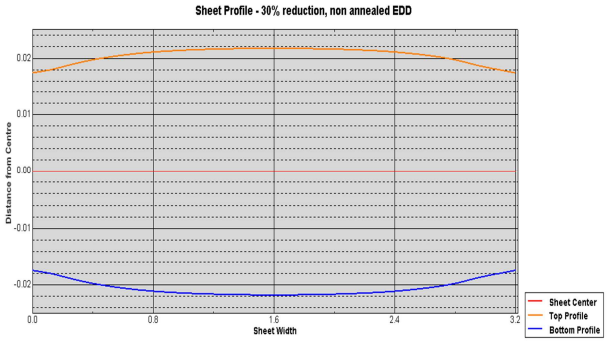

Fig. 7a: *Stress developed in the rolls*

Fig.7b: *Sheet surface profile during rolling*

Figure 7. ***S****tress analysis for 30% reduction with Non-Annealed IF-steel Sheet*

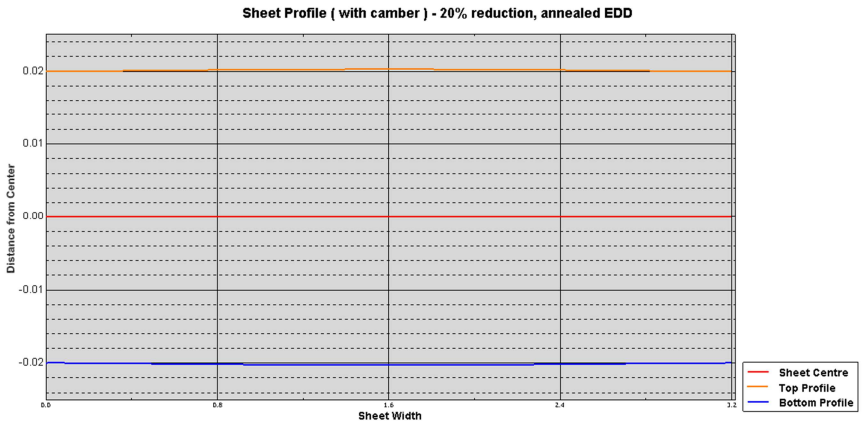

Figure 8. *Sheet surface profile after providing camber in rolls*

It is quite evident from the figure8, that when the camber was introduced in the diameter of rolls, the sheet cross sectional profile was straight and uniform with slight convexity at the middle of the sheet.

5. CONCLUSION

The roll deflection has been studied under the effect of roll separating force and its effect on the roll gap has been analysed using Abaqus CAE. The numerical model confers to the theoretical concepts of rolling and the results obtained are in agreement.

Further, the parametric study undertaken to reduce the roll deflection has been successful by employing camber in the rolls. Providing camber, it is found that the sheet profile improves, though complete removal of the convex deformation in sheet cross section is difficult.

The effect of annealing and strain hardening of the sample in rolling indicates that the strain hardening of the sheet produces higher stresses in the respective rolls than the stress developed when the annealed sheet is rolled necessitating the intermediate annealing.

6. References

ASTM standards E 8M-04, 2004, *Standard Test Methods for Tension Testing of Metallic Materials* [Metric].

B Paolo, B Roberto, R Massimo, 1999, New mill stand with flexible crown control for rolling ultra-thin hot strip, *Metall. Plant Technol. Int*., 22, (3), 7.

J L Chenot,P Montmitonnet, P Buessler, F Fau,1991, Finite element computation of spread in hot flat and shape rolling with a steady state approach. *Eng. Comput. (SwanseaWales)*, 8, (3), pp.245–255.

Janusz Po´spiech, 2005, Calculation method for deformations of stand and rolls to obtain products with small dimension of tolerances, *Journal of Materials Processing Technology*, 166, pp.417–422.

S Kobayashi, S I Oh, T Altan, 1989, Metal Forming and the Finite-Element Method, Oxford University Press, New York.

S Abdelkhalek, P Montmitonnet, N Legrand, P Buessler, 2011, Coupled approach for flatness prediction in cold rolling of thin strip, *International Journal of Mechanical Sciences*, 53, pp.661–675.

V B Ginzburg, M Azzam, 1997, Selection of optimum strip profile and flatness technology for rolling mills, *Iron Steel Eng.*, 74, (7), pp.30–38.

Yu Hai-liang, Liu Xiang-hua, Lee Gyoo Taek, 2007, Analysis of rolls deflection of Sendzimir mill by 3D FEM, *Trans. Nonferrous Met. Soc*., China, 17, pp.600-605.

Z Y Jiang, H T Zhu, A K Tieu, 2003, Effect of rolling parameters on cold rolling of thin strip during work roll edge contact, *Journal of Materials Processing Technology*, 140, pp.535–54.

A Brief Author Biography

***Vijay Gautam* –** is assistant professor in Mechanical Engineering Department in Delhi Technological University and teaches Plasticity and Metal Forming and Machine Design to M Tech and BTech(Mech Engg) students respectively. He has 14 years of teaching experience.

2013 5th International Conference on Computational Intelligence and Communication Networks

Object Recognition from color images by Fuzzy classification of Gabor Wavelet features

Seba Susan and Seema Chandna
Department of Information Technology,
Delhi Technological University

Abstract—**This paper introduces a novel object recognition approach based on the Gabor Wavelet representation of the binarized image that makes use of fuzzy logic for determining the 'soft' class label of the color test images with respect to the gray training templates. The fuzzy membership function used is a Generalized Gaussian function whose exponent value is determined empirically. The use of simple computations for assigning the class label to the query image makes the technique computationally effective. The experimental results on 494 color test images from ten object categories from the Caltech database show a high percentage of classification accuracy with only fifteen gray images from each category used for training. The efficiency of our method is established by comparing our results with that of different classifiers and also with Qiu's Content based Image retrieval (CBIR) system for color images.**

Keywords- Gabor Wavelet features, Object Recognition, Otsu Thresholding, Fuzzy memberships, Generalized Gaussian Function, Color to Gray classification

I. INTRODUCTION

Object detection and recognition has attracted significant attention over the past few years in the fields of computer vision, pattern recognition and image processing [1]. The researches in this field so far are the detection of objects from real-world images [2], objects from noisy images [3], objects from videos [4], objects moving in space [1] and also tracking multiple objects [5]. Various approaches like feature classification [2], combination of appearance, structural and shape features [5,18], viewpoint independent object detection algorithm [4], wavelet transform methods [3] were adopted for efficient object detection. In this paper we select the Gabor wavelet (GW) magnitude features [6-8] to identify the primary object/objects in a scene. The magnitude of Gabor Wavelet coefficients represents the local energy patterns associated with an object and are used to find objects having a similar local energy pattern. Gabor wavelets have been used in the past for object recognition, detection from infrared images [9], 3D object recognition [11], object tracking [10] and object detection using dynamic link architecture [12]. While object detection in [12] uses only Gabor magnitude, [11] uses Gabor magnitude, phase and frequency for detecting occluded objects. The detection of 3D objects is outside the purview of this paper and we use only the Gabor magnitude features for our experiments. To increase the performance of our system we use Otsu thresholding [13] prior to the filtering step for localizing the objects more efficiently since the shape or outline of the object is highly indicative [18] of its class. The combined advantages of Gabor Wavelet and Otsu thresholding has been explored in some works [6-8] though not related to object detection, where thresholding was performed at a later stage after filtering to reduce the redundancy in the wavelet-based representation. Recent works [16] stress on obtaining the semantically coherent interpretation of a scene for efficient object recognition in order to emulate the human visual system which perceives an object in an integrative manner [17]. We propose a new fuzzy classification scheme based on the feature representation of the binarized image displaying the outline of the object. The organization of this paper is as follows. Section II reviews the steps for the extraction of Gabor Wavelet features from an input color image. The proposed fuzzy classification scheme is outlined in Section III. Section IV presents the experimental results and the conclusions are given in Section V.

II. A REVIEW OF GABOR WAVELET FEATURES AND ITS EXTRACTION FROM AN IMAGE

An object is associated with certain inane characteristics such as shape, size and texture apart from the basic color information. It is also characterized by its ability to be distinct from its surroundings/background appearing as a blob of white in a black background in the simplest case. Our feature extraction stage consists of two main steps, the application of Otsu‘s thresholding for binarizing the image and applying the Gabor Wavelet filter bank to extract the magnitude response. The Gabor Wavelet filter bank is adept at representing high frequency structures within the binarized image. The Gabor Wavelet filter is defined as the product of a Gaussian kernel and a complex sinusoid which is then transformed with a Fourier transform to derive the time frequency analysis,

978-0-7695-5069-5/13 $26.00 © 2013 IEEE
DOI 10.1109/CICN.2013.69

$$k_v = \frac{k_{\max}}{f_v}\varphi_u = \frac{u\pi}{4}k_{\max} = \frac{\pi}{2} \quad (1)$$

Here $e^{-ik_{u,v}z}$ is a complex plane wave and $e^{-\frac{\sigma^2}{2}}$ is a term that compensates for the DC value which makes the kernel DC-free. The parameter z = (x,y) indicates a point which represents the horizontal and vertical coordinates of the image obtained after Otsu thresholding. The operator $\|.\|$ denotes the norm operator. Parameters u and ν define the angular orientation and the spatial frequency of the Gabor kernel where ν determines the scale of kernel. The standard deviation of Gaussian window is 2π.
The wave vector is given by,

$$k_{u,v} = k_v e^{i\varphi_u} \quad (2)$$

where $k_v = \frac{k_{\max}}{f_v}, \varphi_u = \frac{u\pi}{4}$

The maximum frequency $k_{\max} = \frac{\pi}{2}$ and the spatial factor f =√2 with ν ε {0,..,3} if four different scales are chosen. To detect objects having different colors but belonging to the same category due to resemblance in shape and texture, we train the classifiers with gray-level images only. The test images are however color images and Gabor Wavelet features are extracted separately for each color dimension R,G,B in the same manner. The feature extraction steps for our experiment are summarized below:

Step 1: Create a Gabor Wavelet filter bank by setting the parameters for Gabor wavelets as follows:
Gabor kernel size= 24x24, four orientations= 0, π/4, π/2, 3π/4 and four scales= 0,1,2,3.

Step 2: The Gabor kernel is composed of real and imaginary parts for the four orientations and four scales

Step 3: **N**ormalize the size of the color image to a fixed size of 40×40 and repeat following steps 4 to 6 for each of the R,G,B channels (testing images) or to the gray image (training images).

Step 4: Use Otsu's thresholding method to binarize the 2-D image data.

Step 5: Convolve the binarized image with real and imaginary part of filter kernel (obtained in step 2), done separately.

Step 6: Calculate the 40x40 Gabor Wavelet magnitude response from the Real and Imaginary responses of the filter for each of the four orientations and for each of the four scales to generate overall 4×4×40×40=25600 filter coefficients concatenated into 1D.

Step 7: Repeat the above steps 1-6 for all the images in the database. So a feature vector of size 25600×3 for each test image and 25600x1 for each training image is obtained.

III. PROPOSED FUZZY CLASSIFIER FOR OBJECT RECOGNITION IN COLOR DOMAIN

In the proposed fuzzy classification procedure, a fuzzy membership function is computed for each query color image with respect to each gray image in the training database. In this case the query image (color image) and each of the training images (in gray) are represented by Gabor Wavelet magnitude feature vectors of length 25600 per dimension as explained in Section II. Retaining the color information of the test images is useful when the gray level representation of the training image finds more resemblance to (any) one of the R,G,B color representations of the test image rather than to its gray level counterpart. The technique makes our system independent of the actual color of the object and just detects if the shape and pattern identifying the object is present strongly in any of the three color domains. The strength of the resemblance is measured with the help of fuzzy membership functions. The choice for the fuzzy membership function for our experiments is the popularly used Gaussian function which is a non-linear, monotonically decreasing function whose mean and standard deviation parameters can be used to adapt the function to a largely varying dataset. The flexibility of the Gaussian curve can be further enhanced by using a variable degree exponent instead of the quadratic exponent of the exponential in which case the function is called a Generalized Gaussian Function (GGF). Consider test sample **x** represented by the 25600x3 color feature vector. The fuzzy membership function of test vector **x** of dimension 25600x3 to a training feature vector **u** of dimension 25600x1 is given by the Generalized Gaussian function (GGF) as shown below,

$$\mu_{ij} = e^{-a(x_{ij}-u_i)^b}, \text{ for j=1,2,3} \quad (3)$$

The parameters a and b of the GGF function in (3) are determined empirically for the best performance from a batch of training samples. In (3) x_{ij} denotes the i_{th} feature of the j_{th} color channel for the test image and u_i denotes the i_{th} feature for the gray training image respectively, where i varies from 1 to 25600 and j varies from 1 to 3 as explained in the preceding sections. Averaging the memberships for the 25600 features of a single color channel j gives the mean membership of the test sample $\mathbf{x_j}$ to the training sample **u** for the particular color dimension j as shown below.

$$\mu_j = \frac{\sum_{i=1}^{25600}\mu_{ij}}{25600}, \text{ for j=1,2,3} \quad (4)$$

The maximum membership value among the three color channels is the membership of the test sample **x** to training sample **u**.

$$\mu_u = \max_j \{\mu_j\} \quad (5)$$

The (maximum) membership computed in (5) measures the maximum strength of resemblance possible between the gray level training vector **u** and the R,G,B color domains of the test vector **x**. The above procedure is repeated for all training vectors **u**, and the maximum membership of **x** to a particular **u** decides its class as that of the same class as **u**.

$$Class(\mathbf{x}) = Class(\arg\max_{\forall u}(\mu_u)) \quad (6)$$

The color to gray fuzzy classification procedure detailed above is performed for all test samples **x** and the classification accuracy is computed based on the number of test samples correctly classified.

IV. EXPERIMENTAL RESULTS AND DISCUSSION

The experimental work is performed on ten categories of the Caltech dataset [14] popularly used for object recognition experiments. The ten categories of objects selected for our work are namely, *Butterfly, Ketch, Garfield, Gramophone, Electric Guitar, Hedgehog, Mandolin, Menorah, Panda,* and *Pyramid* with the size of images being 300x 200 pixels. Fifteen images from each class are converted to gray and used for training and the rest of the color images are used for testing the proposed classifier, creating overall a training database of 150 images and a testing database of 494 images. The MALAB 7.4 software was used for implementation on a Intel 2.10 GHz processor. Initially a set of supervised experiments are conducted on 100 samples of the training dataset (split as 50 samples for training and 50 samples for testing) to determine the optimal value of the exponent b in (3) for best classification results as b‘s value is varied from 1.2 to 2.0, a‘s value in (3) being fixed at 1. The training samples classification results compiled in Table 1 (coarse results from 1.2 to 2.0) and Table 2 (fine tuned results from 1.6 to 1.8) show that the best classification results are obtained for an exponent value of 1.66 and this is the value used for testing our fuzzy classifier for the 494 test samples. The classification results shown in Table 3 show a high classification accuracy of 74.1% for the fuzzy classification method inspite of having rigorous training of only fifteen images per category and it outperforms the distance based Nearest Neighbor classifier for both color only and gray only images (56.9% and 57.9% respectively). The average execution speed is also one of the lowest as seen from Table 3 (approximately six seconds) facilitating real time execution at high accuracy. We also compare our results with other popular classifiers such as MLP Neural Networks (with 100 hidden neurons), Naïve Bayesian classifier and SVM classifier (linear kernel) for the same set of gray level training images and the results (60.9%, 45% and 46.4% respectively) indicate the supremacy of our classification method. The primary advantage of our method over these classifiers is that the gray prototype can be used for identifying the object in the color domain regardless of the actual color combinations in the scene. We also compare our results with Qiu’s well known CBIR technique for color images based on chromatic and achromatic patterns which gives a low performance of 38.1%. Some specific test examples are shown in Fig. 1 for both the best and worst cases for our method and these indicate that binarizing of the image prior to Gabor Wavelet feature extraction plays a significant role in extracting the silhouette and shape of the object which helps in accurate classification.

V. CONCLUSION

A new fuzzy classification of Gabor Wavelet features is proposed for object recognition from color images given a set of gray-level training images. The advantage of the proposed scheme is that it couples high accuracy with real-time execution as proved by the experimental results. The proposed image retrieval obtained in real-time with an execution time of six seconds for each query image with a high accuracy of 74.1% on an extensive dataset. A comparison with other classifiers and retrieval approaches highlights our method‘s supremacy. Otsu‘s Threshold is used for binarizing the image prior to feature extraction and the Generalized Gaussian Function (GGF) is used for computing the fuzzy memberships in all our experiments. Empirical results on a subset of training images indicate that an exponent of 1.66 is most apt for the GGF function.

REFERENCES

[1] Roach, J. W.; Aggarwal, J. K., “Computer Tracking of Objects Moving in Space”, *IEEE Transactions on Pattern Analysis and Machine Intelligence,* Volume: PAMI-1 , Issue: 2, Year: 1979 , Page(s): 127 – 135.

[2] F. Dornaika, F. Chakik; "Efficient Object Detection and Matching Using Feature Classification "; IEEE Conference Pattern Recognition (ICPR), 2010 20th International Conference; page(s): 3073 - 3076; 2010.

[3] R.N. Strickland, He Il Hahn; "Wavelet transform methods for object detection and recovery"; *IEEE Transactions Image Processing*,; volume: 6; issue: 5; page(s): 724 - 735; 1997.

[4] Ping-Han Lee, Yen-Liang Lin, Shen-Chi Chen, Chia-Hsiang Wu, Cheng-Chih Tsai, Yi-Ping Hung; "Viewpoint-Independent Object Detection Based on Two-Dimensional Contours and Three-Dimensional Sizes*"; IEEE Transactions Intelligent Transportation Systems*,; volume: 12; issue: 4; page(s): 1599 - 1608; 2011.

[5] Li He, Hui Wang, Hong Zhang; "Object detection by parts using appearance, structural and shape features"; *IEEE Conference Mechatronics and Automation(ICMA), 2011*; page(s): 489 - 494 ; 2011.

[6] R.M. Rangayyan, R.J. Ferrar, J.E.L. Desautels, A.F. Frere, “Directional Analysis of Images with Gabor Wavelets”, *IEEE Computer Graphics and Image Processing, Proceedings XIII Brazilian Symposium* ,Page(s): 170 - 177 , 2000.

[7] Zhongliang Fu, Chunya Tong, Huang Yan, Zhou Fan, “Parallel Gabor Wavelet Transform for Edge Detection”, *IEEE International Conference Internet Technology and Applications*, , *Page(s):* 1 – 3, 2010.

[8] Z. Yavuz, C. Kose; "Comparing 2D matched filter response and Gabor filter methods for vessel segmentation in retinal images"; *Electrical, Electronics and Computer Engineering (ELECO), IEEE 2010 Conference*; page(s): 648 - 652; 2010.

[9] R. Neil Braithwaite and Bir Bhanu,“Hierarchical Gabor Filters for Object Detection in Infrared Images*”, IEEE conf*, 1994.

[10] Like Zhang, Dong Qin,“The Object Tracking Study Based on the

Gabor Wavelet Character", *IEEE International Conference on Mechatronics and Automation, 2006*.

[11] Xing Wu and Bir Bhanu, Fellow, IEEE, "Gabor Wavelet Representation for 3-D Object Recognition", *IEEE Transactions On Image Processing*, Vol. 6, No. 1, January 1997.

[12] M. Lades, J. C. Vorbruggen, J. Buhmann, J. Lange, C. Von der Malsburg, R. P. Wurtz, and W. Konen, "Distortion invariant object recognition in the Dynamic Link Architecture," *IEEE Transactions on Computers,* vol. 42, pp. 300-311, 1993.

[13] N.Otsu, A threshold selection method from gray level histograms, *IEEE SMC-9*, page 62-66, Jan 1979

[14] R. Fergus and P. Perona, "Caltech Object Category datasets", *http://www.vision.caltech.edu/Image_Datasets/ altech101/Caltech101.html, 2003.*

[15] G Qiu, "Indexing chromatic and achromatic patterns for content-based colour image retrieval", *Pattern Recognition*, vol. 35, pp. 1675 – 1686, August, 2002.

[16] Choi, Myung Jin, Antonio Torralba, and Alan S. Willsky. "A tree-based context model for object recognition." *Pattern Analysis and Machine Intelligence, IEEE Transactions on* 34.2 (2012): 240-252.

[17] Pennick, Mark R., and Rajesh K. Kana. "Specialization and integration of brain responses to object recognition and location detection." *Brain and behavior* 2.1 (2012): 6-14.

[18] Marszałek, Marcin, and Cordelia Schmid. "Accurate object recognition with shape masks." *International journal of computer vision* 97.2 (2012): 191-209.

TABLE 1: Determining the exponent b of GGF function : Coarse testing 1.2 to 2.0

Object Classes	b parameter value (taken with interval 0.1)								
	1.2	**1.3**	**1.4**	**1.5**	**1.6**	**1.7**	**1.8**	**1.9**	**2.0**
1	0	0	1	4	5	5	5	5	5
2	0	0	0	1	5	5	4	4	4
3	0	0	2	4	5	5	4	4	3
4	0	0	0	2	5	4	4	3	3
5	0	0	0	0	2	3	3	3	3
6	0	0	0	3	5	5	5	5	5
7	0	0	0	2	4	5	5	5	5
8	5	5	5	4	4	3	3	3	3
9	0	0	5	5	4	3	1	1	1
10	0	0	0	3	3	4	4	4	4
Total Correctly Classified Images (out of 50)	**5**	**5**	**14**	**28**	**42**	**42**	**38**	**37**	**36**

TABLE 2: Determining the exponent b of GGF function : Fine testing from 1.61 to 1.79

Object Classes	b parameter value (taken with interval 0.01)																		
	1.61	**1.62**	**1.63**	**1.64**	**1.65**	**1.66**	**1.67**	**1.68**	**1.69**	**1.70**	**1.71**	**1.72**	**1.73**	**1.74**	**1.75**	**1.76**	**1.77**	**1.78**	**1.79**
1	5	5	5	5	5	5	5	5	5	5	5	5	5	5	5	5	5	5	5
2	5	5	5	5	5	5	5	5	5	5	5	5	5	5	5	5	5	5	4
3	5	5	5	5	5	5	5	5	5	5	5	5	5	4	4	4	4	4	4
4	4	4	4	4	4	4	4	4	4	4	4	4	4	4	4	4	4	4	4
5	2	2	3	3	4	4	3	3	3	3	3	3	3	3	3	3	3	3	3
6	5	5	5	5	5	5	5	5	5	5	5	5	5	5	5	5	5	5	5
7	4	4	4	4	4	5	5	5	5	5	5	5	5	5	5	5	5	5	5
8	4	4	3	3	3	3	3	3	3	3	3	3	3	3	3	3	3	3	3
9	4	4	4	4	4	4	3	3	3	3	3	3	3	2	2	2	2	2	2
10	3	3	4	4	4	4	4	4	4	4	4	4	4	4	4	4	4	4	4
Total Correctly Classified	**41**	**41**	**42**	**42**	**43**	**44**	**42**	**42**	**42**	**42**	**42**	**42**	**42**	**40**	**40**	**40**	**40**	**40**	**39**

TABLE 3: Classification accuracies (in %) of various methods for the 494 test images

OBJECT CLASS	Test Images per class	A2	A4	A5	A6	A7	A10	A11
1. Butterfly	76	36.8	60.5	59.2	38.2	31.6	55.3	**75**
2. Garfield	19	42.1	31.6	47.4	26.3	26.3	42.1	**63.2**
3. Gramophone	36	16.7	33.3	36.1	19.4	33.3	38.9	**63.9**
4. Electric Guitar	60	23.3	46.7	55.0	33.3	38.3	51.7	**71.7**
5. Hedgehog	39	**66.7**	59.0	48.7	56.4	64.1	56.4	61.5
6. Ketch	99	56.6	75.8	66.7	59.6	51.5	71.7	**82.8**
7. Mandolin	28	17.9	75.0	64.3	60.7	46.4	50	**78.6**
8. Menorah	72	34.7	66.7	72.2	59.7	48.6	55.6	**73.6**
9. Panda	23	17.4	47.8	17.4	30.4	43.5	26.1	52.2
10. Pyramid	42	38.1	73.8	64.3	47.6	57.1	78.6	**90.5**
Average (%age)		38.1	60.9	57.9	46.4	45.0	56.9	74.1
Time per sample (in seconds)		28.73	77.59	0.75	6.19	4.37	0.09	6.54

A2 is Qui's CBIR technique [15] (Color training and Color test images)
A4 is MLP Neural Network Classifier for Gabor Wavelet features (Gray training and Gray test images)
A5 is Nearest Neighbor Classifier for Gabor Wavelet features (Gray training and Gray test images)
A6 is SVM Classifier for Gabor Wavelet features (Gray training and Gray test images)
A7 is Naive Bayesian Linear Classifier for Gabor Wavelet features (Gray training and Gray test images)
A10 is Nearest Neighbor Classifier for Gabor Wavelet features (Color training and Color test images)
A11 is **Proposed Fuzzy Classifier** for Gabor Wavelet features (Gray training and Color test images)

(i) (ii)

Fig.1 Some test examples from the Hedgehog, Ketch and Panda Categories (i) Some easily classified images (a) Original image (b) binarized image (shown for R,G,B) (ii) Some wrongly classified images by the proposed method (a) Original image (b) binarized image (shown for R,G,B) (c) Categories to which (a) got wrongly classified